

AD-A037 248

SCIENCE APPLICATIONS INC ANN ARBOR MICH
THERMAL IMAGING SYSTEMS' RELATIVE PERFORMANCE: 3-5 MICROMETERS --ETC(U)

F/G 17/5

JAN 77 T W TUE

DAEA18-73-A-0127

UNCLASSIFIED

SAI-76-005-AA

AFAL-TR-76-217

NL

1 OF 2
AD
A037248



ADA037248

AFAL-TR-76-217

12



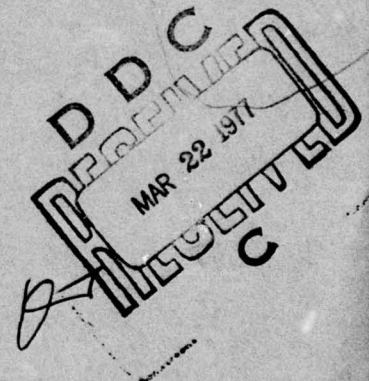
THERMAL IMAGING SYSTEMS' RELATIVE PERFORMANCE: 3-5 μm vs 8-12 μm

*SCIENCE APPLICATIONS, INC.
15 RESEARCH DRIVE
ANN ARBOR, MICHIGAN 48103*

JANUARY 1977

TECHNICAL REPORT AFAL-TR-76-217

FINAL REPORT FOR PERIOD 30 MARCH 1976 to 30 JUNE 1976



Approved for public release; distribution unlimited

AIR FORCE AVIONICS LABORATORY
AIR FORCE WRIGHT AERONAUTICAL LABORATORIES
AIR FORCE SYSTEMS COMMAND
WRIGHT-PATTERSON AIR FORCE BASE, OHIO 45433

NOTICE

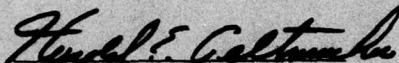
When Government drawings, specifications, or other data are used for any purpose other than in connection with a definitely related Government procurement operation, the United States Government thereby incurs no responsibility nor any obligation whatsoever; and the fact that the government may have formulated, furnished, or in any way supplied the said drawings, specifications, or other data, is not to be regarded by implication or otherwise as in any manner licensing the holder or any other person or corporation, or conveying any rights or permission to manufacture, use, or sell any patented invention that may in any way be related thereto.

This report has been reviewed by the Information Office (OI) and is releasable to the National Technical Information Service (NTIS). At NTIS, it will be available to the general public, including foreign nations.

This technical report has been reviewed and is approved for publication.


JAMES J. STEWART
Project Engineer

FOR THE COMMANDER


HAROLD E. GELTMACHER, ACTG CHIEF
Electro-Optics & Reconnaissance Branch
Reconnaissance and Weapon Delivery Division

Copies of this report should not be returned unless return is required by security considerations, contractual obligations, or notice on a specific document.

Unclassified

SECURITY CLASSIFICATION OF THIS PAGE (When Data Entered)

REPORT DOCUMENTATION PAGE		READ INSTRUCTIONS BEFORE COMPLETING FORM
1. REPORT NUMBER AFAL-TR-76-217	2. GOVT ACCESSION NO.	3. RECIPIENT'S CATALOG NUMBER
4. TITLE (and Subtitle) THERMAL IMAGING SYSTEMS' RELATIVE PERFORMANCE: 3-5 Micrometers vs 8-12 Micrometers	5. TYPE OF REPORT & PERIOD COVERED Final Report 30 March to 30 June 1976	
7. AUTHOR(s) Thomas W. Tuer	14. PERFORMING ORG. REPORT NUMBER SAI-76-005-AA	15. CONTRACT OR GRANT NUMBER(s) DAEA18-73-A-0127 Order No. 0009
9. PERFORMING ORGANIZATION NAME AND ADDRESS Science Applications, Inc. 15 Research Drive Ann Arbor, MI 48103	10. PROGRAM ELEMENT, PROJECT, TASK AREA & WORK UNIT NUMBERS 2004-05-25	
11. CONTROLLING OFFICE NAME AND ADDRESS	12. REPORT DATE January 1977	
	13. NUMBER OF PAGES 107	
14. MONITORING AGENCY NAME & ADDRESS (if different from Controlling Office) Air Force Avionics Laboratory AFAL/DOP Wright-Patterson AFB, OH 45433	15. SECURITY CLASS. (of this report) Unclassified	
16. DISTRIBUTION STATEMENT (of this Report) Approved for public release; distribution unlimited.		
17. DISTRIBUTION STATEMENT (of the abstract entered in Block 20, if different from Report)		
18. SUPPLEMENTARY NOTES		
19. KEY WORDS (Continue on reverse side if necessary and identify by block number) Thermal Imaging FLIR Atmospheric Transmission Atmospheric Path Radiance		
20. ABSTRACT (Continue on reverse side if necessary and identify by block number) The performance of a thermal imaging system operating in the 3-5 μm window relative to a system operating in the 8-12 μm window is calculated parametrically. Airborne systems operating against typical ground targets are evaluated using Barhydt's system performance model with sophisticated models for atmospheric transmission (Lowtran III) and path radiances, and for target and terrain radiances. Present results are found to be in general agreement with previous analyses, considering the differences in conditions assumed.		

DD FORM 1 JAN 73 1473 EDITION OF 1 NOV 65 IS OBSOLETE

Unclassified

SECURITY CLASSIFICATION OF THIS PAGE (When Data Entered)

68

blank
ii

PREFACE

This work was undertaken to review and update previous evaluations of thermal imaging systems' performance in the two main infrared atmospheric windows: 3-5 μm and 8-12 μm . Many of the previous evaluations were based on outdated or erroneous models, especially those for atmospheric transmission. The present analysis employed the latest available models, and addressed the Air Force scenarios of viewing tactical ground target from airborne systems.

ACCESSIO. for	
NTIS	White Section <input checked="" type="checkbox"/>
DIC	Both Section <input type="checkbox"/>
UNANNOUNCED	<input type="checkbox"/>
JUSTIFICATION	
BY	
DISTRIBUTION/AVAILABILITY CODES	
Dist.	Avail. or for SPECIAL
A	

b.1 gmK

TABLE OF CONTENTS

SECTION	PAGE
I. Summary	1
II. Introduction	3
III. Literature Survey	6
IV. Theoretical Development	11
1. Performance Model	11
2. Atmospheric Transmission	13
3. Background Radiance	45
4. Target Signatures	60
V. Calculated Relative Performances	64
VI. Conclusions and Recommendations	81
Appendix A: Availability of Intermediate Results	83
Appendix B: Calculational Procedure	86
Appendix C: Relative Performance at Zero Range	88
References	90

LIST OF FIGURES

FIGURE	PAGE
1. Comparison of Lowtran and Hitran Calculated Atmospheric Spectral Transmission Including Nitrogen Continuum, Mid-latitude Summer Sea Level Model, 1 km Range	15
2. Comparison of Lowtran and Hitran Calculated Atmospheric Spectral Transmission Including Nitrogen Continuum, Mid-latitude Summer Sea Level Model, 10 km Range	16
3. Comparison of Lowtran and Hitran Calculated Atmospheric Spectral Transmission Including Nitrogen Continuum, Mid-latitude Summer Sea Level Model, 20 km Range	17
4. Comparison of Lowtran and Hitran Calculated Atmospheric Spectral Transmission Including Nitrogen Continuum, Mid-latitude Summer Sea Level Model, 40 km Range	18
5. Comparison of Lowtran and Hitran Calculated Average Transmission as a Function of Range for Two Spectral Regions, Including Nitrogen Continuum, Midlatitude Summer Sea Level Model	19
6. Lowtran Nitrogen Continuum Transmission Model; 5 km Range, Midlatitude Summer Atmospheric Model at Sea Level	20
7. Comparison of Various 8-12 μ m Water Continuum Models	23
8. Comparison of Aerosol Size Distributions	25
9. Comparison of Aerosol Extinction Models in 4 μ m Region	27
10. Comparison of Aerosol Extinction Measurements in 4 μ m Region	28
11. Comparison of Aerosol Extinction Measurements and Models in 10 μ m Region	29
12. Lowtran III Calculated Aerosol Spectral Transmission for Two Visibilities in the Long Wavelength and Short Wavelength Infrared (LWIR & SWIR) Atmospheric Windows	31
13. Calculated SWIR Spectral Atmospheric Transmission as a Function of Range; Midlatitude Winter Model Atmosphere, 8.5 km Visibility, 0.75 km Altitude	32

LIST OF FIGURES (CONTINUED)

FIGURE	PAGE
14. Calculated LWIR Spectral Atmospheric Transmission as a Function of Range; Midlatitude Winter, 8.5 km Visibility, 0.75 km Altitude	33
15. Calculated SWIR Spectral Atmospheric Transmission as a Function of Range; Midlatitude Summer Model Atmosphere, 8.5 km Visibility, 0.75 km Altitude	34
16. Calculated LWIR Spectral Atmospheric Transmission as a Function of Range; Midlatitude Summer, 8.5 km Visibility, 0.75 km Altitude	35
17. Calculated SWIR Spectral Atmospheric Transmission as a Function of Range; Tropical Model Atmosphere, 8.5 km Visibility, 0.75 km Altitude	36
18. Calculated LWIR Spectral Atmospheric Transmission as a Function of Range; Tropical Model Atmosphere, 8.5 km Visibility, 0.75 km Altitude	37
19. Calculated SWIR Spectral Atmospheric Transmission for Various Atmospheric Models; 8.5 km Visibility, 0.75 km Altitude, 5 km Range	39
20. Calculated LWIR Spectral Atmospheric Transmission for Various Atmospheric Models; 8.5 km Visibility, 0.75 km Altitude, 5 km Range	40
21. Calculated SWIR Spectral Atmospheric Transmission for Various Water Continuum Models; Tropical Model Atmosphere, 8.5 km Visibility, 0.75 km Altitude, 5 km Range	41
22. Calculated LWIR Spectral Atmospheric Transmission for Various Water Continuum Models; Tropical Model Atmosphere, 8.5 km Visibility, 0.75 km Altitude, 5 km Range	42
23. Calculated SWIR Spectral Atmospheric Transmission as a Function of Visibility; Midlatitude Summer Model Atmosphere, 5 km Range, 0.75 km Altitude	43
24. Calculated LWIR Spectral Atmospheric Transmission as a Function of Visibility; Midlatitude Summer Model Atmosphere, 5 km Range, 0.75 km Altitude	44

LIST OF FIGURES (CONTINUED)

FIGURE	PAGE
25. Measured Spectral Radiant Intensity of Typical Terrain.	46
Backgrounds by Smith and Blay	
26. Measured Spectral Terrain Radiance by Smith and Blay.	48
27. Comparison of Calculated and Measured Spectral Terrain.	50
Radiance	
28. Calculated SWIR Spectral Atmospheric Path Radiance	52
as a Function of Range; Midlatitude Winter Model At- mosphere, 8.5 km Visibility, 0.75 km Altitude	
29. Calculated LWIR Spectral Atmospheric Path Radiance	53
as a Function of Range; Midlatitude Winter Model At- mosphere, 8.5 km Visibility, 0.75 km Altitude	
30. Calculated SWIR Spectral Atmospheric Path Radiance	54
as a Function of Range; Midlatitude Summer Model At- mosphere, 8.5 km Visibility, 0.75 km Altitude	
31. Calculated LWIR Spectral Atmospheric Path Radiance	55
as a Function of Range; Midlatitude Summer Model At- mosphere, 8.5 km Visibility, 0.75 km Altitude	
32. Calculated SWIR Spectral Atmospheric Path Radiance	56
as a Function of Range; Tropical Model Atmosphere, 8.5 km Visibility, 0.75 km Altitude	
33. Calculated LWIR Spectral Atmospheric Path Radiance	57
as a Function of Range; Tropical Model Atmosphere, 8.5 km Visibility, 0.75 km Altitude	
34. Calculated Spectral Atmospheric Path Radiance as a	58
Function of Visibility; Midlatitude Summer Model At- mosphere, 5 km Range, 0.75 km Altitude	
35. Calculated Spectral Atmospheric Path Radiance as a	59
Function of Visibility; Midlatitude Summer Model At- mosphere, 5 km Range, 0.75 km Altitude	
36. Target Spectral Radiation Function (phot/sec/sr/ μ m/K)	62
for Tank at Various Aspects Based on Measurements by Moulton	

LIST OF FIGURES (CONTINUED)

FIGURE	PAGE
37. Calculated Target Spectral Radiation Function (phot/sec/sr/ μ m/K) for Various Target Temperatures	63
38. Calculated Performance of a 3.4-4.8 μ m FLIR Relative to an 8.1-12.2 μ m FLIR as a Function of Atmospheric and Aerosol Models; 0.75 km Altitude, Nominal Target and Terrain	65
39. Calculated Performance of a 3.4-4.8 μ m FLIR Relative to an 8.1-12.2 μ m FLIR for Various Water Continuum Model Combinations; Tropical Atmosphere, Other Conditions Nominal	68
40. Calculated Performance of a 3.4-4.8 μ m FLIR Relative to an 8.1-12.2 μ m FLIR as a Function of Platform Altitude, 8.5 km Visibility, Nominal Target and Terrain	69
41. Calculated Performance of a 3.4-4.8 μ m FLIR Relative to an 8.1 - 12.2 μ m FLIR as a Function of the Target Mid- latitude Summer, 0.75 km Altitude, 8.5 km Visibility	70
42. Calculated Performance of a 3.4-4.8 μ m FLIR Relative to an 8.1-12.2 μ m FLIR as a Function of the Terrain; Mid- latitude Summer, 0.75 km Altitude, 8.5 km Visibility, Nominal Target	72
43. Calculated Performance of a 3.4-4.8 μ m FLIR Relative to an 8.1 - 12.2 μ m FLIR for Various Performance Model Treatments of the Background	73
44. Calculated Performance of a 3.4-4.8 μ m FLIR Relative to Several Long Wavelength FLIRs; Midlatitude Summer At- mosphere, 8.5 km Visibility, 0.75 km Altitude, Nominal Target and Terrain	75
45. Calculated Performance of Several Short Wavelength FLIRS Relative to an 8.1-12.2 μ m FLIR; Midlatitude Summer At- mosphere, 8.5 km Visibility, 0.75 km Altitude, Nominal Tartet and Terrain	76
46. Comparison of Calculated Relative Performance with those of Mundie, Barhydt and Schnitzler	77
47. Comparison of Calculated Relative Performance with that of Milton	80

LIST OF TABLES

TABLE	PAGE
1. Range of Study Parameters	4
2. Relative Performance from Barhydt [19]; 3.4-4.8 vs 8.1-12.2 μm Systems	9
3. Measured Effective Temperatures and Projected Areas of Operating Tank [61]	61
A1. Calculated Atmospheric Spectral Transmission and Path Radiance Cases	83
A2. Calculated Terrain and Target Radiance Cases	84

LIST OF SYMBOLS

SYMBOL	DEFINITION	EQUATION
A_p	projected area	4-16
\bar{B}	signal from background	3-2
C	contrast	3-2
C_I, C_M	contrast for uniform and variegated backgrounds	3-3
C_1, C_2	Planck's constants	4-14
C_v	absorption coefficient	4-6
c	speed of light	3-5
$c_{s,f}$	self and foreign broadened coefficients for continuum absorption	4-7
D	aperture diameter	4-4
D'	detectability	3-2
h	Planck's constants	3-5
J	radiant intensity	3-1
K	factor for photovoltaic detector	3-5
k	absorption coefficient	4-7
L	radiance	3-1
$N(r)$	aerosol size distribution function	4-9
\bar{n}	aerosol complex index of refraction	4-9
P	performance	4-5
p	partial pressure	4-7
Q_{ext}	aerosol extinction efficiency	4-9
R	range	3-1
$R_{\Delta T}$	radiation function, Barhydt's model	3-5
$R'_{\Delta T}$	radiation function with system parameters	3-6
r	aerosol radius	4-9
\bar{S}	signal with target	3-2
T	temperature	3-4
T_o	parameter describing the temperature effect on C_S	4-8

LIST OF SYMBOLS (CONTINUED)

SYMBOL	DEFINITION	EQUATION
w	absorber amount	4-6
w_w	water vapor content	4-7
Z	function of wavelength and temperature	4-15
$z(\alpha)$	function of angular width in Schnitzler's model	3-4
α	target angular width	3-4
ΔT_{in}	noise required-input temperature difference	3-4
ϵ	emittance	4-12
η_d	normalized detector size parameters	3-6
η_q	detector quantum efficiency	3-6
λ	wavelength	3-5
ρ	angular resolution	4-4
τ	transmission	3-5
ω	solid angle	3-1

SUBSCRIPTS

a	atmosphere	3-5
BB	blackbody	4-12
b	background	3-4
eff	effective	4-13
ext	extinction	4-9
f	filter	3-5
f	foreign gas	4-7
g	terrain	4-10
LWIR	long wavelength infrared	4-4
m	measured	4-11
max	maximum	
min	minimum	

LIST OF SYMBOLS (CONTINUED)

SUBSCRIPTS (CONTINUED)

SYMBOL	DEFINITION	EQUATION
p	path	4-10
SWIR	short wavelength infrared	4-4
t	target	3-5
w	water	4-7
ξ	relative detector performance	4-4
o	zero range	C-1

SUPERSCRIPTS

*	quantum units (e. g. , photons/sec rather than watts)	4-2
-	averages	3-2

SECTION I

SUMMARY

A review of previous analyses for the relative performance of short and long wavelength thermal imaging systems (i. e. , nominal 3-5 versus 8-12 μm), indicates some serious shortcomings in the ancillary models employed. All analyses consider horizontal sea level atmospheric paths, neglect or approximate path radiance, and assume only blackbody functions for target and terrain radiances. The present study treats atmospheric slant paths from various aircraft altitudes and ranges with the latest Lowtran transmission model (Lowtran III), and a sophisticated path radiance model developed by Anding (Radst), for various seasonal, latitudinal, and aerosol models. Actual radiance measurements of typical targets and terrains are employed, in addition to theoretically predicted radiances for various target and terrain temperatures.

The results of this parametric analysis indicate that for the nominal target considered here (i. e. , tank, rear aspect), the short wavelength system is superior to the long wavelength system at all ranges for the Tropical and Midlatitude Summer models at most of the typical operating conditions. This superiority increases with range, until at twenty kilometers, there is about an order of magnitude difference between the performance of the two systems for Summer conditions, and about two orders of magnitude for Tropical conditions. It is recognized that these results are in apparent conflict with previous analyses. However, comparisons with these analyses do indicate general agreement, when differences in assumed conditions are accounted for. For Winter conditions, the performance of the two systems is comparable within typically 30% for ranges from zero to twenty kilometers; the short wavelength system

is slightly better at shorter ranges and slightly worse at longer ranges. For cooler targets (or at other aspects), the performance of the short wavelength systems becomes inferior to the long wavelength systems at short ranges for the Summer and Tropical conditions, and at all ranges for the Winter condition.

Aerosols are predicted to have little effect on relative performance, but this is thought to be an erroneous result due to a simplification in the Lowtran model. The relative performance of the short wavelength system improves with increasing target temperature, decreasing altitude, and decreasing terrain temperature, although the latter effect is not particularly significant. No large advantages are evident for other spectral bandpasses within these two window regions, at ranges less than twenty kilometers. Comparisons with other analyses of this type show general agreement, considering the differences in conditions assumed. In order to evaluate the present results in a laboratory environment, an infrared transmissometer and peripheral equipment was delivered in August 1976, for use in the AFAL Tower Facility as a calibration tool.

SECTION II

INTRODUCTION

Thermal imaging systems (sometimes referred to as FLIRs, Forward Looking Infrared) have proven their value for a variety of Air Force missions. Most of these systems operate in the 8 to 12 μm atmospheric window, since early design studies indicated this window provided superior performance over the 3-5 μm window for most operating conditions. More recent analyses indicated that short wavelength systems may be superior to long wavelength systems, for long, humid slant paths. There are also some operational considerations which may favor the short wavelength system (e. g. , better window thermal properties, better resolution, etc.). It was therefore decided to conduct this study to determine, in a parametric fashion, the situations where each system is preferred. Another reason for a new analysis is that many of the previous studies were based on unsophisticated or outdated models.

The scope of the present study is limited to an aircraft based system, viewing a typical ground target at ranges less than twenty kilometers from altitudes between one-half and one kilometer. The latest Lowtran transmission model (i. e. , Lowtran III) was to be used to consider various atmospheric models. The range of parameters employed in this study is outlined in Table 1. In general, the analysis concentrated on using updated atmospheric, target and background models, while using an existing sensor performance model. It should be emphasized that this study is limited to analyzing the performance of a short wavelength infrared (i. e. , SWIR, defined here nominally as 3.4 - 4.8 μm) thermal imaging system relative to a long wavelength infrared (i. e. , LWIR, defined here nominally as 8.1 - 12.2 μm) system. Whether either system will operate adequately for the conditions considered here is not within the scope of this study.

Table 1.
Range of Study Parameters

<u>Platform</u>	
Altitude	0.5, 0.75*, 1.0 km
Range	0 - 20 km
<u>Sensor</u>	
Spectral Regions ¹	3.4 - 4.8 and 8.1 - 12.2 μ m
<u>Atmospheres</u>	
Lowtran III Models	Midlatitude Winter and Summer*, and Tropical
Aerosol Model	5, 8.5*, 23 km Visibility
Continuum	Burch 4 μ m Water Continuum ²
<u>Target (Typical Tank)</u>	
Aspect	Front, Side, Rear*
Temperature	Measured and 250, 275, 325, 350 K
<u>Background</u>	
Terrain Radiance	Day and Night* Measured and 250, 270, 290, 310 K
Path Radiance	Same Conditions as "Atmospheres," Above
* Denotes nominal condition which were generally employed when the other parameters were varied.	
¹ Other narrower bands within these nominal bands were also investigated.	
² Other continua at 4 and 10 μ m were also investigated.	

The organization of this report is as follows. Major conclusions and recommendations are summarized in Section I. The purpose and scope of the study, and the organization of the report are given in the present section (i. e., Section II). Section III surveys some of the more important existing literature in this field. The theoretical development and main characteristics of the various models employed in the present analysis (i. e., the sensor model, the atmospheric transmission and

radiance models, and the target and terrain radiance models) are given in Section IV. Calculated relative performance results, for thermal imaging systems operating in the short and long wavelength atmospheric windows, are presented in Section V. Finally, Section VI indicates the main conclusions of the analysis, and makes recommendations for future investigations in this field. Ancillary information is also presented in three appendices (Appendix A, B and C).

SECTION III LITERATURE SURVEY

Biberman considered the problem of detecting a target against uniform and cluttered backgrounds [1]. He proposed the following criteria:

$$\begin{aligned} J/R^2 &\geq \omega L && \text{uniform background} \\ J/R^2 &\geq 2\omega L_{\max} && \text{cluttered background} \end{aligned} \tag{3-1}$$

where J is the target radiant intensity, R is the range, ω is the field of view, and L is the background radiance. For the cluttered case, the criterion is necessary but perhaps not sufficient, and the maximum value to background radiance in the field of view must be used. This discussion did not consider such parameters as optical gain, cell noise, cell sensitivity or system noise, and did not give any quantitative results.

Mundie considered the relative merits of detectors which utilize the 3-5 and 8-13 μm atmospheric windows [2]. He suggested the following performance criteria:

$$\begin{aligned} \text{Signal-to-Noise Ratio:} & \quad \frac{\bar{S}_{\min} - \bar{B}_{\min}}{L} \\ \text{Clutter-to-Noise Ratio:} & \quad \frac{\bar{B}_{\max} - \bar{B}_{\min}}{L} \\ \text{Contrast:} & \quad C \equiv \frac{\bar{S}_{\min} - \bar{B}_{\max}}{\bar{B}_{\max} - \bar{B}_{\min}} \\ \text{Detectability:} & \quad D' \equiv \frac{\bar{S}_{\min} - \bar{B}_{\max}}{N} \end{aligned} \tag{3-2}$$

where \bar{B}_{\min} and \bar{B}_{\max} are the averages of the detector output signals generated by viewing members of the hottest and coolest background

families, respectively; and \bar{S}_{\min} and \bar{S}_{\max} are the signals when a small target is in the field of view against the respective background families. Using these expressions, Mundie evaluated the relative performance of short-to-long wavelength FLIRs assuming blackbody radiances for the targets and backgrounds, and a "temperate" atmospheric transmission model. The transmission was representative of 50 atm · cm of CO_2 and 2 pr · cm of H_2O , based on measurements by Yates and Taylor [3], and Wyatt, et. al. [4, 5]. He concluded that the performance of the short wavelength scanner was inferior to the long wavelength scanner by factors of 2.5 and 8.4 at ranges of zero and 1.6 km, respectively. The calculated performance of the two systems is equivalent at target temperatures of 440 and 530 K, at ranges of zero and 1.6 km, respectively.

Rosell, Sendall, et. al., considered the image contrast and modulation contrast for uniform and variegated backgrounds, respectively [6-14]:

$$C_I \equiv \frac{L_{\max} - L_{\min}}{L_{\max}} \quad \text{uniform background} \quad (3-3)$$

$$C_M \equiv \frac{L_{\max} - L_{\min}}{L_{\max} + L_{\min}} \quad \text{variegated background}$$

where L is the radiance of the target or background. They developed complex expressions for system performance in uniform and cluttered backgrounds considering such parameters as finite apertures of the sensors and other elements of the system (i. e., modulation transfer functions), the image size and shape, the integration time of the eye, picture aspect ratio, etc. However, they apparently did not carry out calculations on relative performance of various systems.

Schnitzler considered composite FLIR-visual systems' performance in detecting targets of various sizes [15, 16]. He developed expressions for the "noise required-input temperature difference" ΔT_{in} to express the performance of thermal imaging systems for spot detection. Using values of the various psychophysical and system parameters based on test data, the following expressions resulted:

$$\begin{aligned}\Delta T_{in} &= 7.19 \times 10^{-4} \left[L_b / \left(\frac{dL_b}{dT} \right) \right] z(\alpha) & 8.13 - 12.2 \mu m \\ \Delta T_{in} &= 6.83 \times 10^{-3} \left[L_b / \left(\frac{dL_b}{dT} \right) \right] z(\alpha) & 3.33 - 4.17 \mu m\end{aligned}\quad (3-4)$$

where L_b is the background radiance and z is a function of the angular width of the target, α .

Using Lowtran II with the standard Tropical atmospheric model at 5 and 23 km visibility [17], ΔT_{in} was evaluated as a function of both α and range. According to these calculations, the long and short wavelength FLIR systems give equivalent performances between about 3.5 and 3.9 km for both visibilities and all target sizes; the short wavelength system is superior at larger ranges.

Barhydt, et. al., developed a "radiation function" to compare long and short wavelength thermal imaging infrared sensors [18, 19]:

$$R_{\Delta T} = \frac{1}{2\sqrt{2hc}} \frac{\int_0^\infty \tau_f(\lambda) \tau_a(\lambda) \left(\frac{\partial^2 J_t}{\partial T \partial \lambda} \right) \lambda d\lambda}{\left[\int_0^\infty \tau_f(\lambda) \frac{\partial L_b^*}{\partial \lambda} d\lambda \right]^{1/2}} \quad (3-5)$$

where τ_f and τ_a are the transmissions of the filter and the atmosphere, respectively, J_t is the radiant intensity of the target, and L_b^* is the radiance of the background in quantum units (e. g., photons/sec/sr/m²).

Other spectral dependent parameters are also considered to evaluate the relative performance:

$$R'_{\Delta T} = K\eta_d\sqrt{\eta_q} R_{\Delta T}$$

where K is unity for a photoconductive detector and $\sqrt{2}$ for a photovoltaic detector, η_q is the detector quantum efficiency, and η_d is the detector size parameter. Four measurements of atmospheric transmission by Yates and Taylor [3], at different ranges and humidities, were employed to evaluate this function; 300 K blackbodies were assumed for the target (J_t) and the background (L_b^*). For two different system aperture-resolution combinations, the performance of the short wavelength system was calculated to be 1.7 to 2.7 times better than the long wavelength system at a range of 18.7 km and a relative humidity of 82% (see Table 2). At the other three range-humidity combinations, the short wavelength system was calculated to be inferior to long wavelength system.

Table 2.
Relative Performance from Barhydt [19];
3.4-4.8 vs 8.1-12.2 μm Systems

Range (km)	Relative Humidity (%)	Aperture- Resolution (in-mrad)	Relative Performance
5.5	51	1.25	0.30
5.5	73	1.25	0.33
16.3	53	1.25	0.37
16.3	82	1.25	1.74
5.5	51	0.8	0.46
5.5	73	0.8	0.51
16.3	53	0.8	0.57
16.3	82	0.8	2.74

Milton, et. al. [20], used the performance model of Barhydt [18] in a similar analysis, except they used the Lowtran II atmospheric transmission model [17] to evaluate τ_a , instead of using the measurements of Yates and Taylor. Calculations were presented as a function of range, for three visibilities (i. e., aerosol models) and four humidities. At a humidity of 18 gm/m^3 (near the Tropical model Schnitzler used), the long and short wavelength systems were predicted to give equivalent performances at ranges from about 5 to 7 km.

Moser [21] referred to a mathematical model of airborne FLIR operational performance, but did not describe it. He did reference several reports [22-24], but due to time limitations of the current contract, these reports were not reviewed. Shumaker and Keller [25] presented a model of FLIR performance, but did not show any comparisons.

In summary, the four authors who presented relative performance were Mundie, Schnitzler, Barhydt and Milton (their results are compared to the present results in Section V). All used simple blackbody radiances for the target and background. For atmospheric transmission values, Mundie and Barhydt used measurements by Yates and Taylor, while Schnitzler and Milton employed the Lowtran II code. All authors considered only horizontal sea-level paths, and apparently neglected the path radiance contribution to background noise (see Section IV, #3).

SECTION IV THEORETICAL DEVELOPMENT

In this section formulations are given for various equations and procedures used in the calculation of the relative performance of thermal imaging systems. Section IV, #1 gives the development of the performance model, Section IV, #2 discusses the atmospheric transmission considerations, Section IV, #3 considers background radiance, and Section IV, #4 presents target signature calculations.

1. Performance Model

A model developed by Barhydt [18] was used in this study to evaluate the relative performance of thermal imaging systems:

$$R_{\Delta T} = \frac{1}{2\sqrt{2hc}} \frac{\int_0^{\infty} \tau_f(\lambda) \tau_a(\lambda) \frac{\partial^2 J_t}{\partial T \partial \lambda} \lambda d\lambda}{\left[\int_0^{\infty} \tau_f(\lambda) \frac{\partial L_b^*}{\partial \lambda} d\lambda \right]^{1/2}} \quad (4-1)$$

For relative performance, only spectrally varying factors are important, so the constant in front of the equation can be neglected. The filter function (τ_f) is assumed to be perfect, i. e., unity inside the spectral band and zero outside. The λ in the numerator is simply to correct for not using quantum units in the numerator for J . If photons are used here (i. e., J_t^*), as in the numerator, λ can be removed. Thus we have:

$$R_{\Delta T} \propto \frac{\int_{\Delta\lambda} \tau_a(\lambda) \frac{\partial^2 J_t^*}{\partial T \partial \lambda} d\lambda}{\left[\int_{\Delta\lambda} \frac{\partial L_b^*}{\partial \lambda} d\lambda \right]^{1/2}} \quad (4-2)$$

Three other spectrally dependent terms from the full signal-to-noise expression must also be considered:

$$R'_{\Delta T} = K\eta_d\sqrt{\eta_q} R_{\Delta T} \quad (4-3)$$

where K is unity for photoconductive detectors, but equal to $\sqrt{2}$ for photovoltaic detectors; η_q is the detector quantum efficiency; and η_d is the normalized detector size parameter. Barhydt [19] recommends values of 0.5 for η_q for detectors in both spectral regions* (e. g., indium antimonide in the 3-5 μm region, and mercury-doped germanium in the 8-12 μm region). To compensate for the inherently lower value of MTF in the 8-14 μm region (due to the increase in optical diffraction, smaller detectors can be employed. To obtain the same MTF, η_d for long wavelength systems is reduced from unity in the short wavelengths to between 0.5 and 0.8 (for aperture diameter - nominal angular resolution products: $D\rho = 0.8 - 1.25$ in-mrad, respectively [18]). Thus, the short to long wavelength ratio of these three parameters (i. e., the relative detector performance, ξ) varies between:

$$\xi \equiv \frac{(K\eta_d\sqrt{\eta_q})_{\text{SWIR}}}{(K\eta_d\sqrt{\eta_q})_{\text{LWIR}}} = 1.77 - 2.83 \quad (4-4)$$

In the present study, the larger value (i. e., 2.83 corresponding to more advanced systems) was used. ** Finally, the relative performance is expressed as:

$$P = \xi \frac{(R_{\Delta T})_{\text{SWIR}}}{(R_{\Delta T})_{\text{LWIR}}} \quad (4-5)$$

* In his original paper [18], Barhydt suggested $\eta_q = 0.25$ for mercury-doped germanium detectors.

** It should be noted that neither Mundie [2] or Milton [20] included this factor.

2. Atmospheric Transmission

Previous studies of this nature (see Section III) have used either measurements by Yates and Taylor [3] or the Lowtran II code [17] for evaluating the spectral atmospheric transmission. Although measurements (such as those of Yates and Taylor) are probably more realistic than calculations, they are limited in the range of conditions which can be considered. Lowtran is a one parameter band model for calculating atmospheric transmission for arbitrary slant paths based on techniques suggested by Altshuler [26]. It also considers aerosol extinction (i. e. , scattering and absorption), and certain continuum molecular absorption.

a. Molecular Line Absorption

The Lowtran II model, used in some previous studies of this type, has been superceded by Lowtran III which updates some of the band model parameters [27]. Lowtran considers the uniformly mixed atmospheric gases: CO_2 , N_2O , CH_4 , CO , N_2 and O_2 ; as well as non-uniform water vapor and ozone. Its main assumption is that the average transmittance over a twenty wavenumber spectral interval can be represented by a single parameter of the form:

$$\bar{\tau} = f(C_\nu w) \quad (4-6)$$

where C_ν is the wavelength dependent absorption coefficient and w is the equivalent absorber amount. Lowtran is most inaccurate in the window regions between strong bands (i. e. , the weak line approximation region). A warning is given [27]: "The one-dimensional prediction scheme presented... is not accurate for such conditions...". These of course are just the regions of most interest in the present study.

A sample line-by-line calculation (i. e. , Hitran) using the AFCRL line parameter compilation [28], was performed for comparison with the Lowtran III results. Because of the expense of such line-by-line calculations, only two narrow regions in the short wavelength window (i. e. , 3.4 - 4.1 and 4.55 - 4.8 μm) were considered. To be consistent with the Lowtran results, the infinite resolution line-by-line results were degraded to 20 wavenumber resolution (using a square filter function). Figures 1-4 compare the spectral transmission calculated by the two techniques for the Midlatitude Summer, sea level condition at several ranges. It is immediately apparent that although the results were presumably degraded to the same resolution, the line-by-line calculations show much more spectral detail than those of Lowtran. Note also that the degree of agreement at various wavelengths is different at different ranges (some improving and some becoming worse with range). This is characteristic of a single parameter band model, and can be improved using a two-parameter model.

A comparison of the transmission integrated over the spectral band is shown in Figure 5 as a function for range. It is seen that for the 3.4 - 4.1 μm spectral region, Lowtran gives low transmission relative to the line-by-line calculations at short ranges, and high transmission at longer ranges. The maximum error for this band for ranges less than 40 km is about $\pm 6\%$. For the other bandpass (i. e. , 4.55 - 4.8 μm), the error is about the same at short ranges, but increases with range beyond about 20 km. At 40 km range, the Lowtran results are almost a factor of two below the line-by-line results. Water continuum and aerosol extinction are not included in these results (nitrogen continuum is, since it cannot easily be suppressed from the Lowtran results). However since these components (i. e. , water continuum and aerosol extinction) are slowly varying

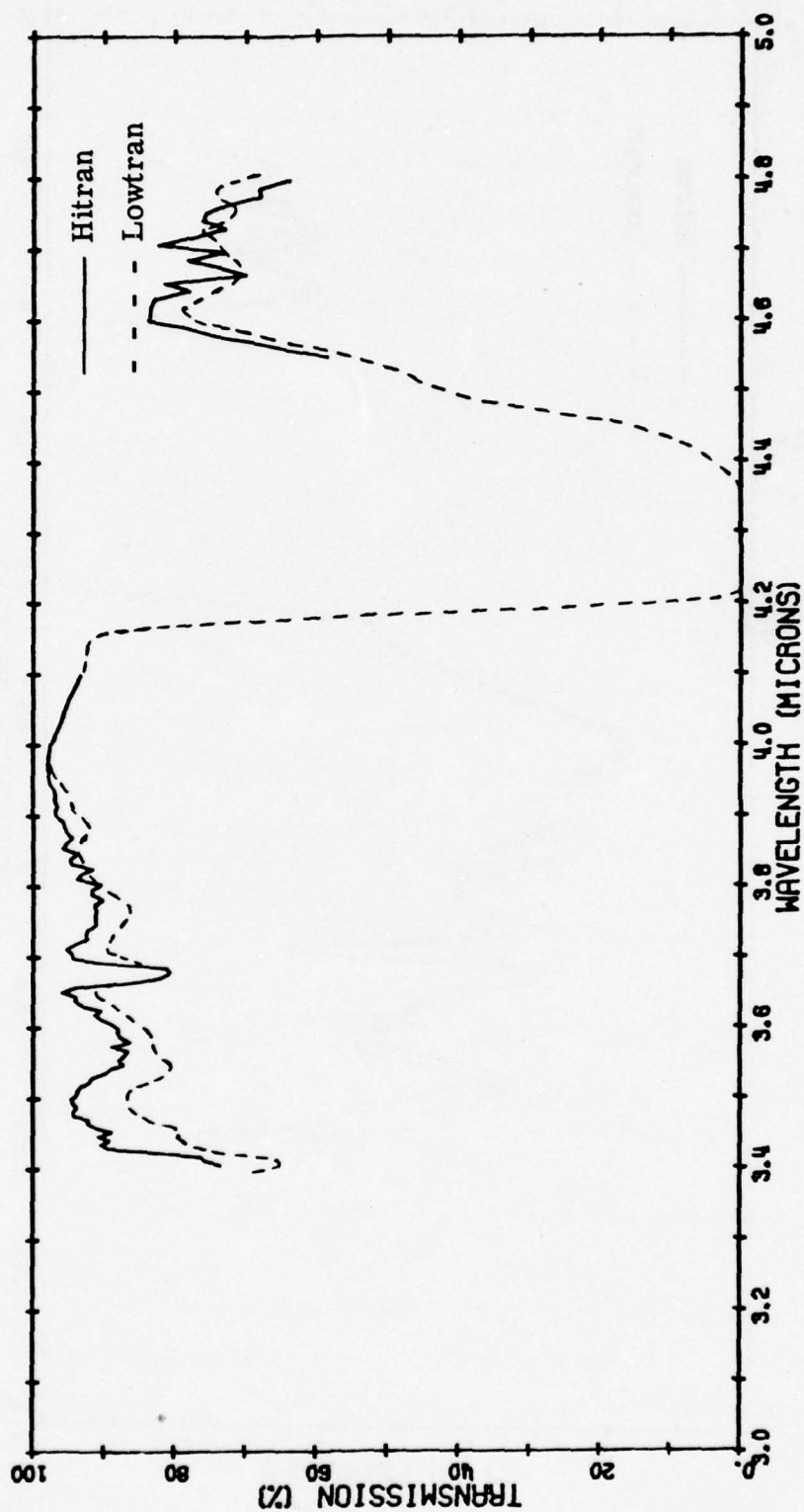


Figure 1. Comparison of Lowtran and Hitran Calculated Atmospheric Spectral Transmission Including Nitrogen Continuum, Midlatitude Summer Sea Level Model, 1 km Range

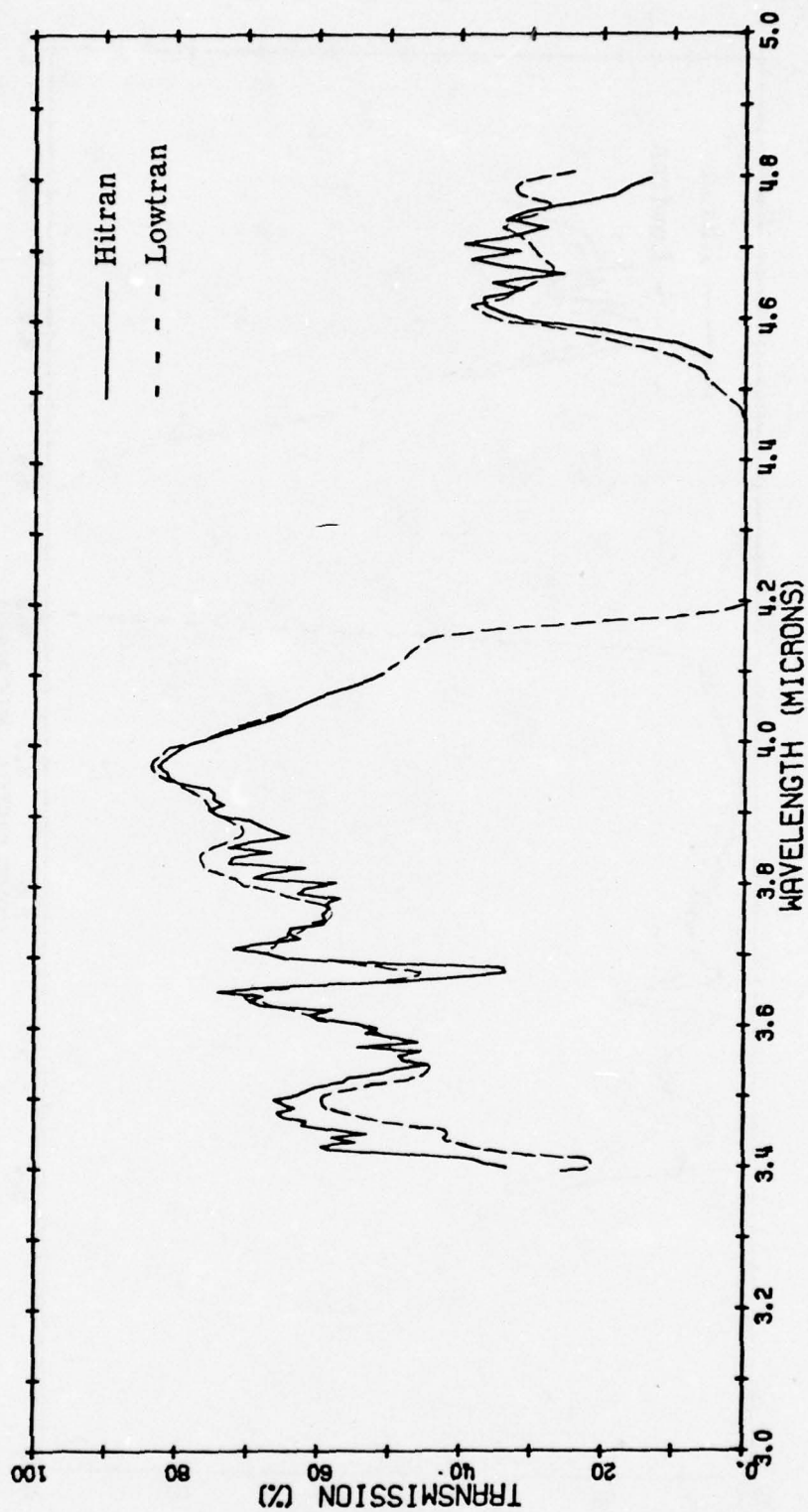


Figure 2. Comparison of Lowtran and Hitran Calculated Atmospheric Spectral Transmission Including Nitrogen Continuum, Midlatitude Summer Sea Level Model, 10 km Range

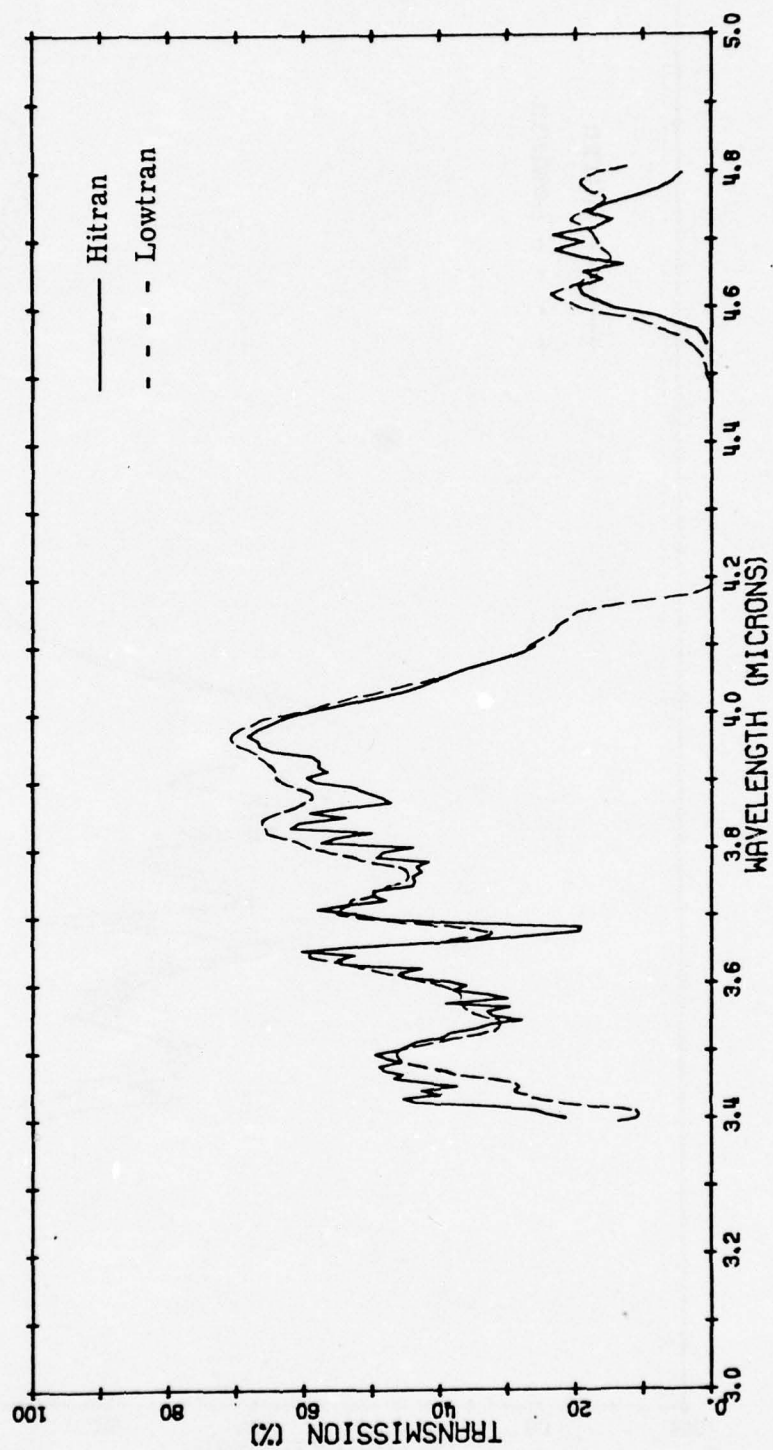


Figure 3. Comparison of Lowtran and Hitran Calculated Atmospheric Spectral Transmission Including Nitrogen Continuum, Midlatitude Summer Sea Level Model, 20 km Range

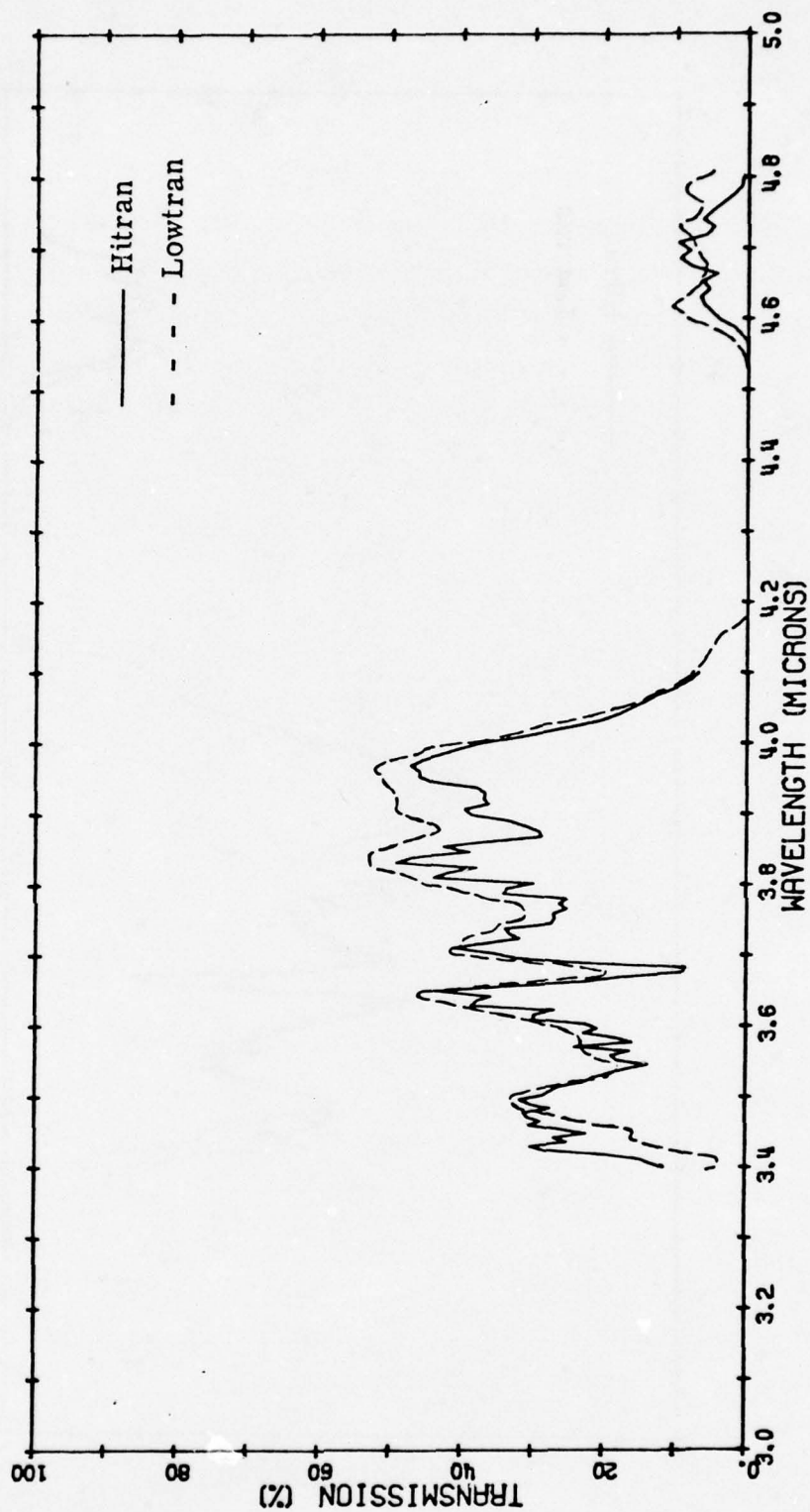


Figure 4. Comparison of Lowtran and Hitran Calculated Atmospheric Spectral Transmission Including Nitrogen Continuum, Midlatitude Summer Sea Level Model, 40 km Range

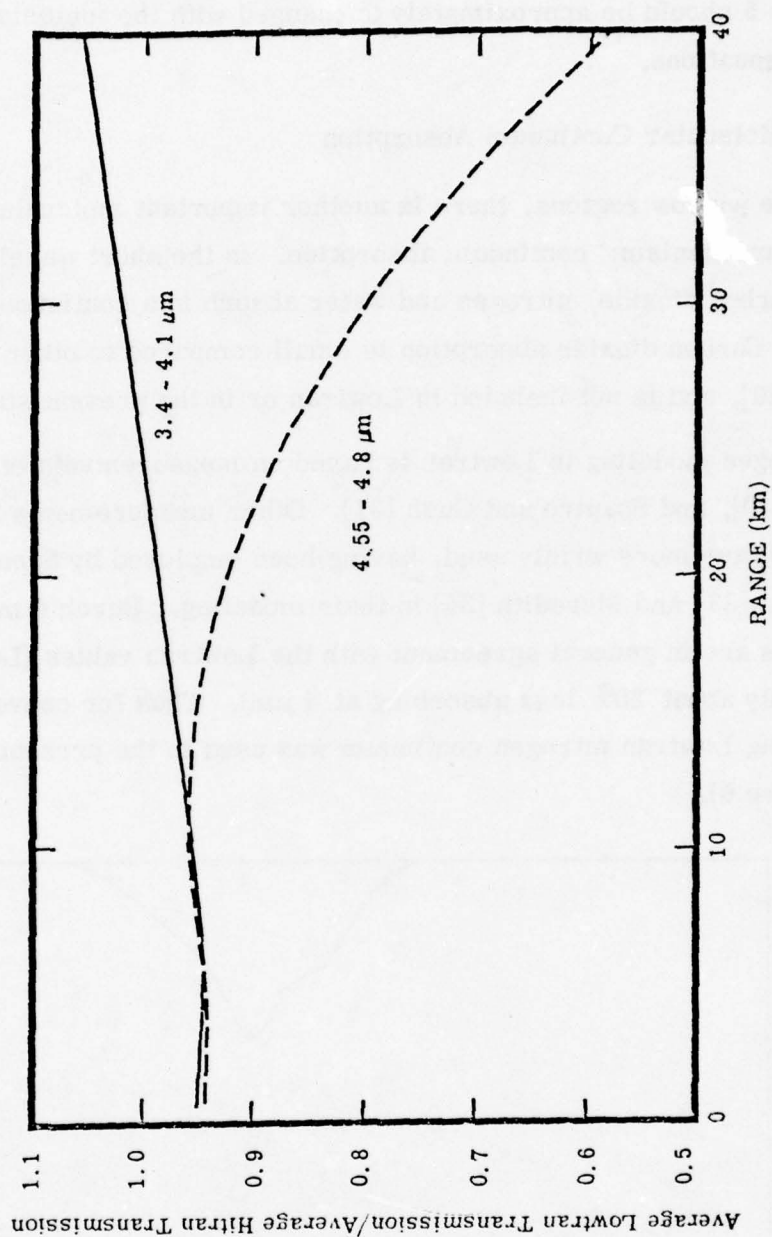


Figure 5. Comparison of Lowtran and Hitran Calculated Average Transmission as a Function of Range for Two Spectral Regions, Including Nitrogen Continuum; Midlatitude Summer Sea Level Model

functions of wavelengths (see Sections IV, 1b and IV, 1c), they are, to a good approximation, multiplicative factors. Thus, the ratio shown in Figure 5 should be approximately unchanged with the inclusion of those attenuations.

b. Molecular Continuum Absorption

In the window regions, there is another important molecular absorption mechanism: continuum absorption. In the short wavelength region carbon dioxide, nitrogen and water absorb in a continuous fashion. Carbon dioxide absorption is small compared to other mechanisms [29], and is not included in Lowtran or in the present study.

Nitrogen modeling in Lowtran is based on measurements of Reddy and Cho [30], and Shapiro and Gush [31]. Other measurements by Burch [29] are more widely used, having been employed by Spencer [32], Long [33] and Meredith [34] in their modeling. Burch's measurements are in general agreement with the Lowtran values (Lowtran is only about 20% less absorbing at $4\text{ }\mu\text{m}$). Thus for convenience, the existing Lowtran nitrogen continuum was used in the present study (see Figure 6).

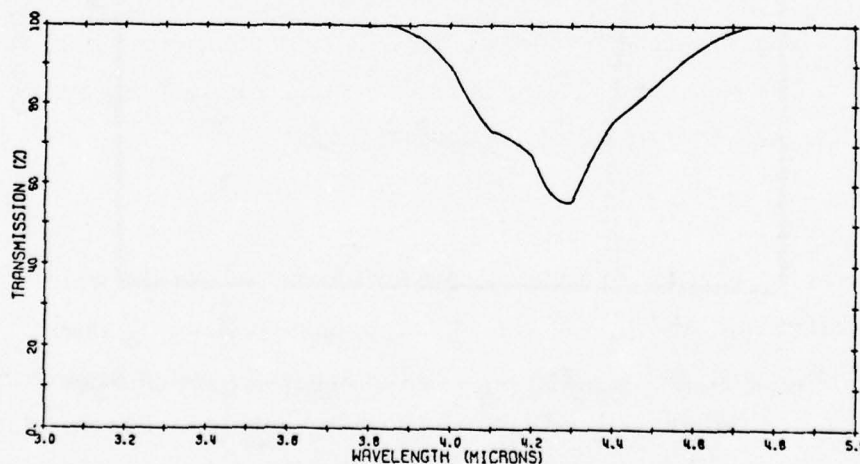


Figure 6. Lowtran Nitrogen Continuum Transmission
Model; 5 km Range, Midlatitude Summer
Atmospheric Model at Sea Level

The Lowtran III model was also supposed to include the 4 μm water continuum [27]: "Absorption coefficients for the water continuum near 10 μm and 4 μm in Lowtran III are based on measurements...". However, in examining the output and the code, it is apparent that this continuum is still being neglected.

There is still some debate about the proper level of the continuum near 4 μm . The generally accepted level is based on extrapolations of data taken by Burch at high temperature, high pressure, and low spectral resolution [27]. Because the continuum absorption is small and has little spectral structure, measurements are difficult even with laboratory path lengths of a kilometer. Recently however, two sets of White cell measurements of total water vapor absorption coefficients have been reported, which correspond to Midlatitude Summer conditions [35, 36]. In general, it seems that currently used extrapolations from Burch data are somewhat higher in transmission than reality. However, they are felt to be valid to within a factor of two [37]. This continuum was incorporated into the Lowtran results for the present study using a special purpose computer code "Tran" (see Appendix A).

In the long wavelength window, the only important continuum absorption is due to water. There is considerable controversy regarding this continuum. It is generally evaluated from:

$$k = w_w (C_s p_w + C_f p_f) \quad (4-7)$$

where k is the continuum absorption coefficient, w_w is the water vapor content, p_w and p_f are the partial pressure of water vapor and foreign gases, and C_s and C_f are the self and foreign broadening absorption coefficients. Lowtran uses measurements of Burch, et. al. [38, 39], McCoy and Rensch [40], and Bignell [41], for the self broadening absorption coefficient, C_s .

Two significant approximations are then invoked:

1. The self broadening absorption coefficient (C_s) does not vary with temperature.
2. The foreign broadening absorption coefficient (C_f) is proportional to the self coefficient (C_s).

The first approximation was probably used for lack of accurate knowledge of the temperature effect. The second was based on a single measurement by McCoy, et. al. [40], with large experimental uncertainty [37]. The value used for the ratio C_f/C_s is 0.005.

Roberts, et. al. [42] have proposed a modified expression which lifts the first approximation, but not the second. It does however, alter the value of C_f/C_s to 0.0008, based on more recent measurements by Long and Burch [42]. The level of C_s was also modified slightly based on more recent measurements by Burch. The temperature dependence of C_s was taken to be:

$$C_s = C_s^0 \exp \left[T_0 \left(\frac{1}{T} - \frac{1}{296} \right) \right] \quad (4-8)$$

where C_s^0 is the value of C_s at 296 K, and T is the temperature in Kelvin. Roberts suggests a value of 1800 K for T_0 .

It should be noted that due to the second approximation, C_f has the same temperature dependency in this model as C_s . There is no reason to expect the same dependency, since two different mechanisms are involved. Indeed, there is evidence that the two parameters should have opposite temperature effects. A model by Kunde [43], treats C_s and C_f separately, and assigns them different (and opposite) temperature dependence.

Sample results for these three models are shown in Figure 7. It is seen that Roberts' model varies with temperature much more

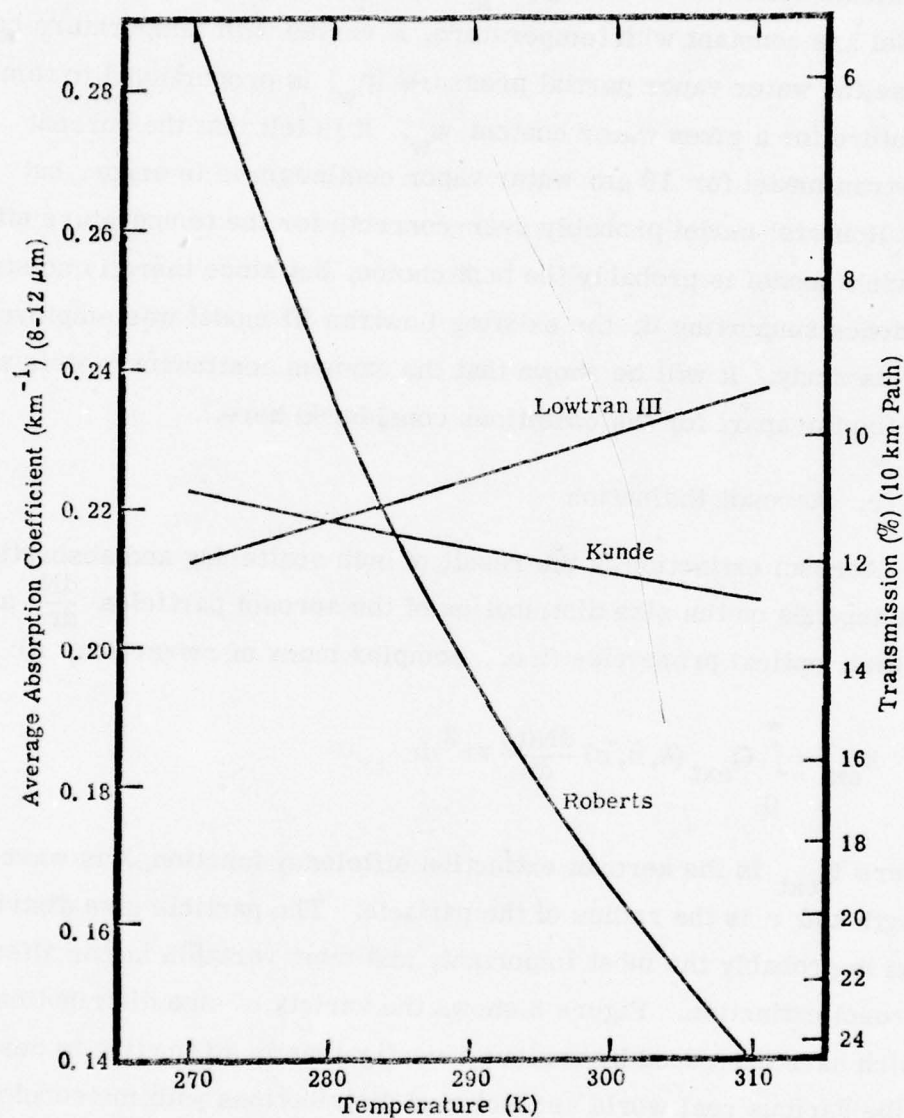


Figure 7. Comparison of Various 8-12 μm Water Continuum Models. Water content (14 gm/m^3) and total pressure (1 atm) correspond to Midlatitude Summer Model.

than the others because both C_s and C_f are assumed to have the same functional behavior. Although C_s (and C_f) in the current Lowtran model are constant with temperature, k varies with temperature because the water vapor partial pressure (p_w) is proportional to temperature for a given water content w_w . It is felt that the current Lowtran model for 10 μm water vapor continuum is in error, but that Roberts' model probably over-corrects for the temperature effect. Kunde's model is probably the best choice, but since there is no strong evidence supporting it, the existing Lowtran III model was employed in this study. It will be shown that the various continuum models are not too far apart for the conditions considered here.

c. Aerosol Extinction

Aerosol extinction is the result of both scattering and absorption, and depends on the size distribution of the aerosol particles $\frac{dN}{dr}$ and on their optical properties (i. e., complex index of refraction, \bar{n}):

$$k_{\text{ext}} = \int_0^{\infty} Q_{\text{ext}}(\lambda, \bar{n}, r) \frac{dN(r)}{dr} \pi r^2 dr \quad (4-9)$$

where Q_{ext} is the aerosol extinction efficiency function, λ is wavelength and r is the radius of the particle. The particle size distribution is probably the most important, and most variable factor affecting aerosol extinction. Figure 8 shows the variety of size distributions which have been used by various investigators in attempting to describe various real world aerosol size distributions with meteorological and geographical parameters. Variables which are often included in such models are relative humidity, wind speed, and the influence of oceanic or urban environments.

The complex index of refraction of the aerosol affects the aerosol extinction through the efficiency function, Q_{ext} . For typical aerosol

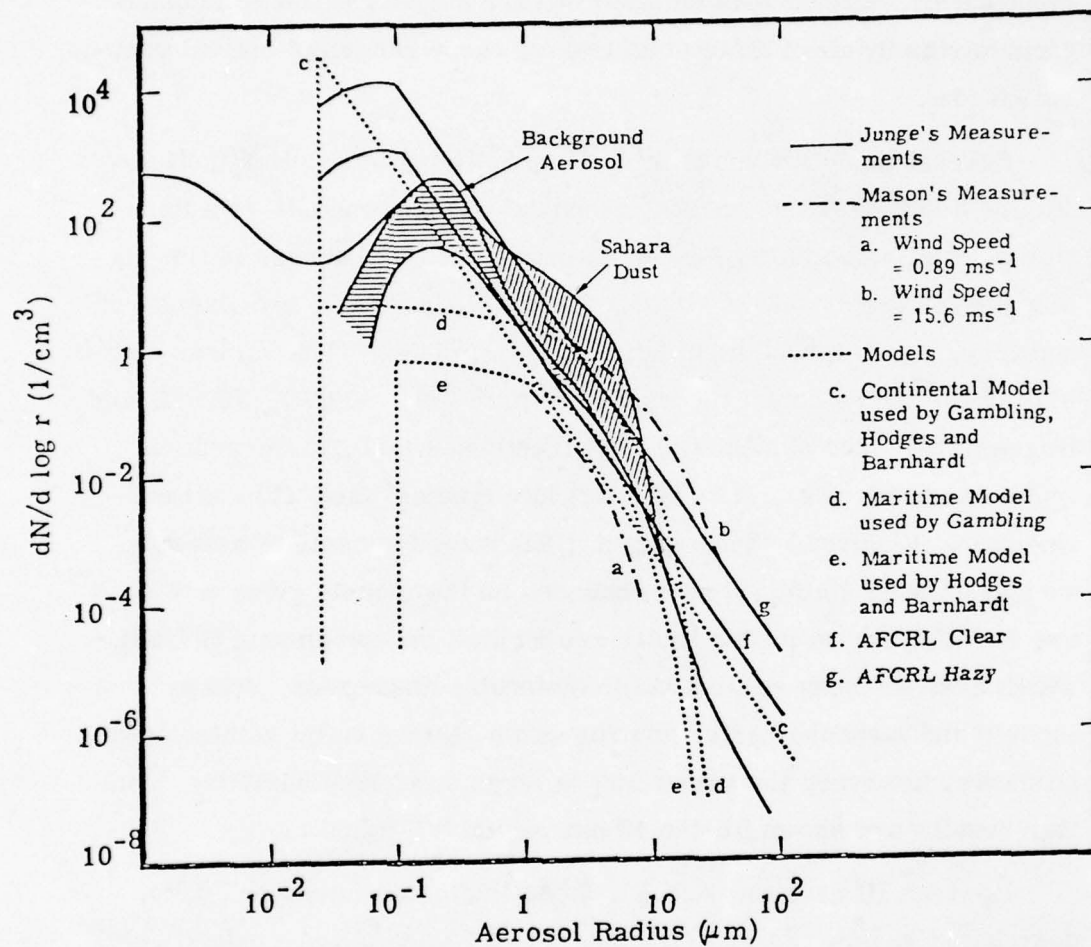


Figure 8. Comparison of Aerosol Size Distributions

materials (e.g., dust, soot, sea salts and water solubles), the real part of the index has values in a relatively narrow range from about 1.2 to 1.8 for the 4 and 10 μm regions [44]. The imaginary part of the index for these materials and spectral regions, ranges from about 10^{-3} to almost unity, but its effect on the extinction coefficient is smaller than that of the real index. For a typical measured size distribution, calculations indicate that the aerosol extinction coefficient varies by about a factor of two for these ranges of optical properties [45].

Several models are available for predicting aerosol extinction. Figure 9 indicates the results of several of these models as a function of relative humidity for the 4 μm region. The curves in this figure are for the models of Gambling [46], Hodges [47], and Barnhardt and Streete [48] in which humidity is a parameter. The various symbols in the figure depict the models of Katz [49], AFCRL [50-54], and Hughes [55]. The numbers in the parentheses indicate the generic type of aerosol (e.g., (1) - all maritime type aerosol, (0) - all continental). Figure 10 shows recent NRL measurements of aerosol extinction near 4 μm [56] superimposed on the models given in Figure 9. Also shown in this figure are British measurements [57, 58], which have not been corrected for molecular absorption. These models and measurements show the same general trend with relative humidity; however, the variability is large at a given humidity. Similar results are shown for the 10 μm region in Figure 11.

Lowtran III uses the AFCRL model indicated (clear and hazy, designated in Lowtran by "visibilities" of 23 and 5 km, respectively) in Figures 9 - 11. It can be seen that the extremes in extinction resulting from this model, almost bracket the extremes indicated by the other models and measurements. It was therefore decided to

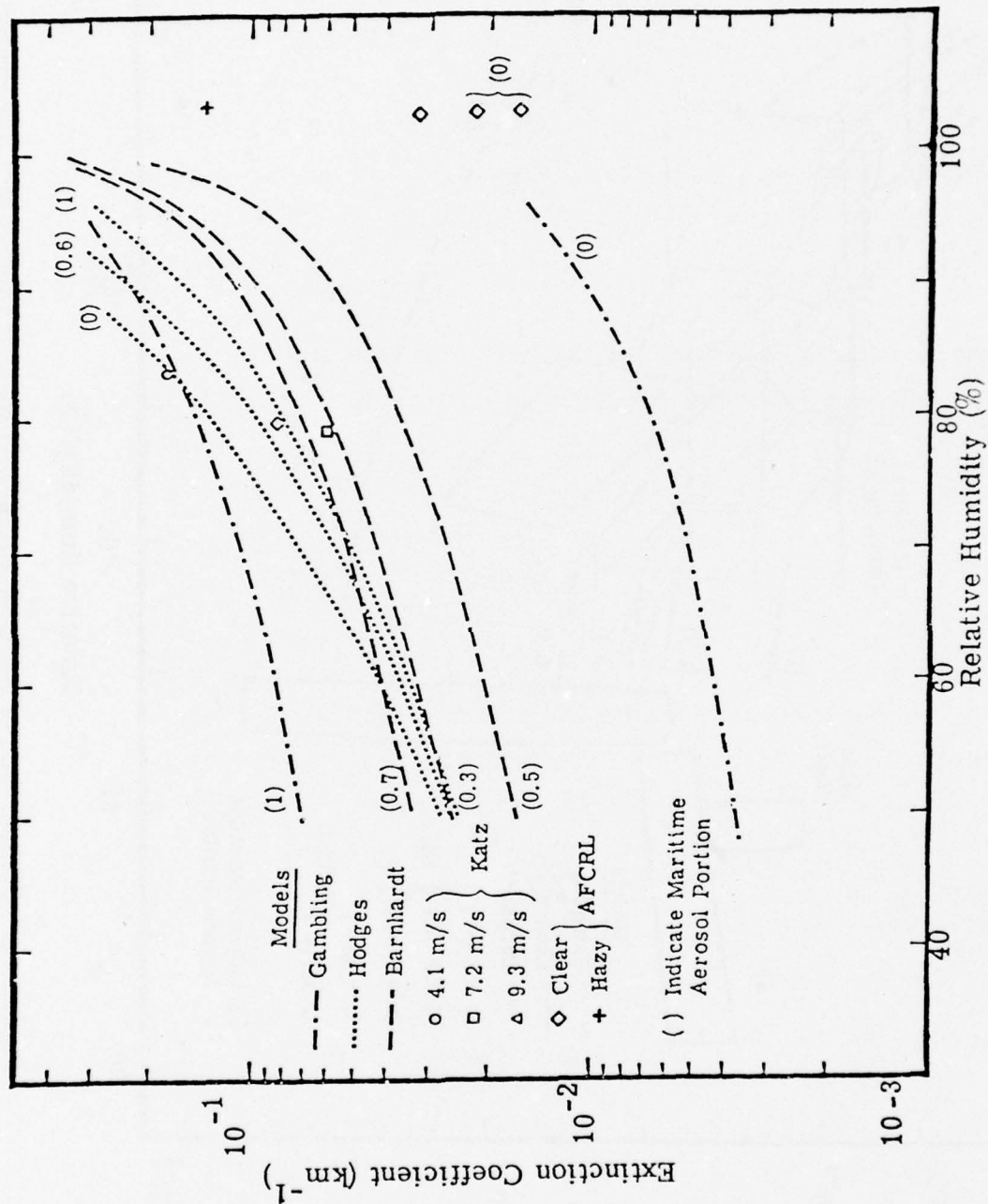


Figure 9. Comparison of Aerosol Extinction Models in $4 \mu\text{m}$ Region

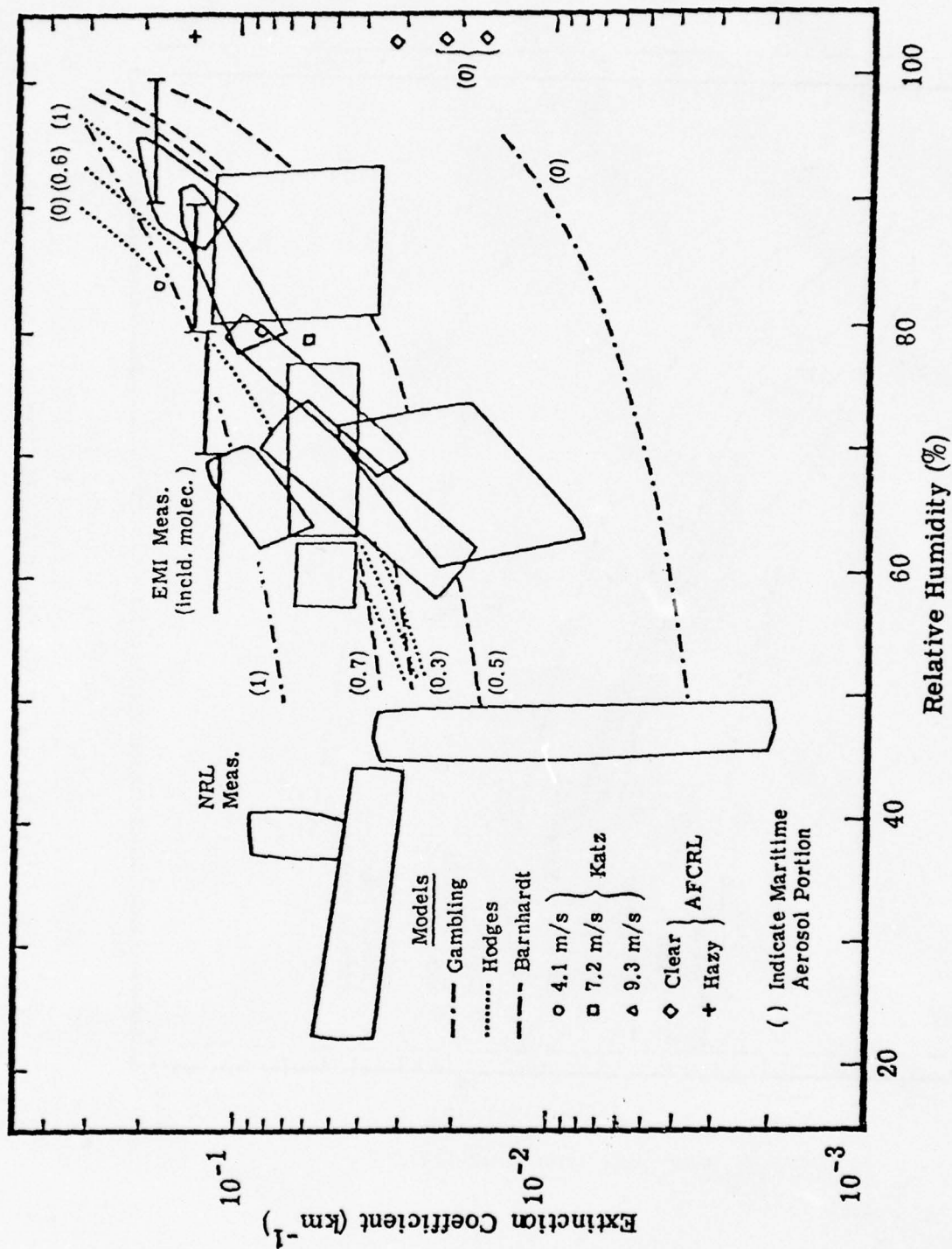


Figure 10. Comparison of Aerosol Extinction Measurements in $4 \mu\text{m}$ Region

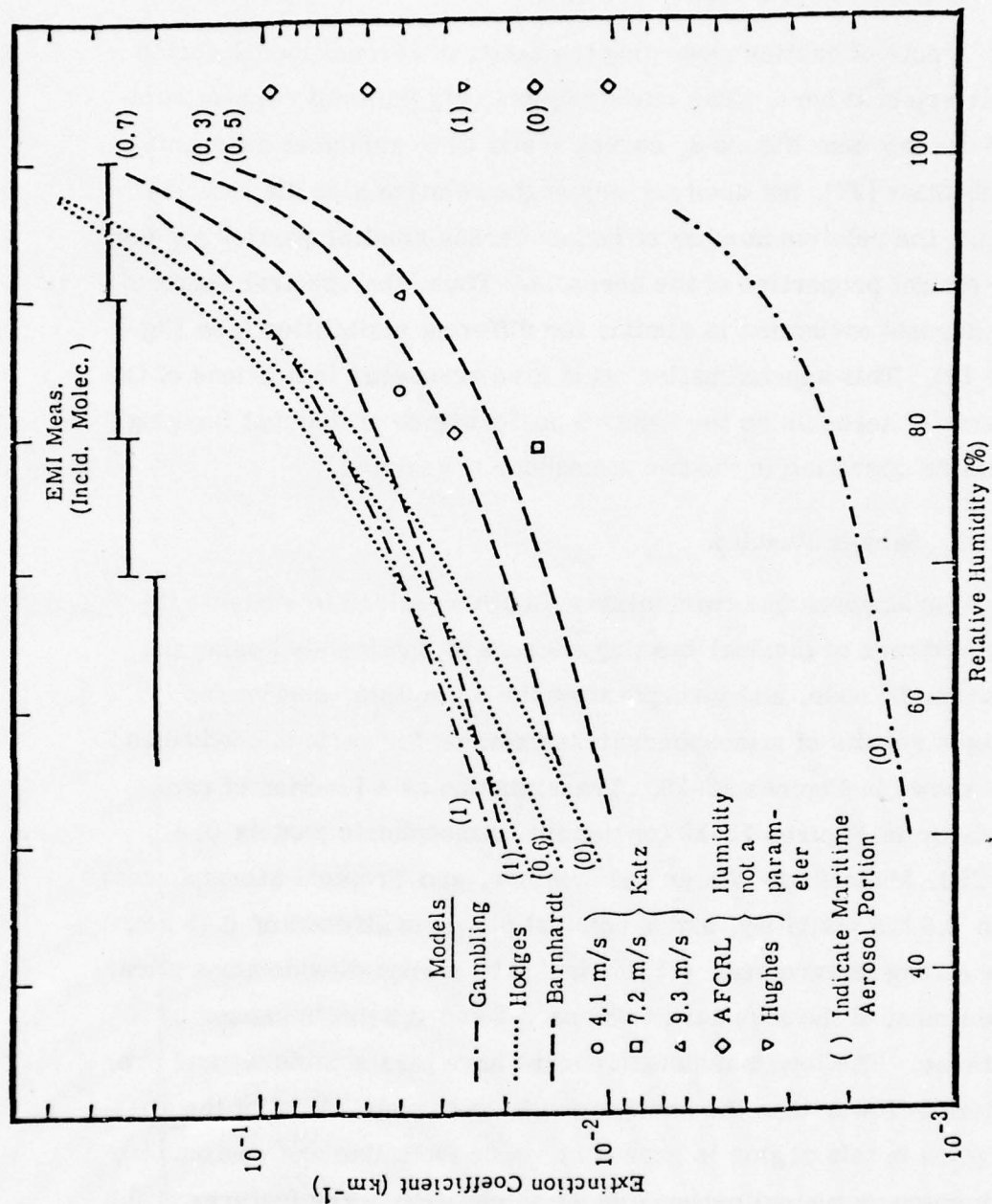


Figure 11. Comparison of Aerosol Extinction Measurements and Models in $10 \mu\text{m}$ Region

employ this model (with one intermediate condition, i. e. , 8.5 km visibility) in the present calculations.

A note of caution regarding the Lowtran aerosol model should be interjected here. The model adjusts only the total aerosol number density (see Figure 8, curves f and g) to arrive at different visibilities [27], but does not adjust the relative size distribution (e. g. , the relative number of larger versus smaller particles), nor the optical properties of the aerosols. Thus, the spectral shape of the aerosol extinction is similar for different visibilities (see Figure 12). This approximation could give erroneous indications of the effects of aerosols on the relative performance of thermal imaging systems operating in the two atmospheric windows.

d. Sample Results

The atmospheric transmission factor required to evaluate the performance of thermal imaging sensors was calculated using the Lowtran III code, and incorporating the 4 μm water continuum. Sample results of atmospheric transmission for various conditions are shown in Figures 13-26. Transmission as a function of range is shown in Figures 13-18 for nominal atmospheric models (i. e. , AFCRL Midlatitude Winter and Summer, and Tropical atmospheres) with 8.5 km visibility, and a nominal platform altitude of 0.75 km. The strong feature near 4.3 μm is due to carbon dioxide absorption, while most of the structure between 3.5 and 3.9 μm is caused by methane. The long wavelength curves have less structure, and are generally lower than the short wavelength curves. Most of the absorption in this region is caused by water (both line and continuum), with some ozone and carbon dioxide attenuation. The features at 9.5 and 9.7 μm are due to ozone, but most of the other features are from water. The cutoff near 8 μm is due to methane and N_2O . Because

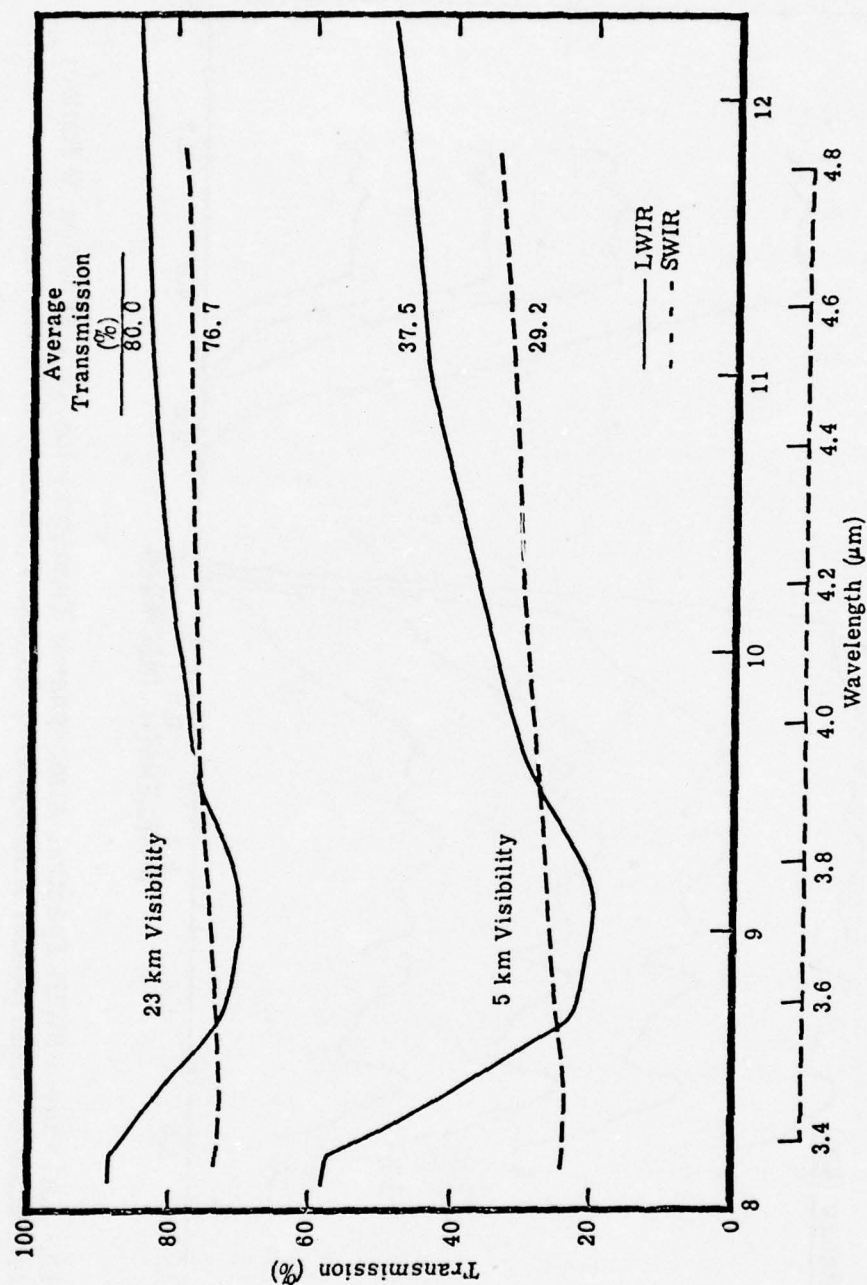


Figure 12. Lowtran III Calculated Aerosol Spectral Transmission for Two Visibilities in the Long Wavelength and Short Wavelength Infrared (LWIR & SWIR) Atmospheric Windows

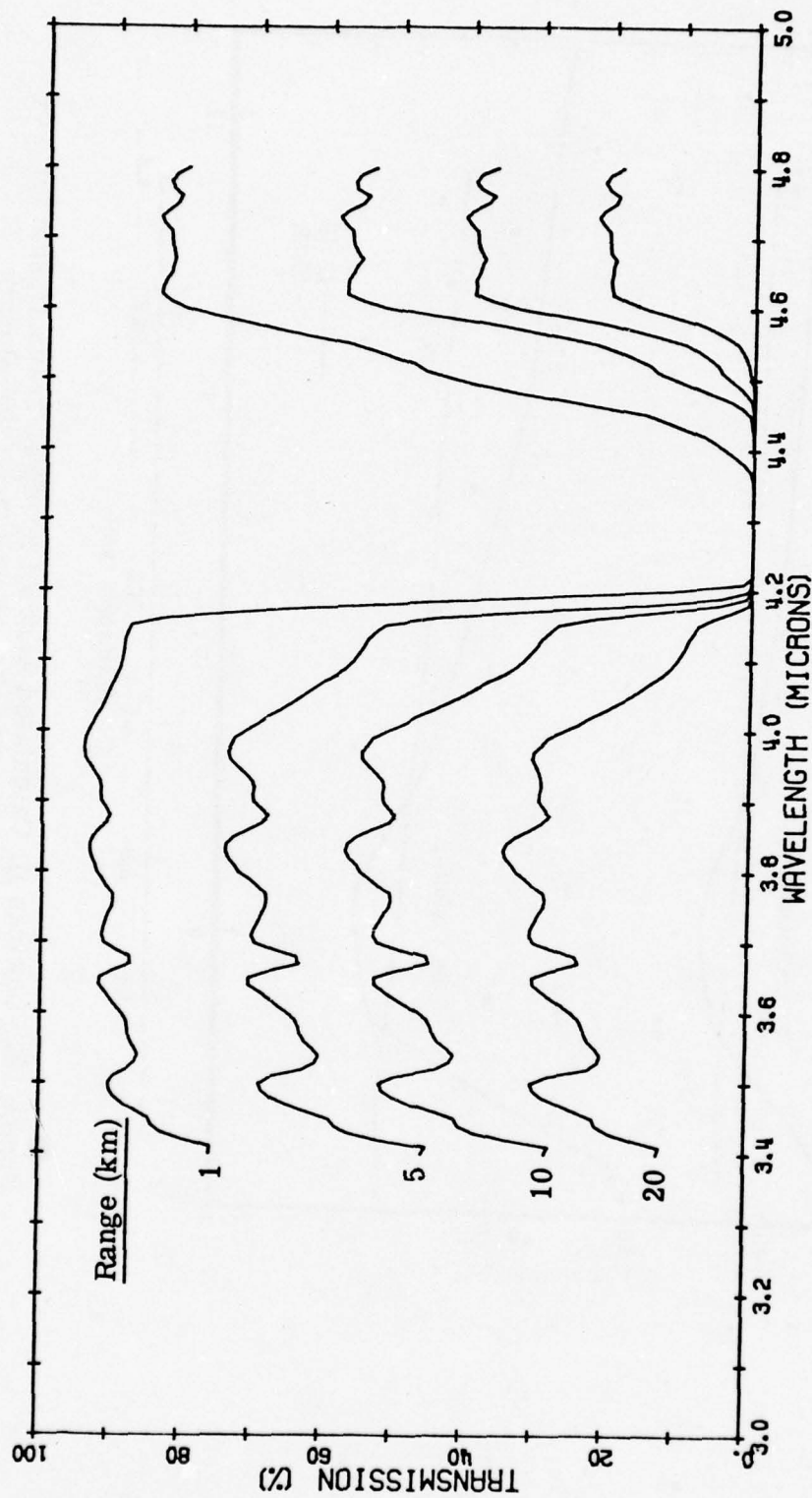


Figure 13. Calculated SWIR Spectral Atmospheric Transmission as a Function of Range;
Midlatitude Winter Model Atmosphere, 8.5 km Visibility, 0.75 km Altitude

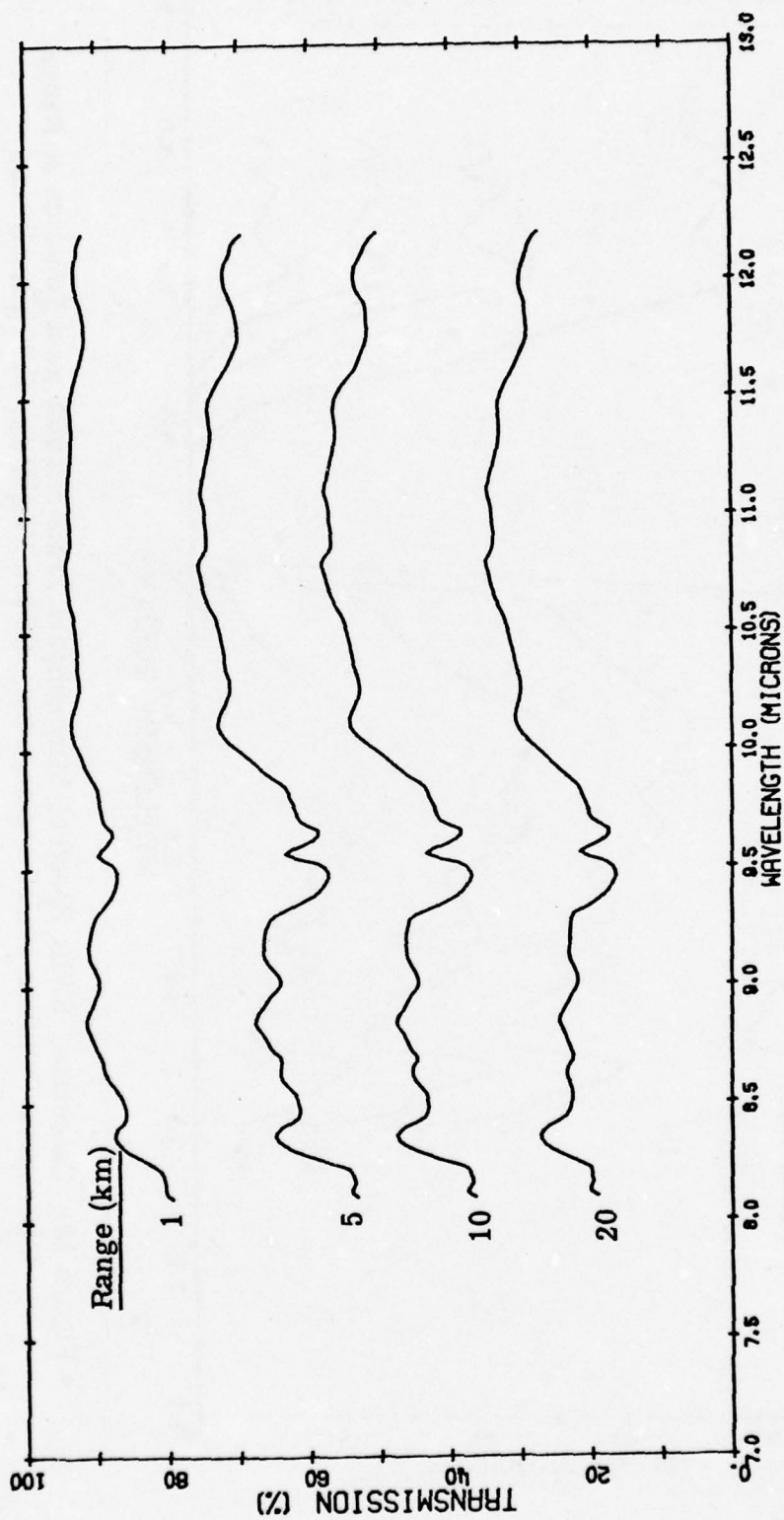


Figure 14. Calculated LWIR Spectral Atmospheric Transmission as a Function of Range;
Midlatitude Winter, 8.5 km Visibility, 0.75 km Altitude

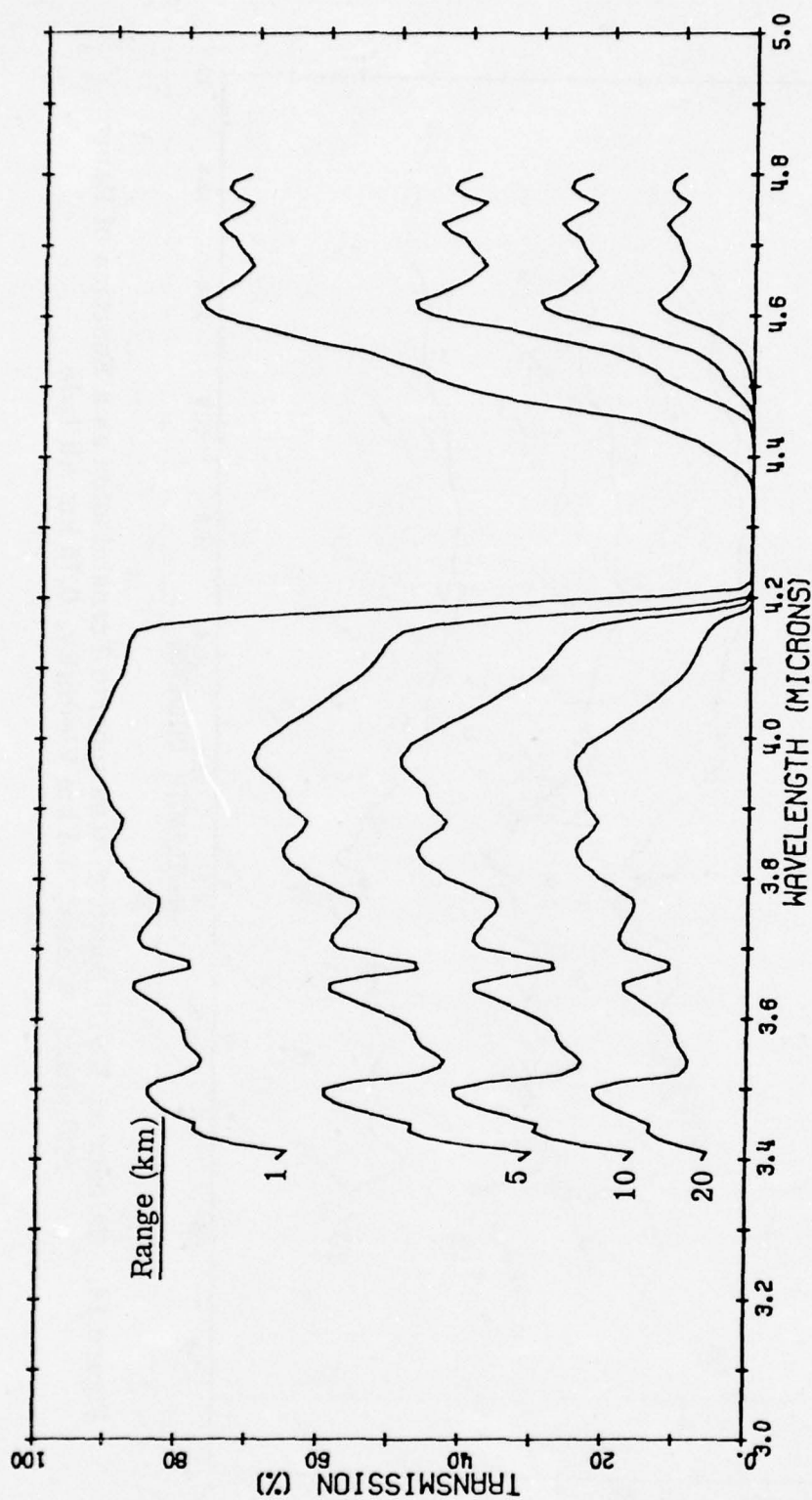


Figure 15. Calculated SWIR Spectral Atmospheric Transmission as a Function of Range;
Midlatitude Summer Model Atmosphere, 8.5 km Visibility, 0.75 km Altitude

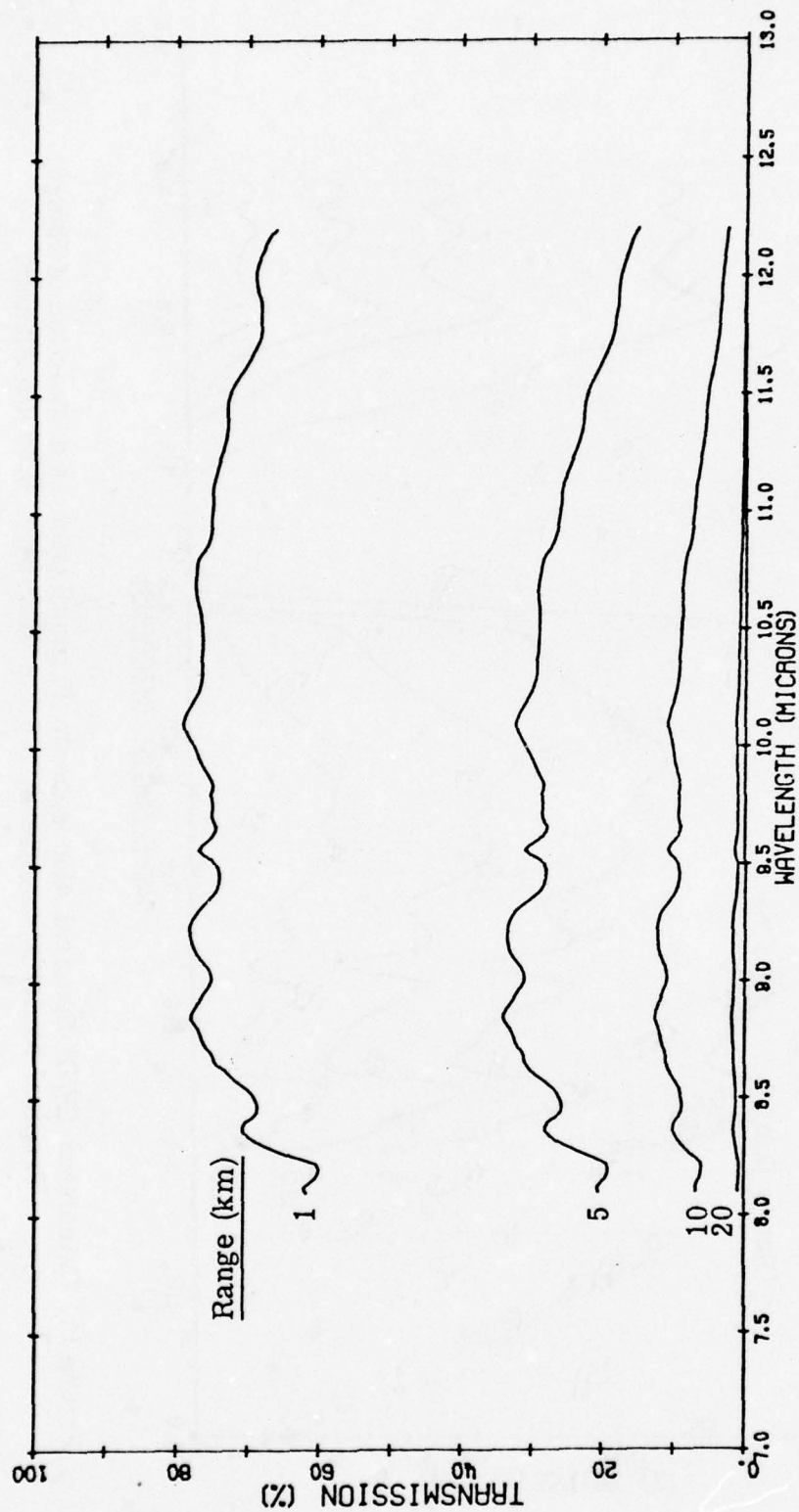


Figure 16. Calculated LWIR Spectral Atmospheric Transmission as a Function of Range;
Midlatitude Summer, 8.5 km Visibility, 0.75 km Altitude

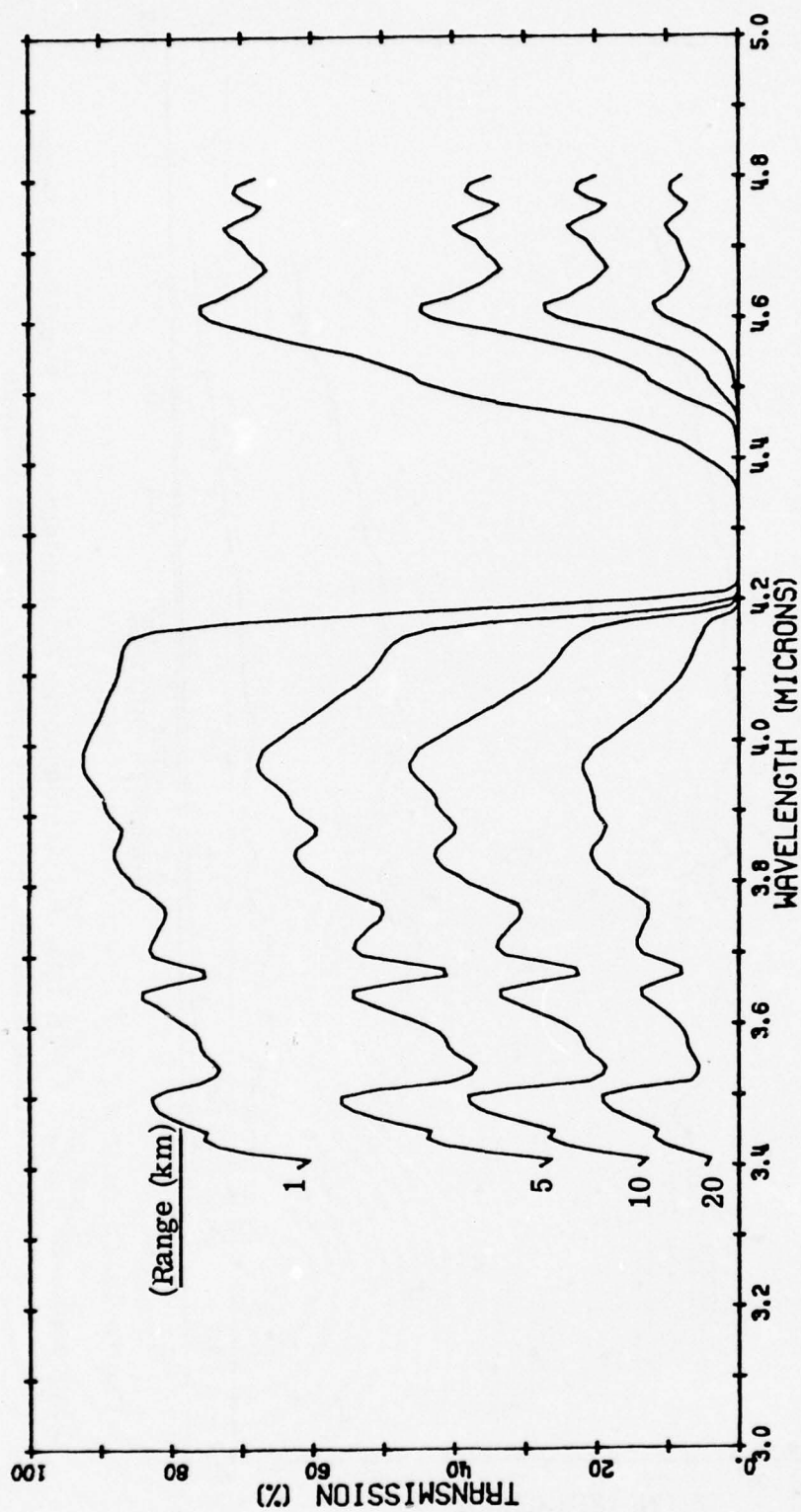


Figure 17. Calculated SWIR Spectral Atmospheric Transmission as a Function of Range;
Tropical Model Atmosphere, 8.5 km Visibility, 0.75 km Altitude

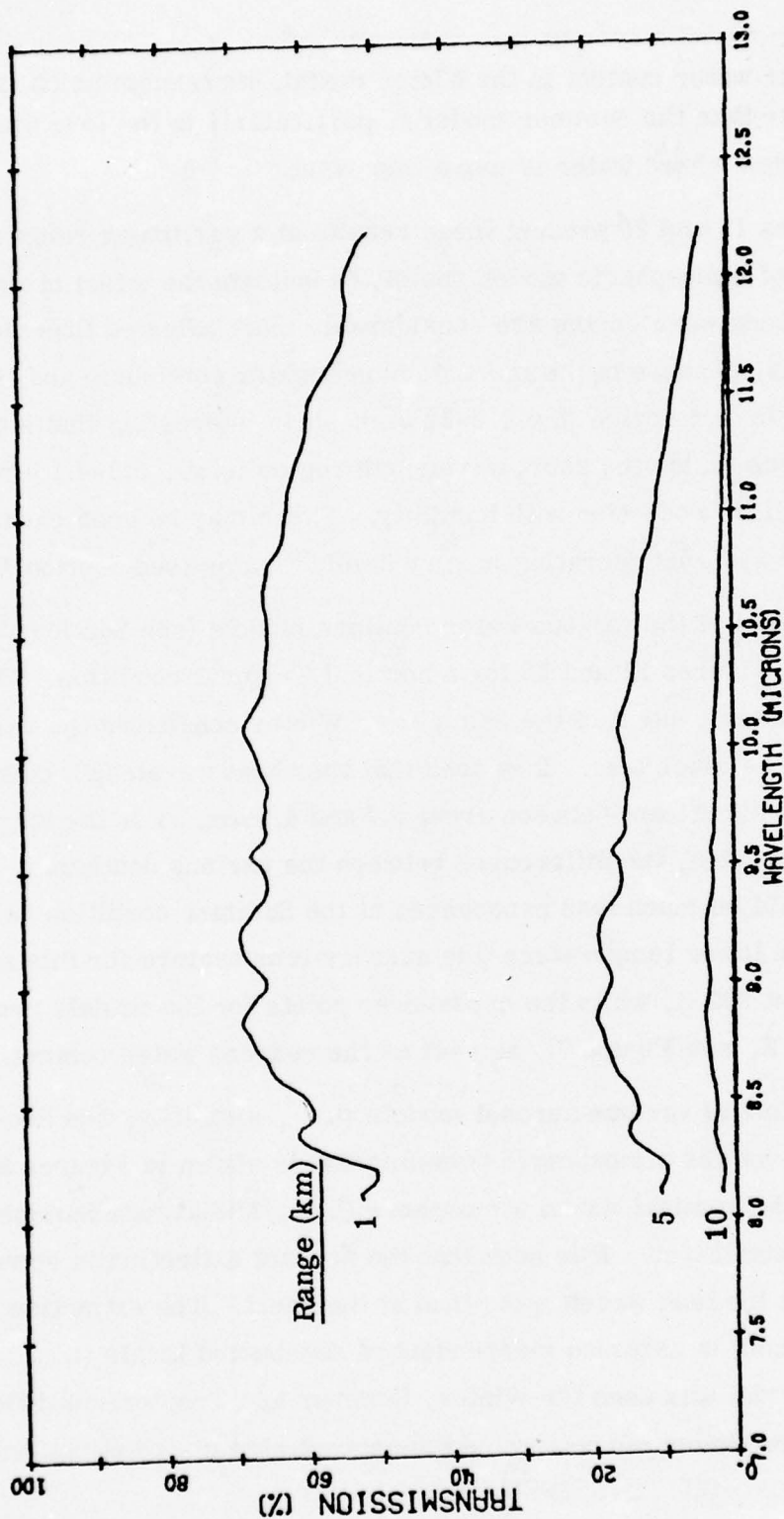


Figure 18. Calculated LWIR Spectral Atmospheric Transmission as a Function of Range;
Tropical Model Atmosphere, 8.5 km Visibility, 0.75 km Altitude

of the lower water content in the Winter model, its transmission is much better than the Summer model's, particularly in the long wavelength window where water is more important.

Figures 19 and 20 present these results at a particular range as a function of atmospheric model, mainly to indicate the effect of water content. Long wavelengths are considerably more affected than short wavelengths, because of the more dominant water continuum and line absorption in that region (i. e. , 8-12 μm). It is interesting that some narrow bands inside the short wavelength region (e. g. , 3.8-4.1 μm) show very little reduction with humidity. These may be good candidate regions for systems operating in very humid locales (see Section V).

The effect of the various water continua models (see Section IV, #b), is shown in Figures 21 and 22 for a nominal Tropical condition. For the lower water content of the Summer or Winter conditions the variations would be much less. It is seen that the short wavelength continuum is only significant between about 3.5 and 4.2 μm . For the long wavelength region, the differences between the various continuum models would be much less pronounced at the Summer condition because of the lower temperature (the average temperature for this slant path is about 292 K, while the cross-over points for the models are around 283 K, see Figure 7), as well as the reduced water content.

The effect of various aerosol models (i. e. , visibility, see Section IV, #c), on the atmospheric transmission is shown in Figures 23 and 24 for the nominal model atmosphere (i. e. , Midlatitude Summer) at nominal conditions. It is seen that the aerosol extinction is somewhat less at the long wavelengths than at the short. The extinction due to aerosols is assumed independent of season and locale (i. e. , the same model was used for Winter, Summer and Tropical conditions). This is certainly not correct since the aerosol size distributions and

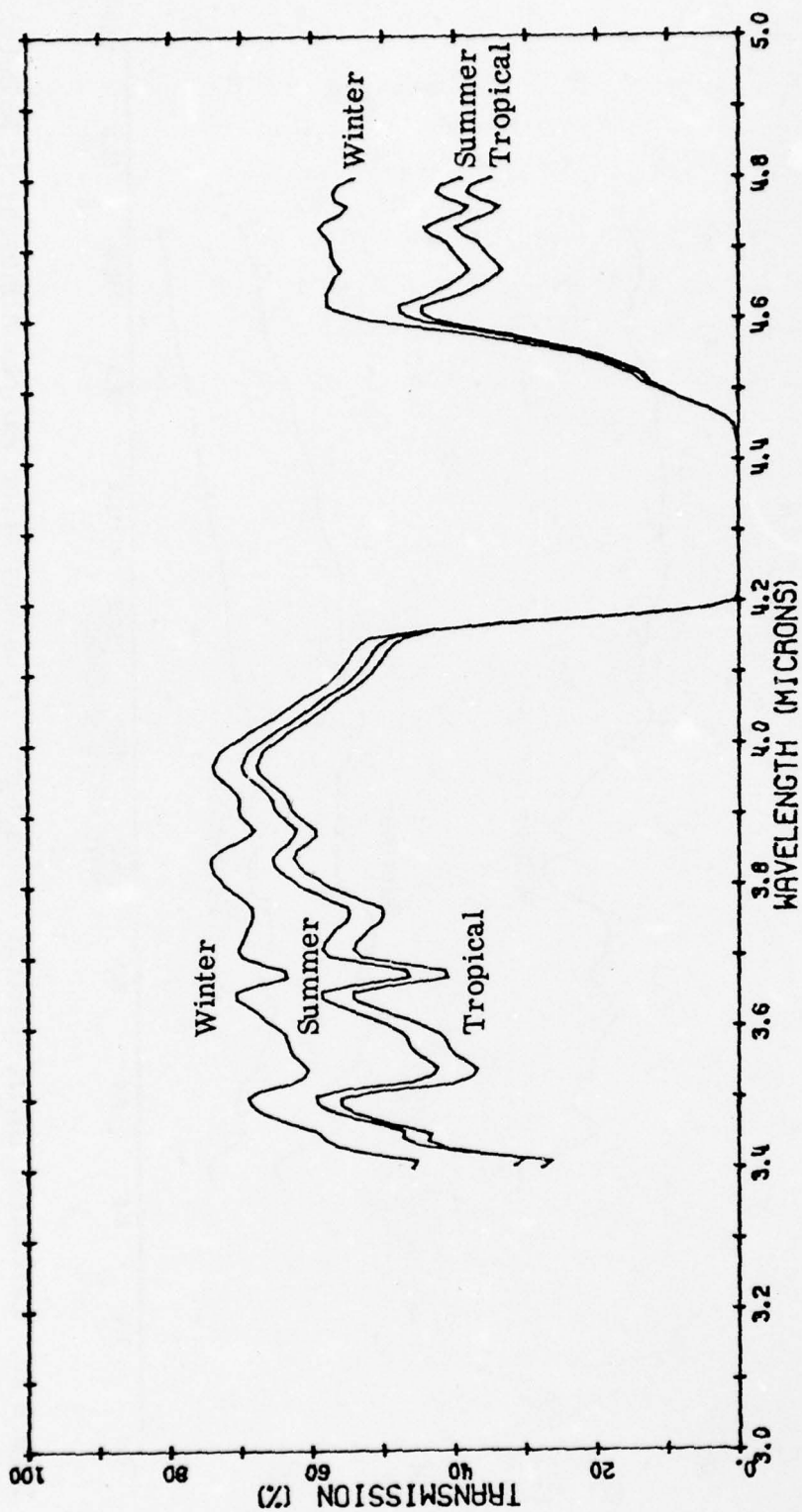


Figure 19. Calculated SWIR Spectral Atmospheric Transmission for Various Atmospheric Models;
8.5 km Visibility, 0.75 km Altitude, 5 km Range

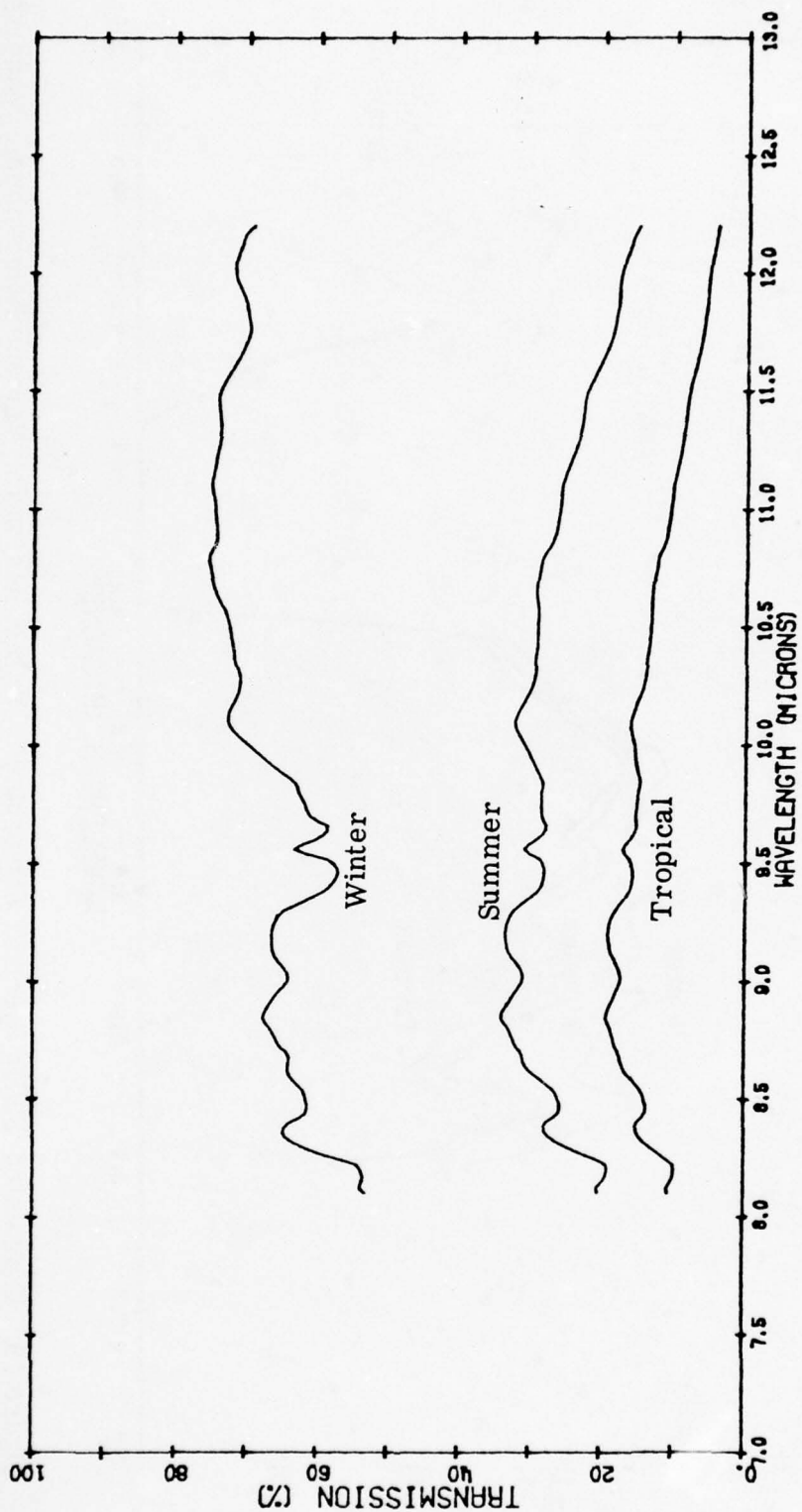


Figure 20. Calculated LWIR Spectral Atmospheric Transmission for Various Atmospheric Models;
8.5 km Visibility, 0.75 km Altitude, 5 km Range

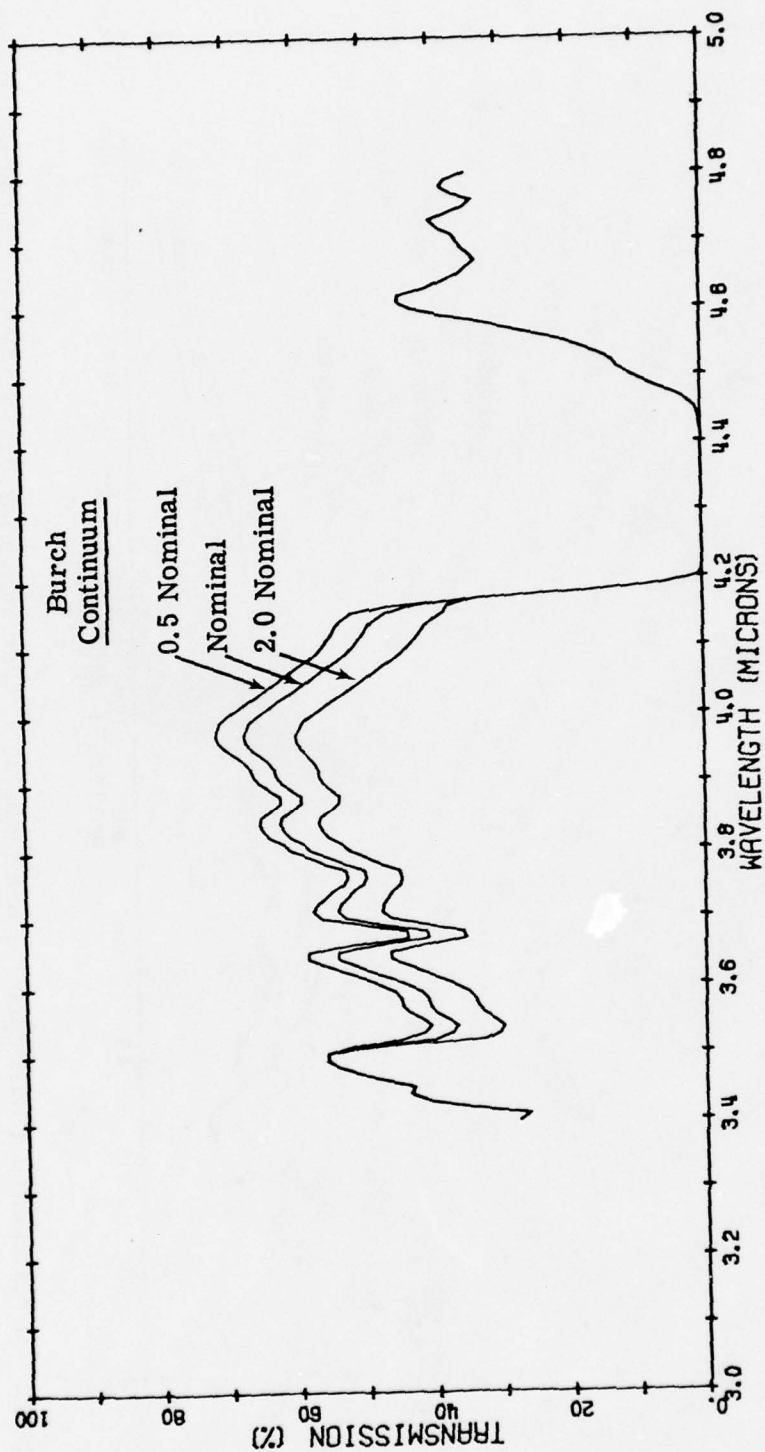


Figure 21. Calculated SWIR Spectral Atmospheric Transmission for Various Water Continuum Models;
Tropical Model Atmosphere, 8.5 km Visibility, 0.75 km Altitude,
5 km Range

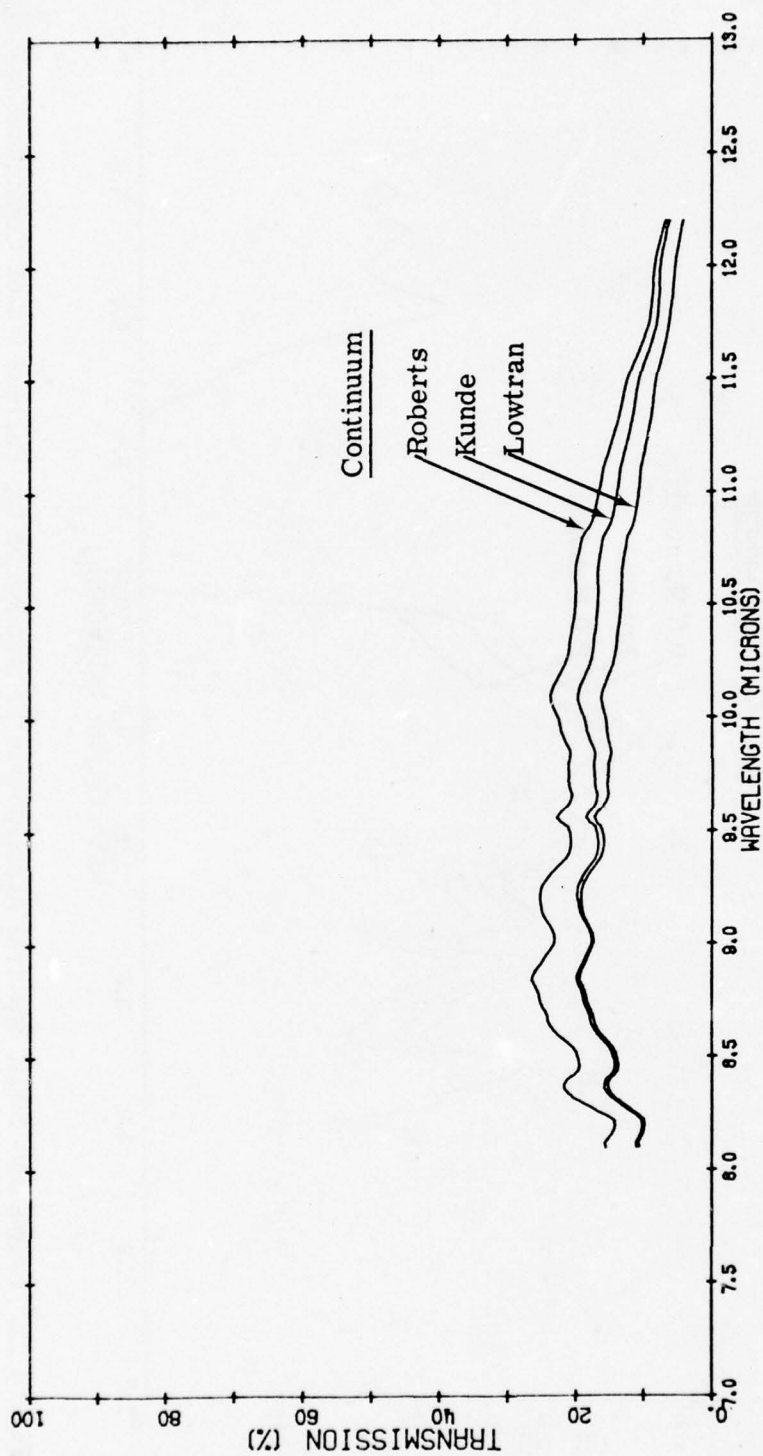


Figure 22. Calculated LWIR Spectral Atmospheric Transmission for Various Water Continuum Models;
Tropical Model Atmosphere, 8.5 km Visibility, 0.75 km Altitude,
5 km Range

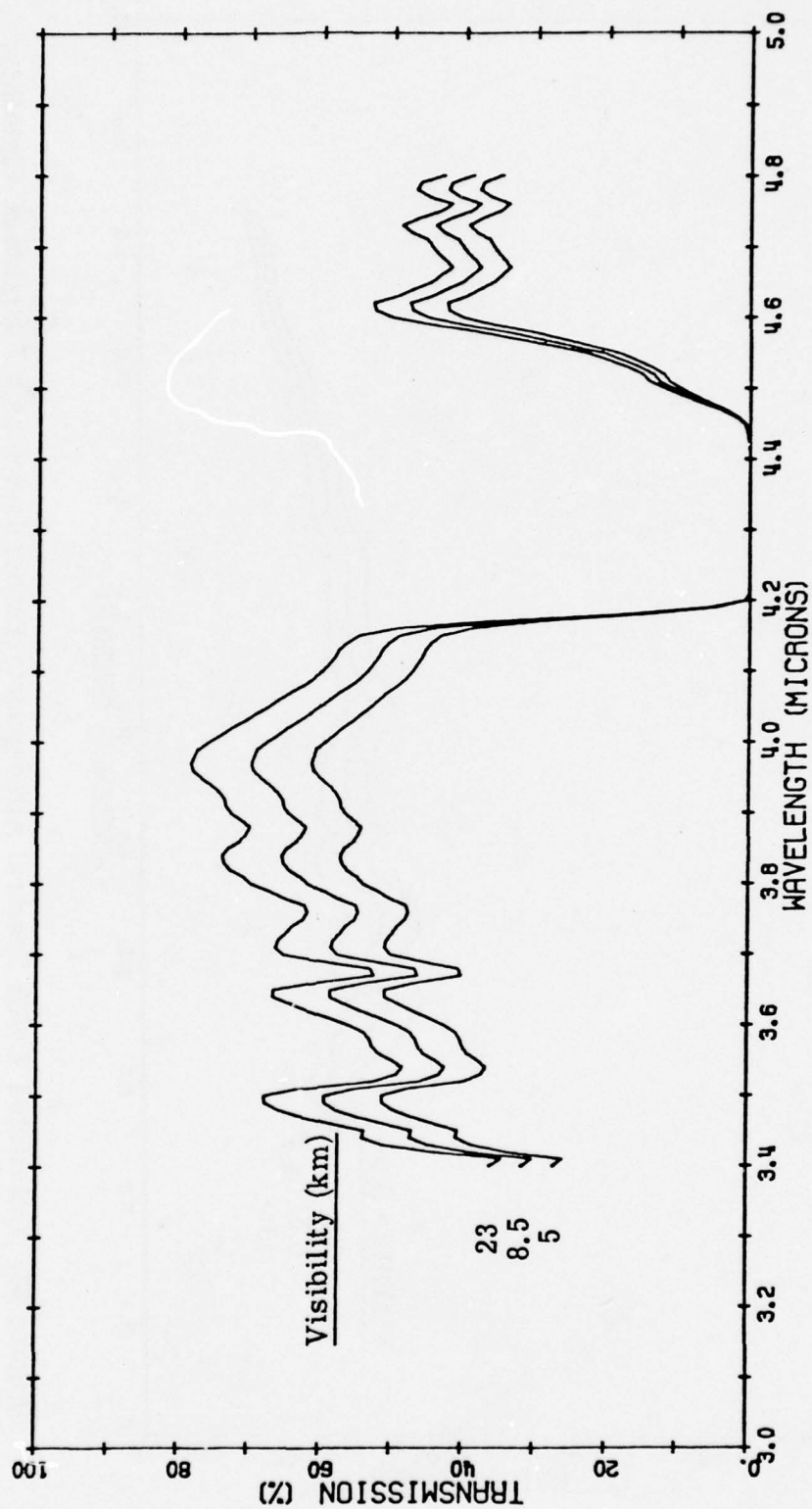


Figure 23. Calculated SWIR Spectral Atmospheric Transmission as a Function of Visibility; Midlatitude Summer Model Atmosphere, 5 km Range, 0.75 km Altitude

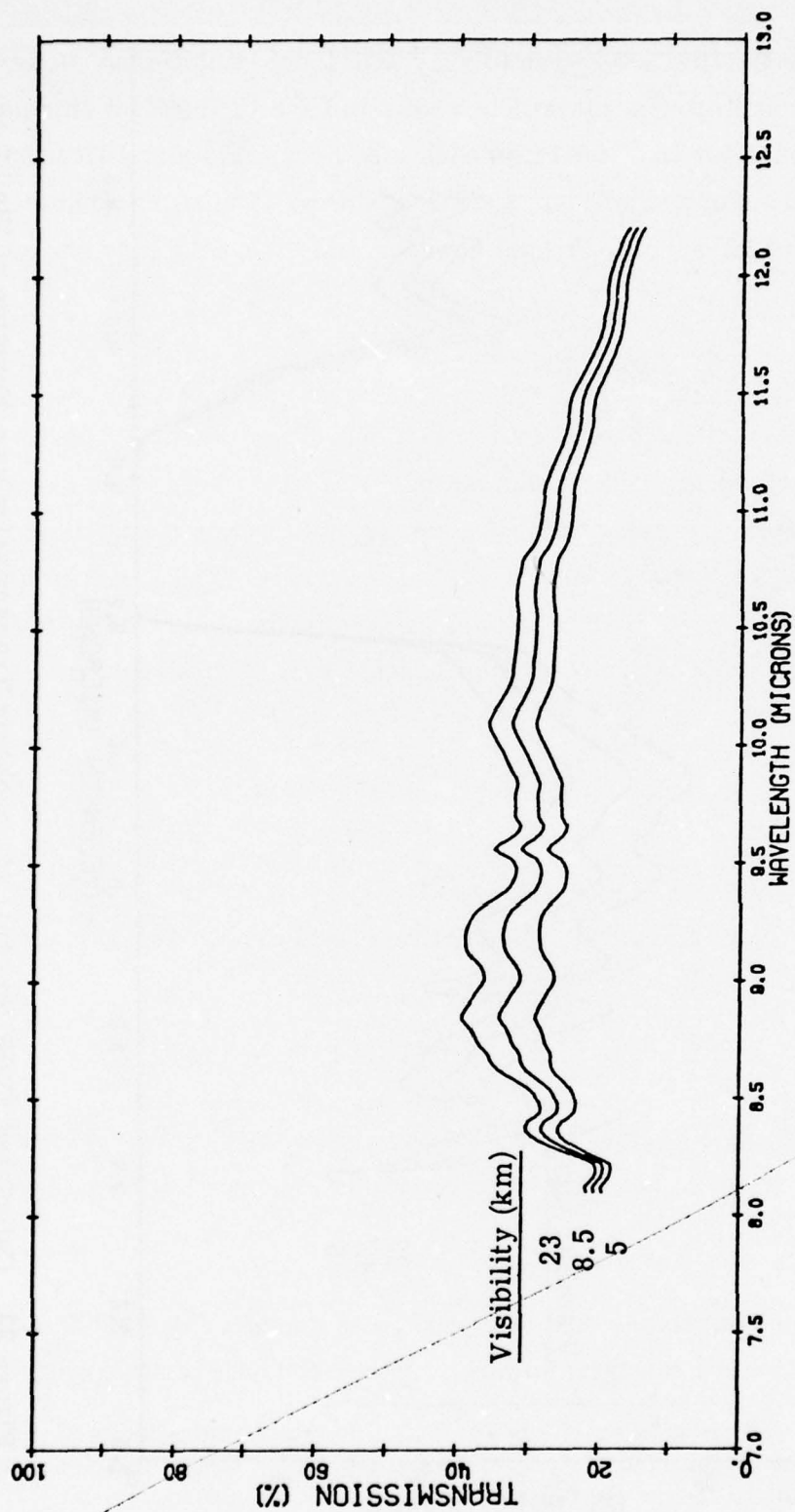


Figure 24. Calculated LWIR Spectral Atmospheric Transmission as a Function of Visibility;
Midlatitude Summer Model Atmosphere, 5 km Range, 0.75 km Altitude

optical properties are known to vary with these conditions. However, since aerosol attenuation will be shown to have little effect on relative performance for the Lowtran model used here, this simplification will not introduce any significant additional error. If a more sophisticated aerosol model were to be used however, this inconsistency should be corrected.

3. Background Radiance

The denominator of Equation 4-2, describing Barhydt's performance model involves the radiance of the background. Background radiance, for a thermal imager viewing ground targets through a long atmospheric path, is comprised of radiance from the terrain (L_g), and from the atmospheric path (L_p). The former component is attenuated by the atmosphere, while the latter component (as it is generally defined and calculated*) is not:

$$\left(\frac{\partial L}{\partial \lambda}\right)_b = \tau_a(\lambda) \left(\frac{\partial L}{\partial \lambda}\right)_g + \left(\frac{\partial L}{\partial \lambda}\right)_p \quad (4-10)$$

Previous analyses of this type (see Section III), have neglected the path radiance term, and apparently also neglected the atmospheric attenuation of the terrain radiance:

$$\left(\frac{\partial L}{\partial \lambda}\right)_b \cong \left(\frac{\partial L}{\partial \lambda}\right)_g \quad (4-11)$$

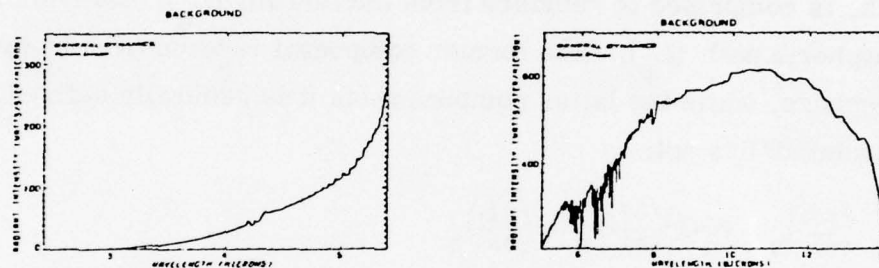
Although these two approximations are compensating, the end result certainly is not exact. The effect of this is discussed in Section V.

a. Terrain Radiances

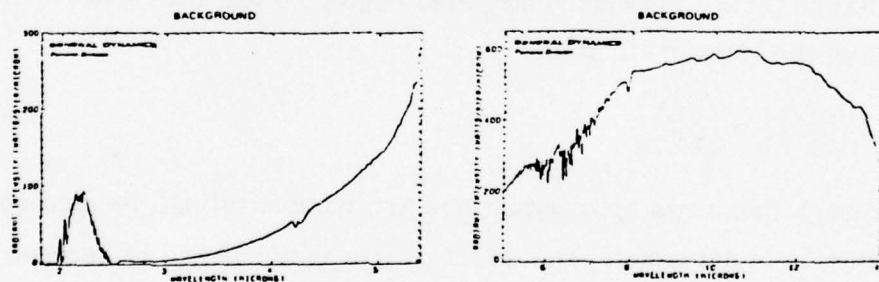
Previous analyses of this type have assumed a simple 300 K black-body function for the terrain (and with the above approximations, the

* Path radiance is calculated by considering simultaneous absorption and emission of each segment of the path. Thus, the attenuation is accounted for in the calculation.

background radiance). Although this is certainly a good approximation for first order analyses (especially at long wavelengths), it can deviate significantly from reality. In particular, there can be considerable solar reflection in the short wavelength region during the day. In the present study, actual measurements of terrain spectral radiant intensities by Smith and Blay [59] have been employed. These measurements were taken from relatively short ranges ($\sim 80\text{m}$), so atmospheric attenuation effects were minimal. Both day and night measurements were made with two high resolution interferometer-spectrometers for the two spectral regions (see Figure 25).



a. Nighttime Measurements



b. Daytime Measurements

Figure 25. Measured Spectral Radiant Intensity of Typical Terrain Backgrounds by Smith and Blay [59].

These measurements were converted to radiances in quantum units by the following procedure. First, the measurements were normalized to their effective radiating areas by dividing by the field of view - range squared product to give radiance:

$$\left(\frac{\partial L(\lambda)}{\partial \lambda}\right)_m = \left(\frac{\partial J(\lambda)}{\partial \lambda}\right) / (\omega R^2) \quad (4-12)$$

These results were then roughly fit with blackbody curves of temperature T_{eff} , and the effective spectral emittance of the background derived:

$$\epsilon(\lambda) = \left(\frac{\partial L(\lambda)}{\partial \lambda}\right)_m / \left[\frac{\partial L(\lambda, T_{\text{eff}})}{\partial \lambda}\right]_{\text{BB}} \quad (4-13)$$

Using the effective temperature of the blackbody function (T_{eff}), and the derived emittance (ϵ), the spectral radiance in quantum units was evaluated:

$$\left(\frac{\partial L^*}{\partial \lambda}\right)_g = \epsilon(\lambda) \left[\frac{\partial L^*(\lambda, T_{\text{eff}})}{\partial \lambda}\right]_{\text{BB}} \quad (4-14)$$

where the standard Planck function for spectral radiance in quantum units was used:

$$\left[\frac{\partial L^*(\lambda, T_{\text{eff}})}{\partial \lambda}\right]_{\text{BB}} = C_1 \lambda^{-4} \left[\exp\left(\frac{C_2}{\lambda T_{\text{eff}}}\right) - 1 \right]^{-1} \quad (4-15)$$

Results of this calculation are shown in Figure 26 for day and night conditions in the two spectral regions. In the long wavelength region, the two curves are very similar as might be expected, since the air temperature was only 4 K cooler during the night measurement than during the day measurement. In the short wavelength region, the radiances during the day are typically almost a factor of two above those during the night. Unfortunately these measurements are only for one locale (and one type of terrain) and one season:

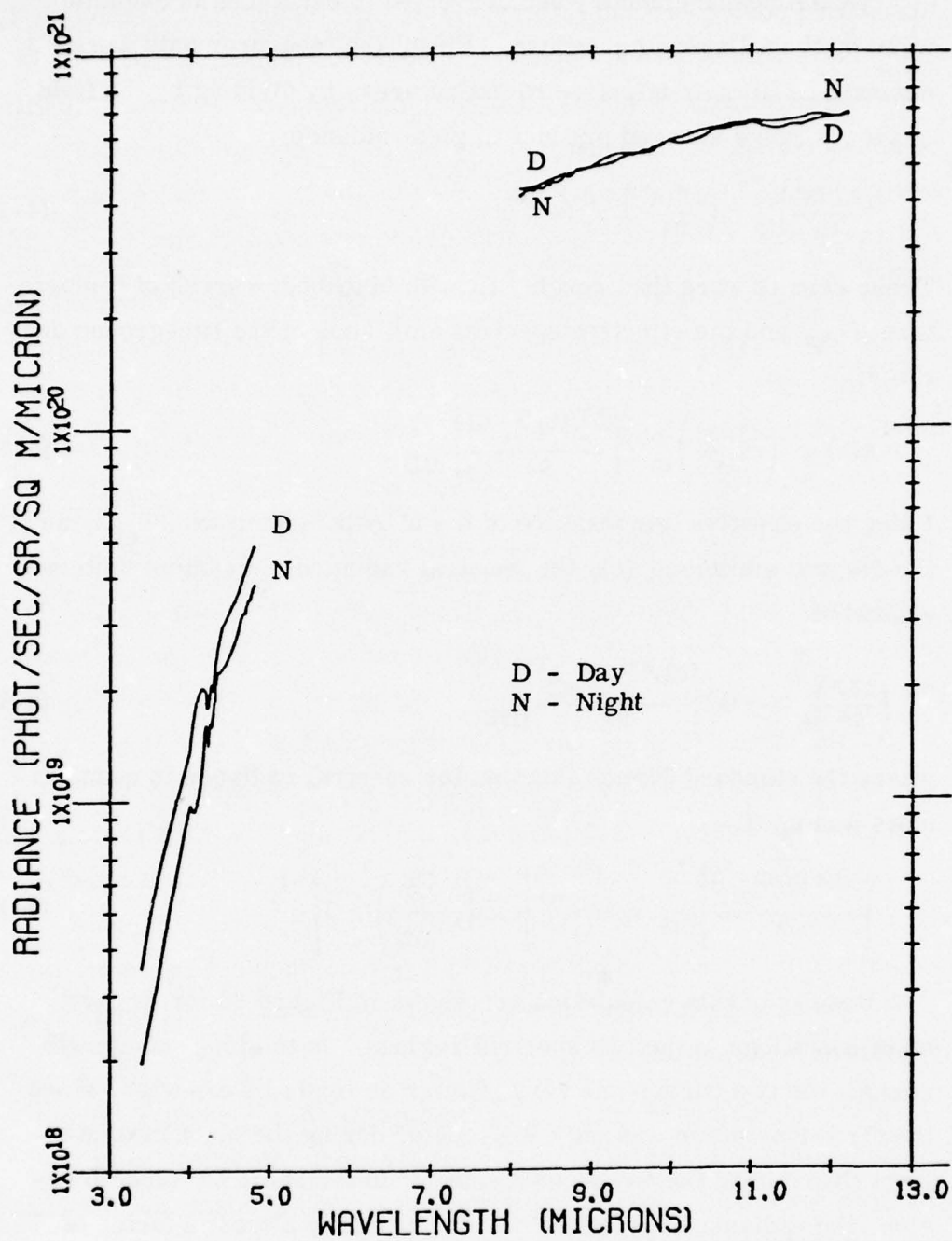


Figure 26. Measured Spectral Terrain Radiance by Smith and Blay [59]

Aberdeen Proving Grounds, Maryland in September. Thus, arbitrarily using these values with atmospheric models for Summer, Winter and Tropical conditions is somewhat of an inconsistency. However, it will be shown (see Section V) that the relative performance of thermal imaging systems is not strongly influenced by the level of the terrain radiance, so it is felt that this inconsistency is not significant.

In addition to these measurement-derived terrain radiances, theoretical radiances were also employed in some of the performance calculations. These theoretical radiances were calculated directly from the Planck function (Equation 4-15) for various temperatures (see Figure 27).

b. Path Radiances

The effective radiance for the atmosphere in the viewing path, arises from the simultaneous absorption and emission of the consecutive portions of the path as well as scattering of radiation (from sources outside the line of sight) by the atmosphere into the line of sight. Calculation of this radiance is very similar in many respects to the calculation of atmospheric transmission, in that the same band models and aerosol scattering model can be used. Indeed, an SAI atmospheric transmission code "Radst" [60], calculates both transmission and path radiance simultaneously (unfortunately Lowtran does not currently include this feature although there apparently are plans to incorporate it in a future modification).

The computer code Radst was employed in this study to evaluate the path radiance contribution to the background. Modifications to this code were made, so that the atmospheric and aerosol models were consistent with those of Lowtran. One exception to this was the short wavelength water continuum, which was incorporated in the Lowtran

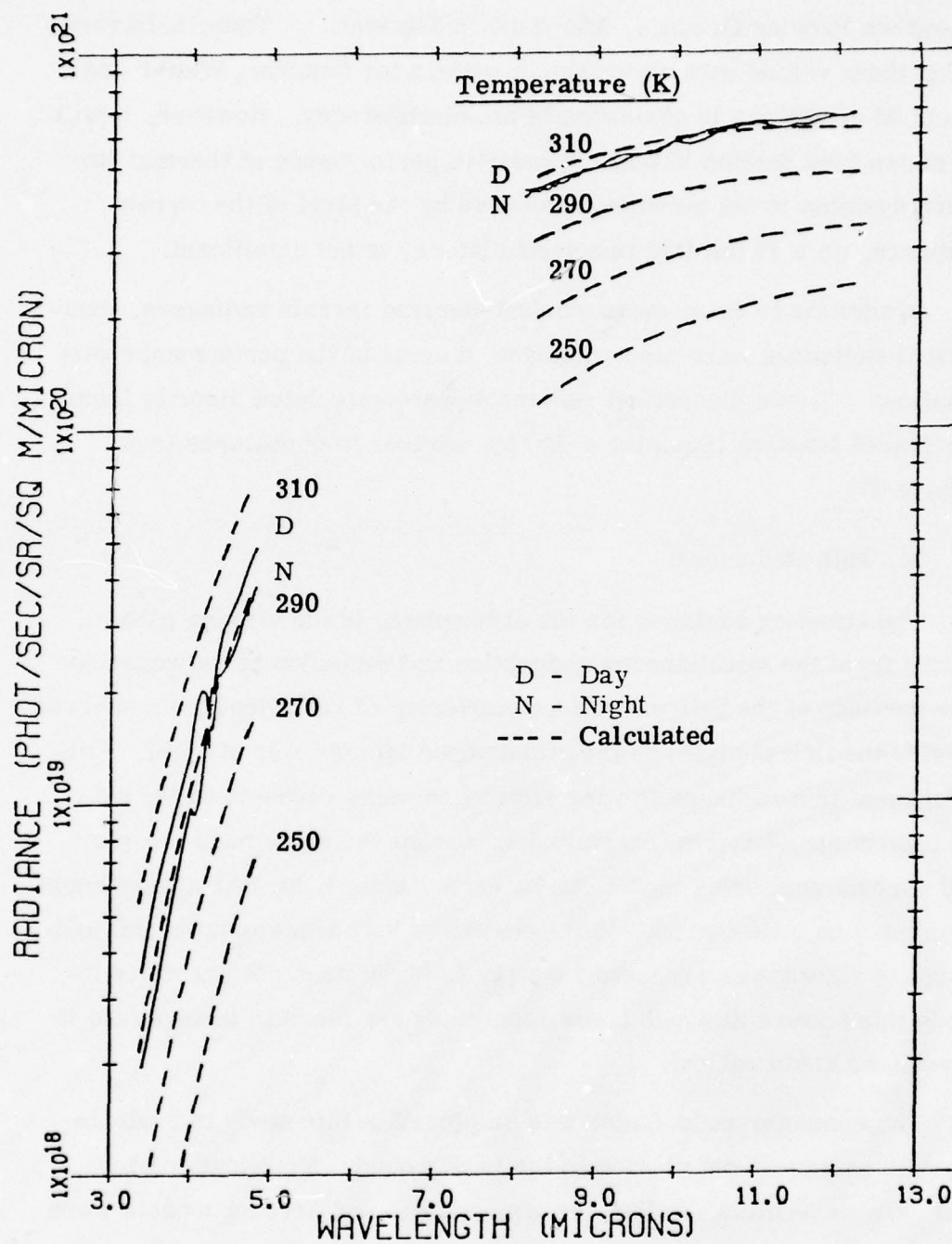


Figure 27. Comparison of Calculated and Measured Spectral Terrain Radiance

results, but unfortunately not in those of Radst. It was felt that this modification was beyond the scope of the present effort, and would have minor impact on the performance calculations. The Radst results were converted to quantum units (i. e., from watts to photons/sec) in the subsequent special purpose code "Path."

Sample results from these codes are shown in Figures 28-37 for various conditions. Figures 28-33 present the calculated spectral path radiance as a function of range for both spectral regions and all seasons. These results are similar to the atmospheric transmission calculated by Lowtran (see Figures 13-18), but with roughly an inverse character. That is, where the transmission is large the path radiance is small, and vice versa. Also the path radiance increases with increasing range, decreasing visibility and increasing humidity while the transmission has the opposite dependency on these parameters. It may also be noted that the calculated path radiance has more spectral structure than the calculated transmission. This is an artifact of the respective codes used to generate the results; Lowtran has lower spectral resolution than Radst. The upper limits to the path radiance at long ranges (e. g., between 4.2 and 4.6 μm) and in the long wavelength window) corresponds to gray body curves at some effective atmospheric temperature. Note that the Tropical, long wavelength region (see Figure 33), attains this condition more completely than the short wavelength region, due to its larger opacity. The Winter long wavelength region (see Figure 29) does not show this "blackening" effect because of the reduced water content. This Winter radiances are reduced by more than a factor of two from those of the Summer, due to reduced temperature (and for the long wavelength region, reduced water).

Aerosol content (i. e., visibility) has very little effect on path radiance (see Figures 34 and 35). This can be explained by realizing that

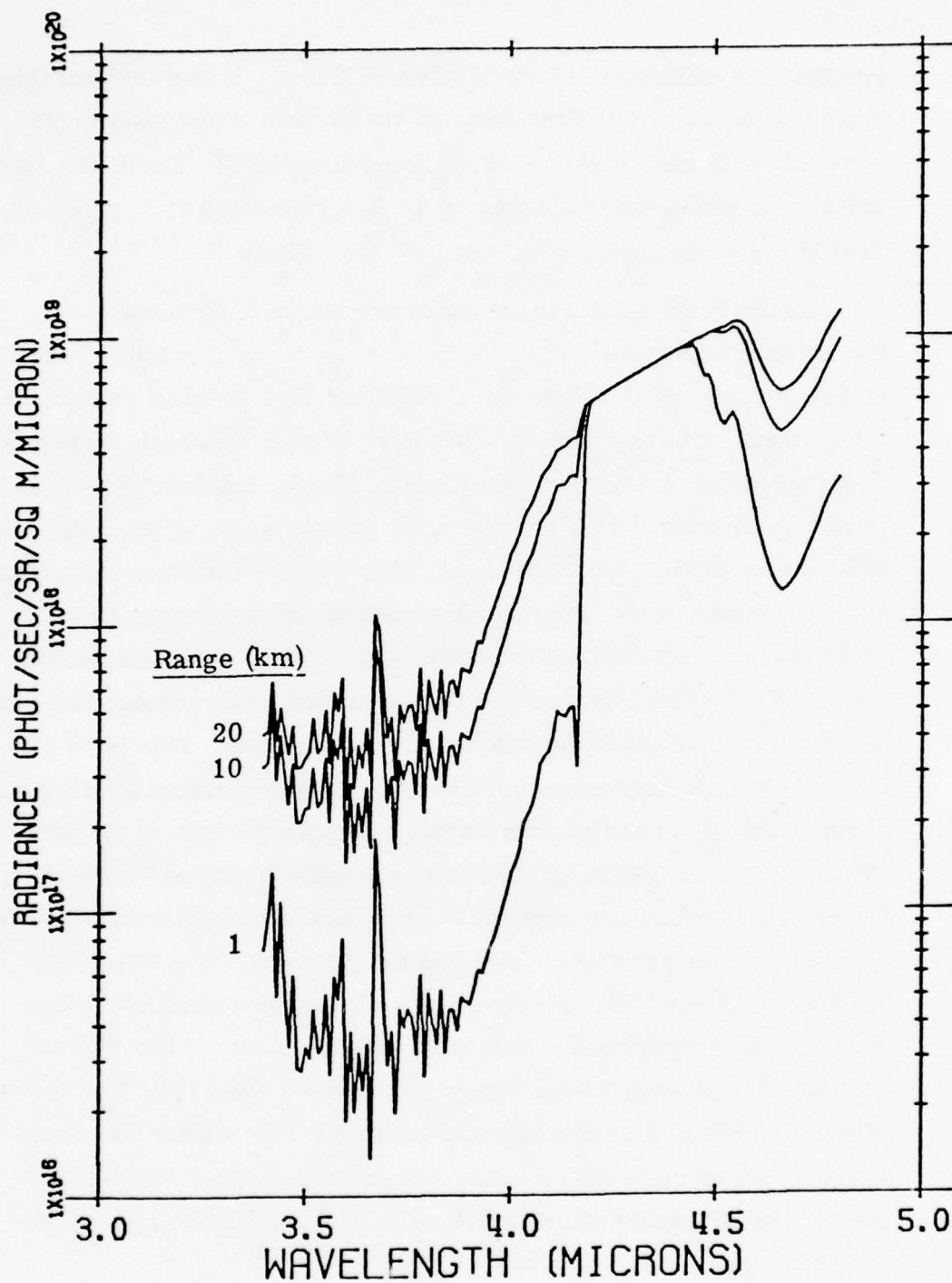


Figure 28. Calculated SWIR Spectral Atmospheric Path Radiance
as a Function of Range;
Midlatitude Winter Model Atmosphere
8.5 km Visibility, 0.75 km Altitude

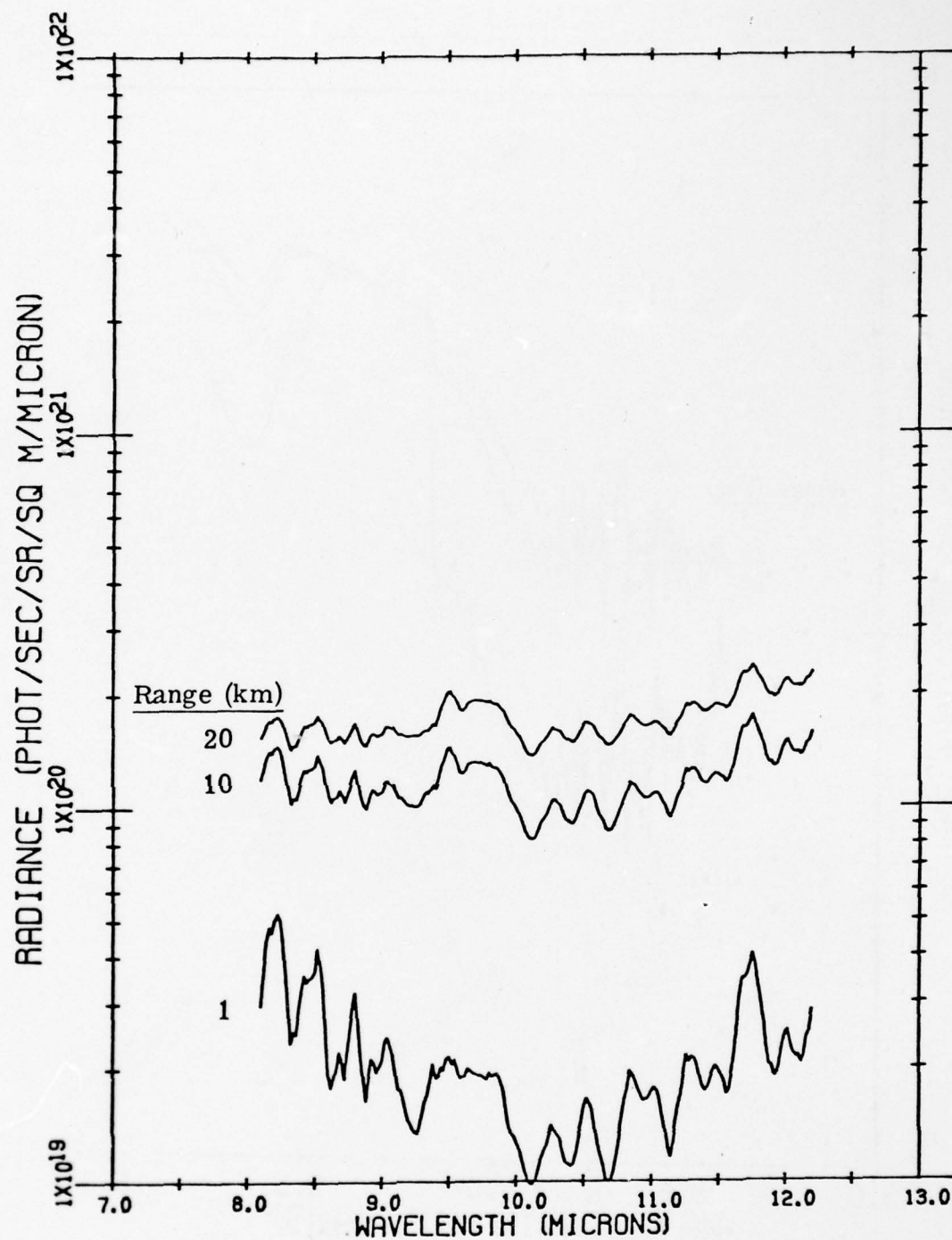


Figure 29. Calculated LWIR Spectral Atmospheric Path Radiance
as a Function of Range:
Midlatitude Winter Model Atmosphere
8.5 km Visibility, 0.75 km Altitude

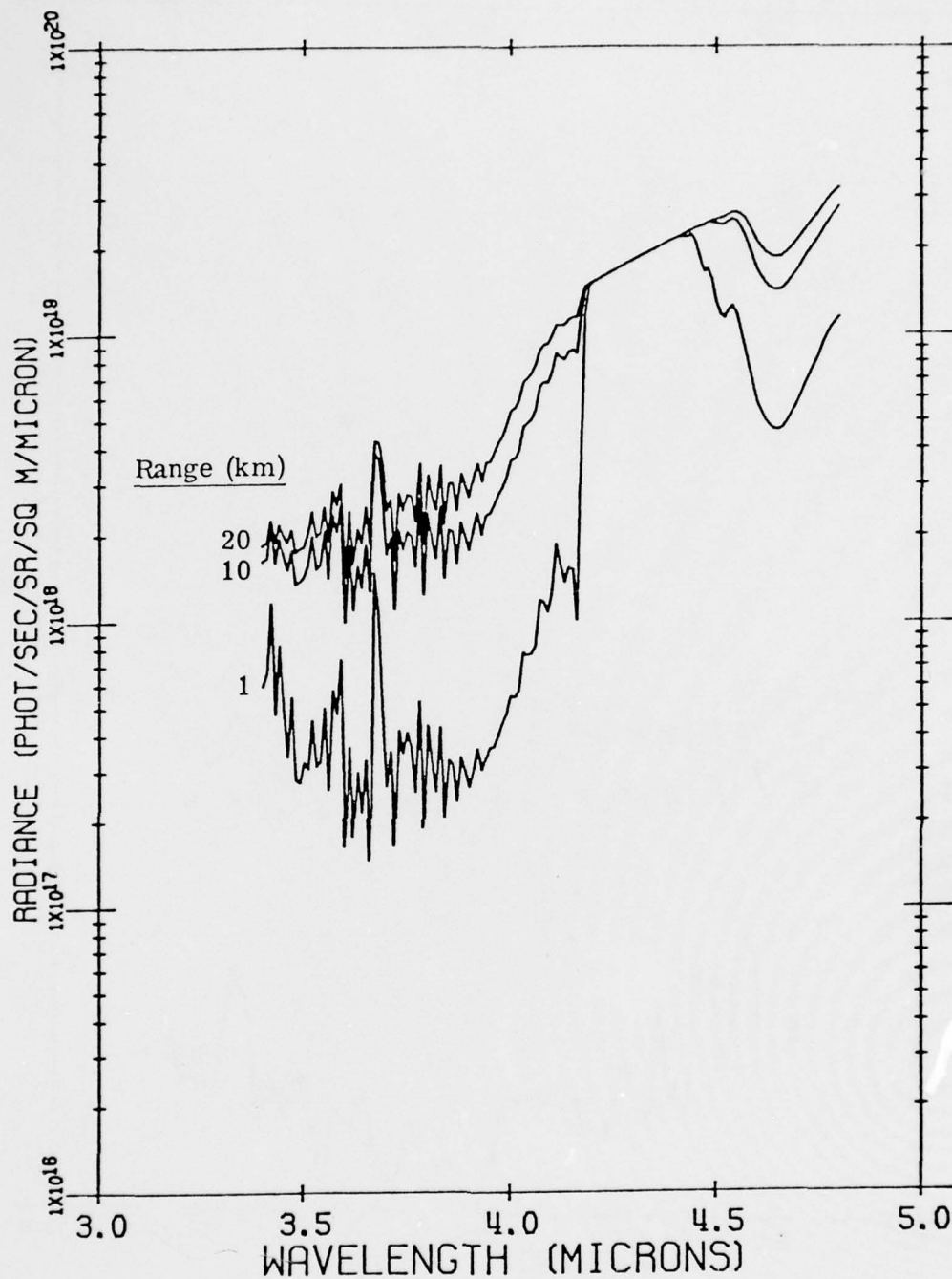


Figure 30. Calculated SWIR Spectral Atmospheric Path Radiance
as a Function of Range;
Midlatitude Summer Model Atmosphere
8.5 km Visibility, 0.75 km Altitude

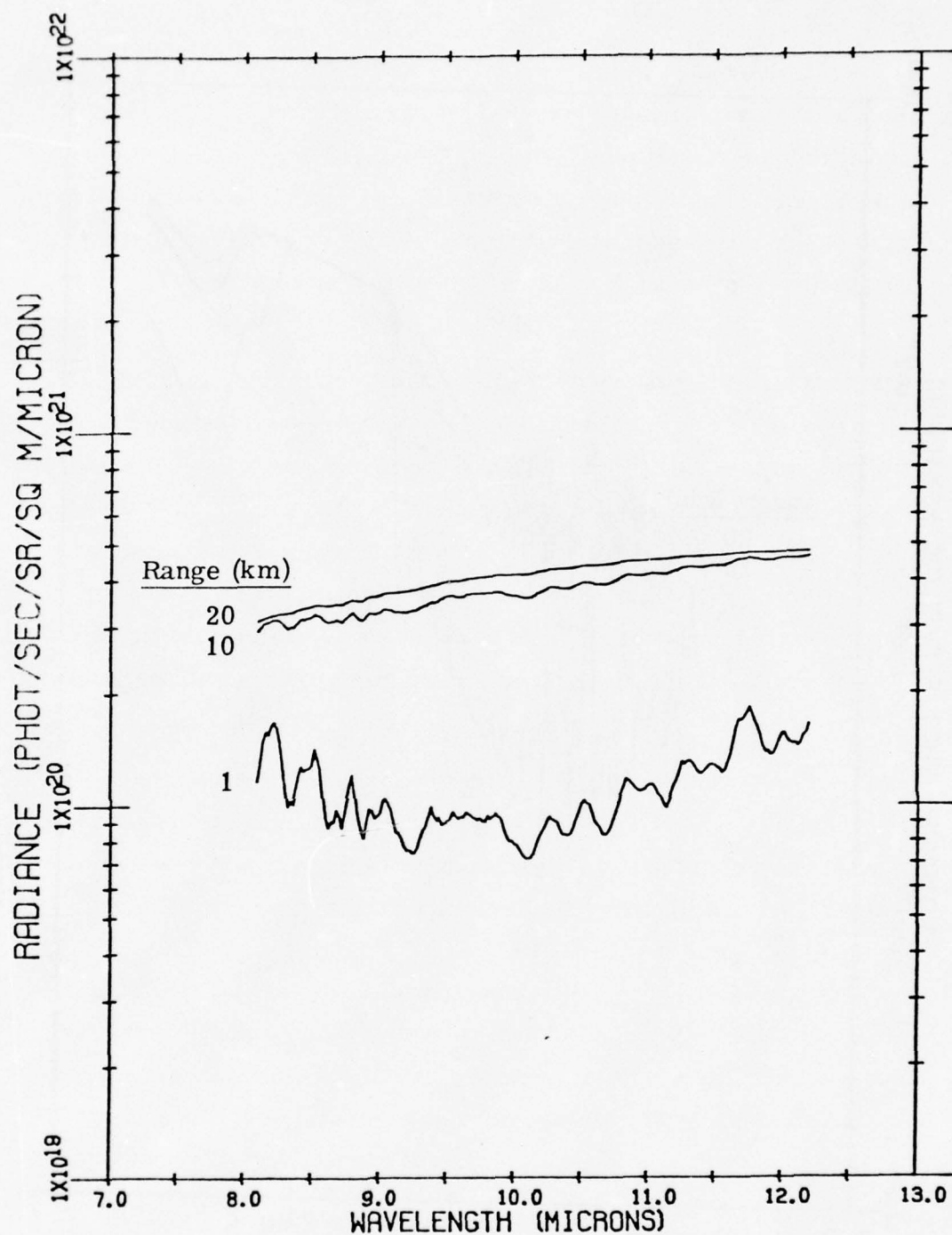


Figure 31. Calculated LWIR Spectral Atmospheric Path Radiance
as a Function of Range;
Midlatitude Summer Model Atmosphere
8.5 km Visibility, 0.75 km Altitude

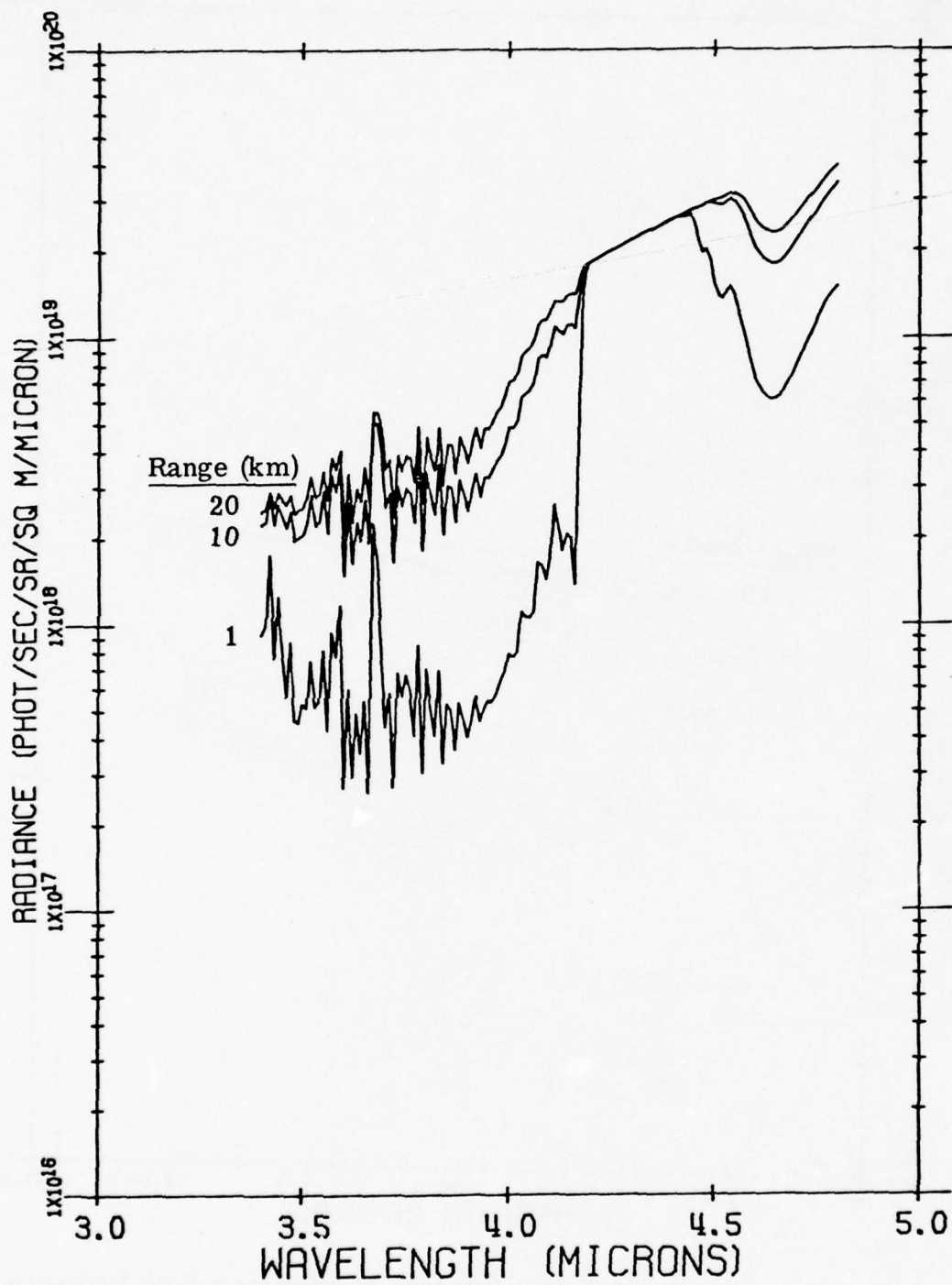


Figure 32. Calculated SWIR Spectral Atmospheric Path Radiance
as a Function of Range;
Tropical Model Atmosphere, 8.5 km Visibility,
0.75 km Altitude

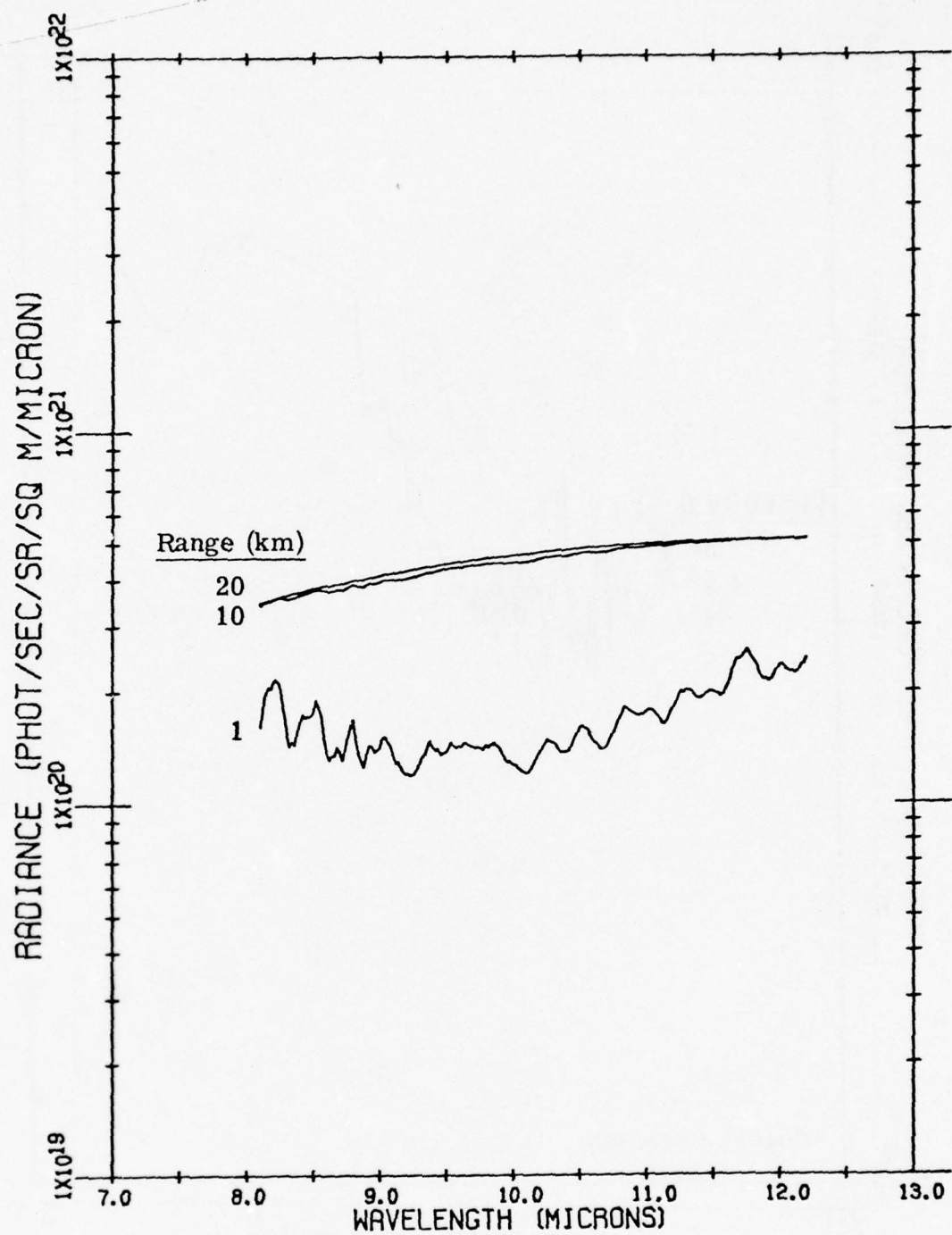


Figure 33. Calculated LWIR Spectral Atmospheric Path Radiance
as a Function of Range;
Tropical Model Atmosphere, 8.5 km Visibility,
0.75 km Altitude

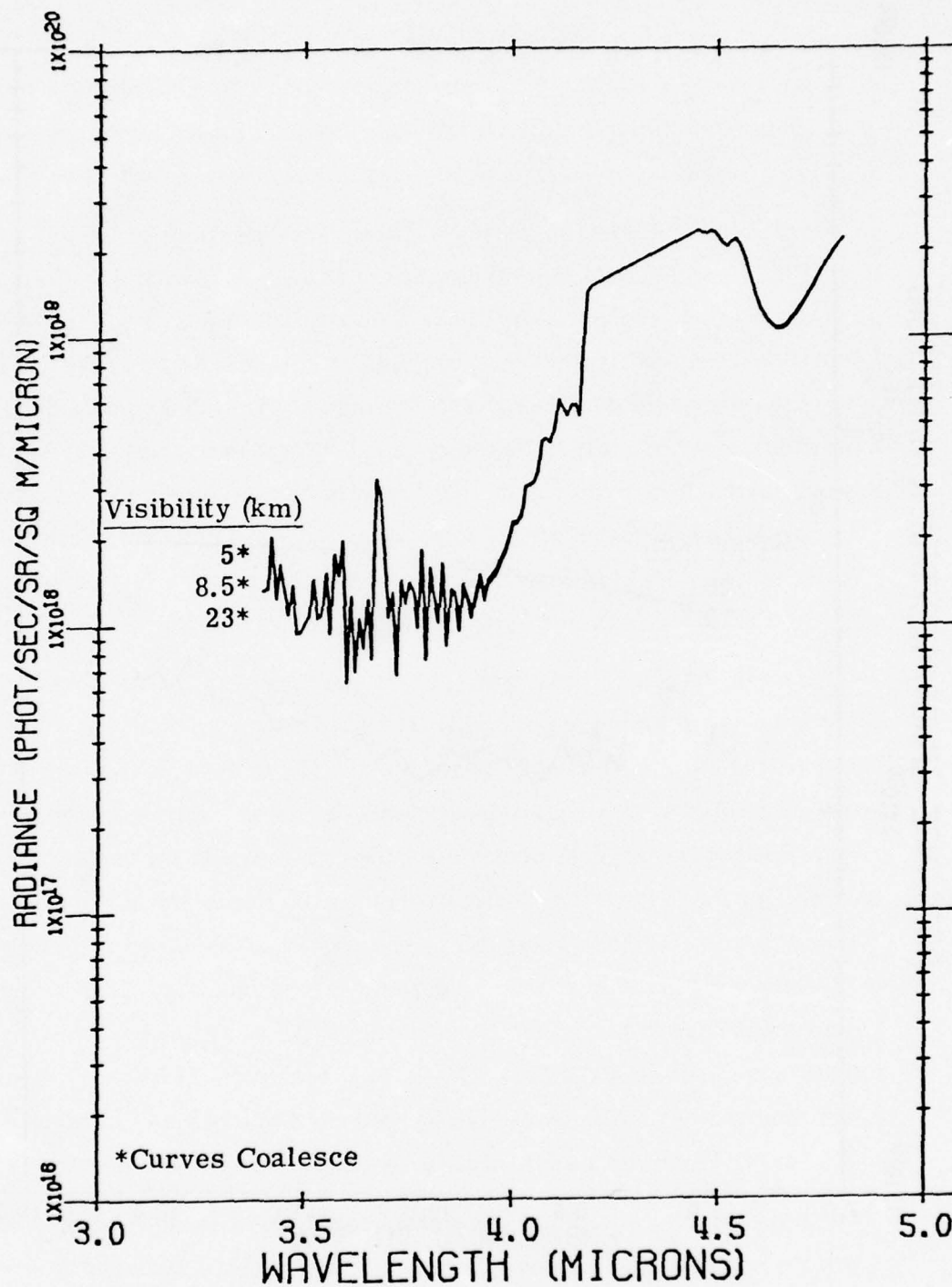


Figure 34. Calculated Spectral Atmospheric Path Radiance
as a Function of Visibility;
Midlatitude Summer Model Atmosphere
5 km Range, 0.75 km Altitude

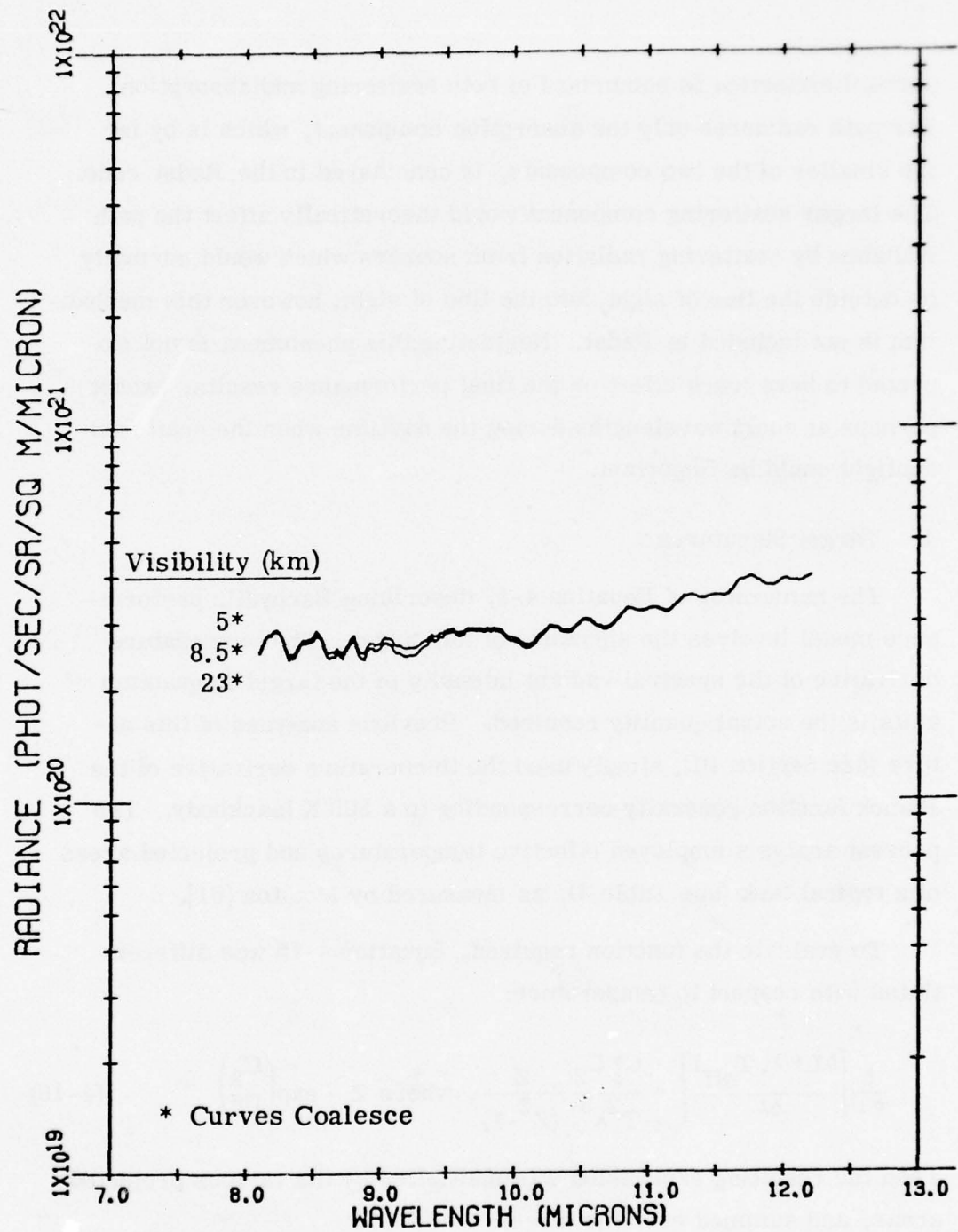


Figure 35. Calculated Spectral Atmospheric Path Radiance
as a Function of Visibility;
Midlatitude Summer Model Atmosphere
5 km Range, 0.75 km Altitude

aerosol extinction is comprised of both scattering and absorption. For path radiances only the absorption component, which is by far the smaller of the two components, is considered in the Radst code. The larger scattering component would theoretically affect the path radiance by scattering radiation from sources which would normally be outside the line of sight, into the line of sight; however this mechanism is not included in Radst. Neglecting this phenomena is not expected to have much effect on the final performance results, except perhaps at short wavelengths during the daytime when the scattered sunlight could be important.

4. Target Signatures

The numerator of Equation 4-1, describing Barhydt's performance model involves the signature of the target. The temperature derivative of the spectral radiant intensity of the target in quantum units is the actual quantity required. Previous analyses of this nature (see Section III), simply used the temperature derivative of the Planck function generally corresponding to a 300 K blackbody. The present analysis employed effective temperatures and projected areas of a typical tank (see Table 3), as measured by Moulton [61].

To evaluate the function required, Equation 4-15 was differentiated with respect to temperature:

$$\frac{\partial}{\partial T} \left[\frac{\partial L^*(\lambda, T_{\text{eff}})}{\partial \lambda} \right] = \frac{C_1^* C_2}{T^2 \lambda^5} \frac{Z}{(Z^2 - 1)}, \text{ where } Z \equiv \exp\left(\frac{C_2}{\lambda T}\right) \quad (4-16)$$

Then the resulting expression was multiplied by the various projected areas, and summed over the target:

$$\frac{\partial J_t^*}{\partial T \partial \lambda} = \sum_{i=1}^m (A_p)_i \frac{\partial^2 L^*(\lambda, T_i)}{\partial T \partial \lambda} \quad (4-17)$$

Table 3.
Measured Effective Temperatures and
Projected Areas of an Operating Tank [61]

Aspect	Component	Projected Area (m ²)	Effective Temperature Above Ambient (K)
Side	Turret	3.4	0.66
	Tread	8.4	5.40
Front	Turret	3.9	0.92
	Hull	1.9	1.90
	Tread	1.8	5.70
Rear	Turret	2.6	0.91
	Hull	1.8	2.20
	Tread	1.8	5.50
	Engine	1.4	49.0

This radiant intensity function was calculated for three different aspects of the tank in the two spectral regions of interest. It was tacitly assumed that the emittance of the target is the same in the two atmospheric windows.

Results of these calculations for front, side and rear aspects are shown in Figure 36. In addition to these calculations using the measured temperatures, calculations were performed for a range of assumed temperatures for the same projected areas (actually the projected area is not important since it can be canceled out of the relative performance expression (i. e., it is independent of wavelength). These results are shown in Figure 37.

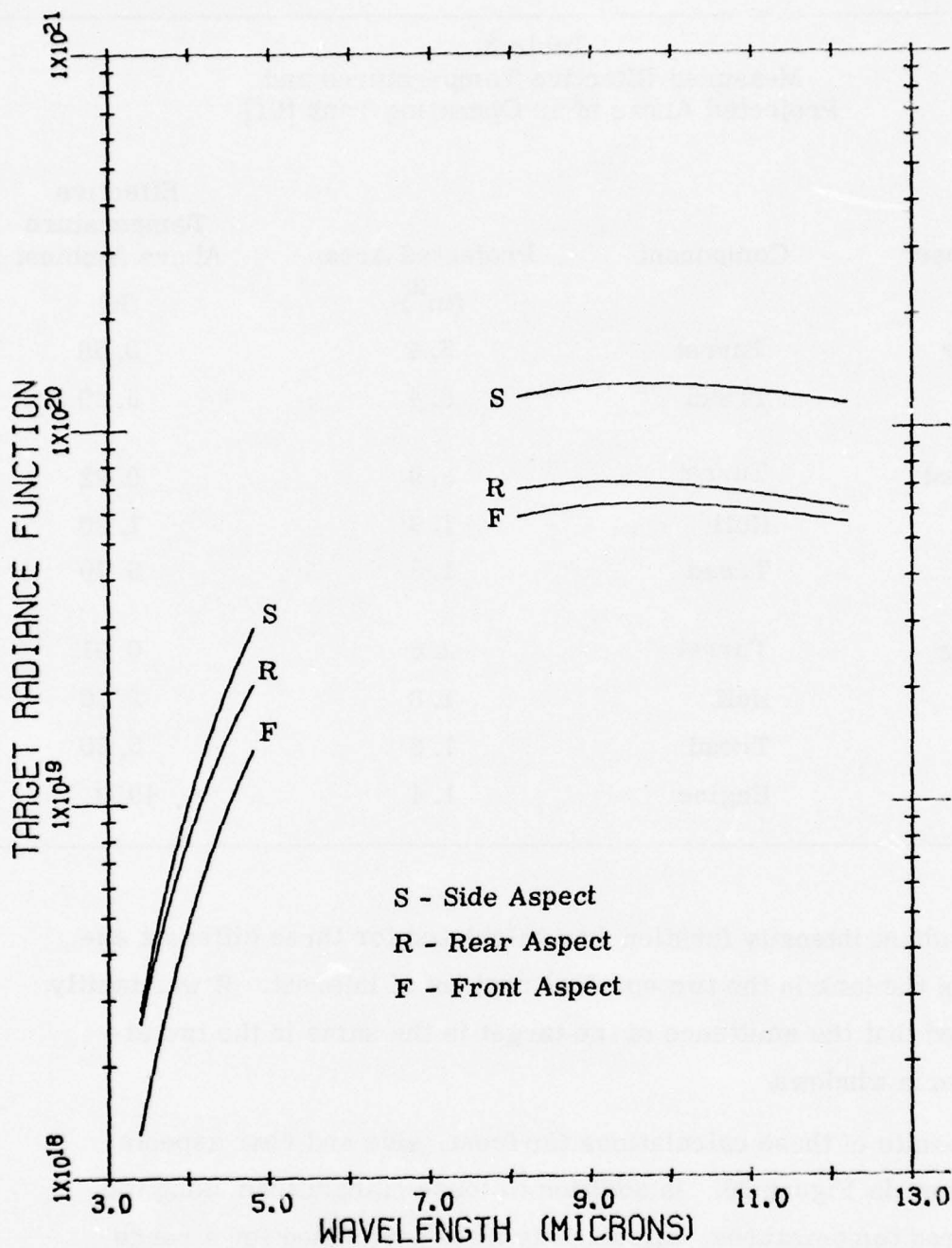


Figure 36. Target Spectral Radiation Function (phot/sec/sr/ μ m/K) for Tank at Various Aspects Based on Measurements by Moulton [61].

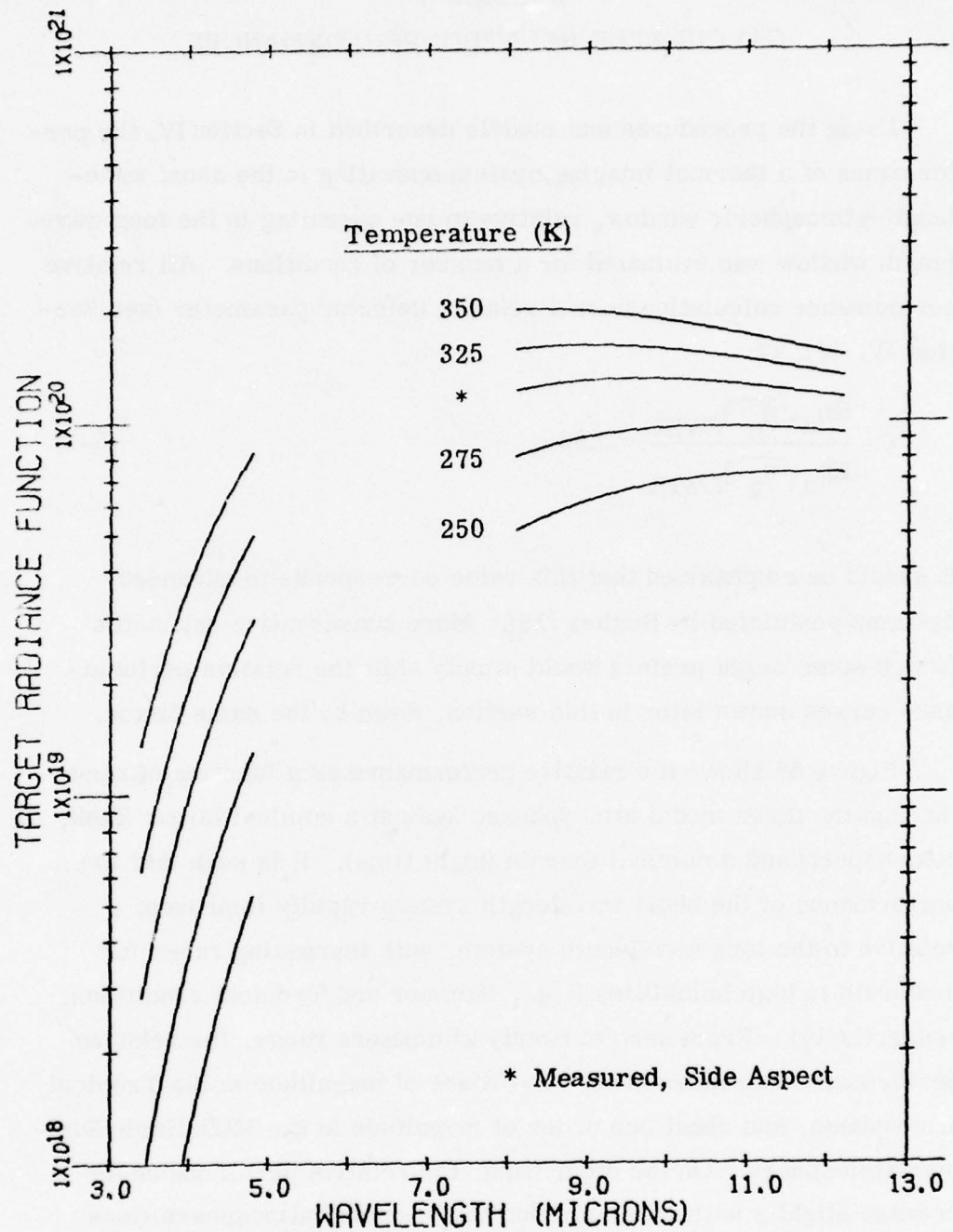


Figure 37. Calculated Target Spectral Radiation Function (phot/sec/sr/ μ m/K) for Various Target Temperatures

SECTION V

CALCULATED RELATIVE PERFORMANCES

Using the procedures and models described in Section IV, the performance of a thermal imaging system operating in the short wavelength atmospheric window, relative to one operating in the long wavelength window was evaluated for a number of conditions. All relative performance calculations use a relative detector parameter (see Section IV, #1), of:

$$\xi = \frac{K\eta_d \sqrt{\eta_q})_{\text{SWIR}}}{K\eta_d \sqrt{\eta_q})_{\text{LWIR}}} = 2.83 \quad (5-1)$$

It should be emphasized that this value corresponds to advanced systems postulated by Hughes [19]. More conservative estimates (which some might prefer) would simply shift the relative performance curves shown later in this section, down by the same factor.

Figure 38 shows the relative performance as a function of range through the three model atmospheres against a nominal target (tank, rear aspect) and a nominal terrain (night time). It is seen that the performance of the short wavelength system rapidly improves, relative to the long wavelength system, with increasing range for moderate to high humidities (i. e. , Summer and Tropical conditions, respectively). From zero to twenty kilometers range, the relative performance increases about two orders of magnitude in the Tropical atmosphere, and about one order of magnitude in the Midlatitude Summer atmosphere. On the other hand, the relative performance decreases slightly with range for the Winter model atmosphere (less than 50% from zero to twenty kilometers range). Cooler targets (or other than rear aspect) would reduce the relative performance as will be shown later.

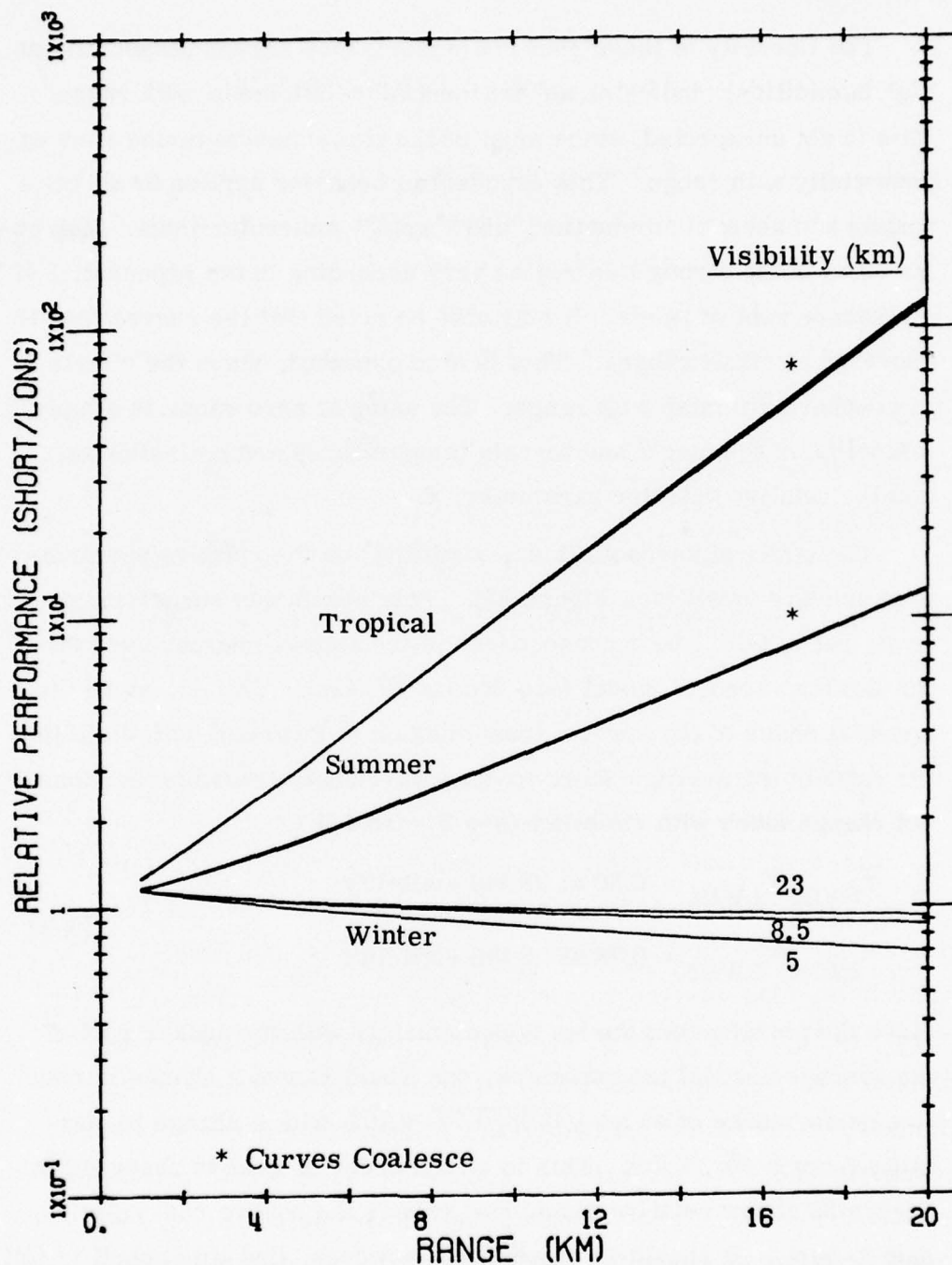


Figure 38. Calculated Performance of a 3.4 - 4.8 μm FLIR Relative to an 8.1 - 12.2 μm FLIR as a Function of Atmospheric and Aerosol Models; 0.75 km Altitude, Nominal Target and Terrain

The linearity of these relative performance curves (especially at high humidities), indicates an exponential relationship with range. This is not unexpected, since most of the transmission terms vary exponentially with range. This exponential behavior applies to all continuum and aerosol attenuation, and "weak" molecular lines. Molecular lines in the strong line region vary according to the exponential of the square root of range. It may also be noted that the curves tend to converge at small ranges. This is also expected, since the effects of atmosphere diminish with range. The value at zero range is simply a function of the target and terrain temperatures and emissivities, and the relative detector parameter, ξ .

The effect of aerosols (i. e. , visibility) on the relative performance is quite small (see Figure 38). This result was surprising at first, but is felt to be a consequence of the approximations used in the Lowtran aerosol model (see Section IV, #2). That is, since the spectral shape of the aerosol transmission is invariant with visibility, the ratio of the average short-to-long wavelength transmission does not change much with visibility (see Figure 12):

$$\begin{aligned}\bar{\tau}_{\text{SWIR}}/\bar{\tau}_{\text{LWIR}} &= 0.96 \text{ at } 23 \text{ km visibility} \\ \bar{\tau}_{\text{SWIR}}/\bar{\tau}_{\text{LWIR}} &= 0.78 \text{ at } 5 \text{ km visibility}\end{aligned}\tag{5-2}$$

Since the performance varies approximately with the square root of the average aerosol transmission, one would expect a change in relative performance of about $\sqrt{0.96/0.78} \approx 10\%$ with a change in visibility from 5 to 23 km. This is on the order of what is observed in Figure 38 at low relative humidities (where the square root relationship is best). It should be emphasized however, that this result is felt to be fictitious, and the result of an unrealistic aerosol model in Lowtran.

The level of the water vapor continuum absorption in the two atmospheric window regions is still uncertain (see Section IV, #2b). Although the effect of this uncertainty appears quite small in atmospheric transmission, (see Figures 21 and 22) its influence on the relative performance is rather large (see Figure 39). Combinations of various continua were selected to give the maximum variations (i. e., the smallest in one band with the largest in the other band, and vice versa). By this pairing, with the Tropical atmosphere there is more than a factor of five difference between the maximum and minimum relative performance at twenty kilometers range. It is unlikely that the calculations would be off by this much, but these results are presented to show a worst case. Note that the nominal model used in this study does not correspond to any of those indicated in Figure 39, but is near Curve A. Its closeness to Curve A can be explained by the fact that the long wavelength continuum is more important than the short, and that the Lowtran III model (which is used as nominal) is so highly absorbing (see Figure 22).

Platform altitude generally influences the relative performance more than visibility (see Figure 40). At higher humidities (i. e., Tropical and Summer models), the short wavelength system tends to become favored at lower altitudes because of the increased water vapor in the path. However for summer conditions, the improvement is less than a factor of two at twenty kilometers range for a decrease in altitude from 1 to 0.5 km. An even smaller change is indicated for winter conditions, where the effect is insignificant. This is due to the reduced water content of the atmosphere during the winter. It is interesting (but still not significant), that the relative performance improves slightly with altitude during the winter.

Figure 41 (solid curves) shows the effect of target aspect on relative performance for nominal atmospheric, viewing and terrain conditions. The aspect effect is quite small for this target (less than a

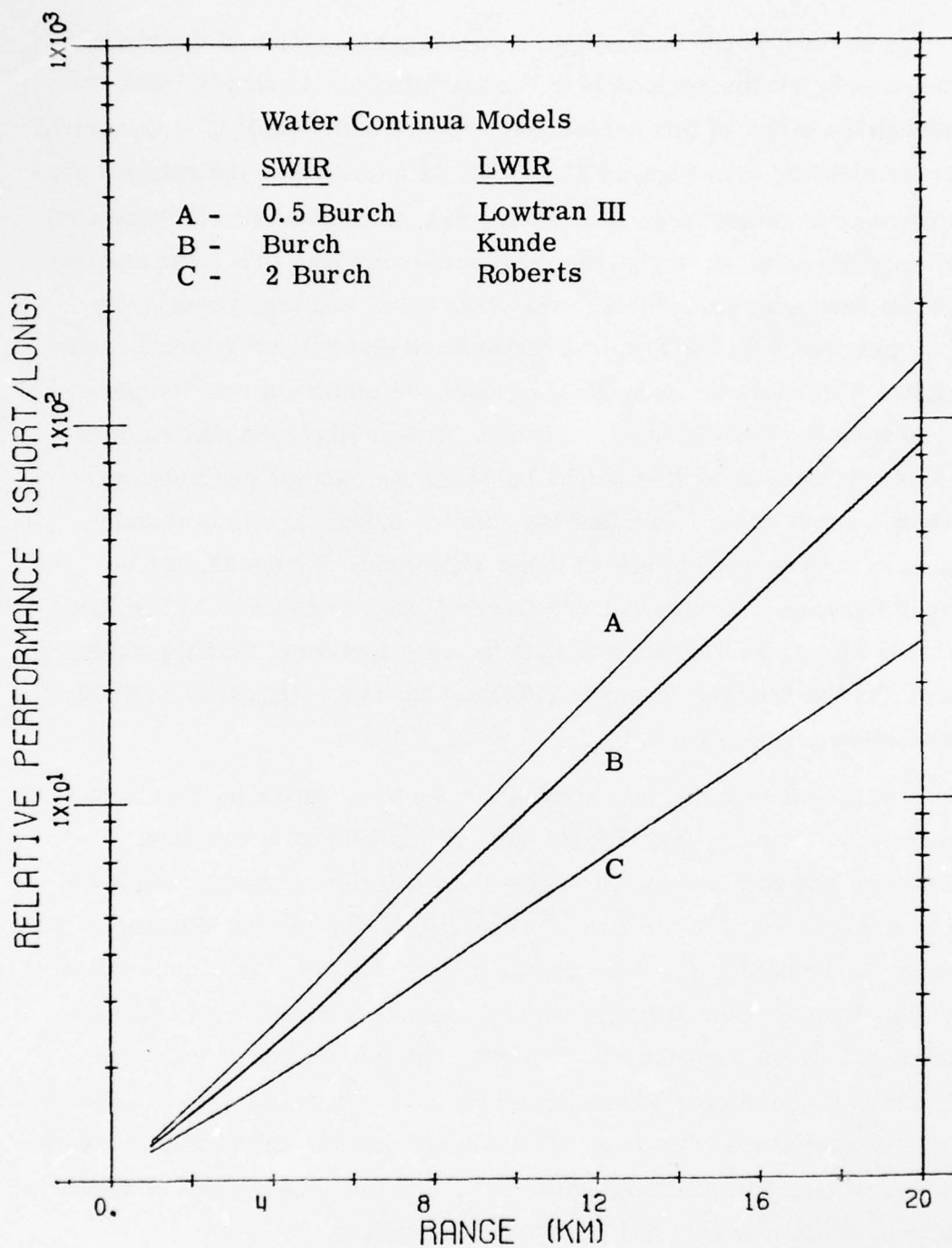


Figure 39. Calculated Performance of a 3.4 - 4.8 μ m FLIR
Relative to an 8.1 - 12.2 μ m FLIR for Various
Water Continuum Model Combinations;
Tropical Atmosphere, Other Conditions Nominal

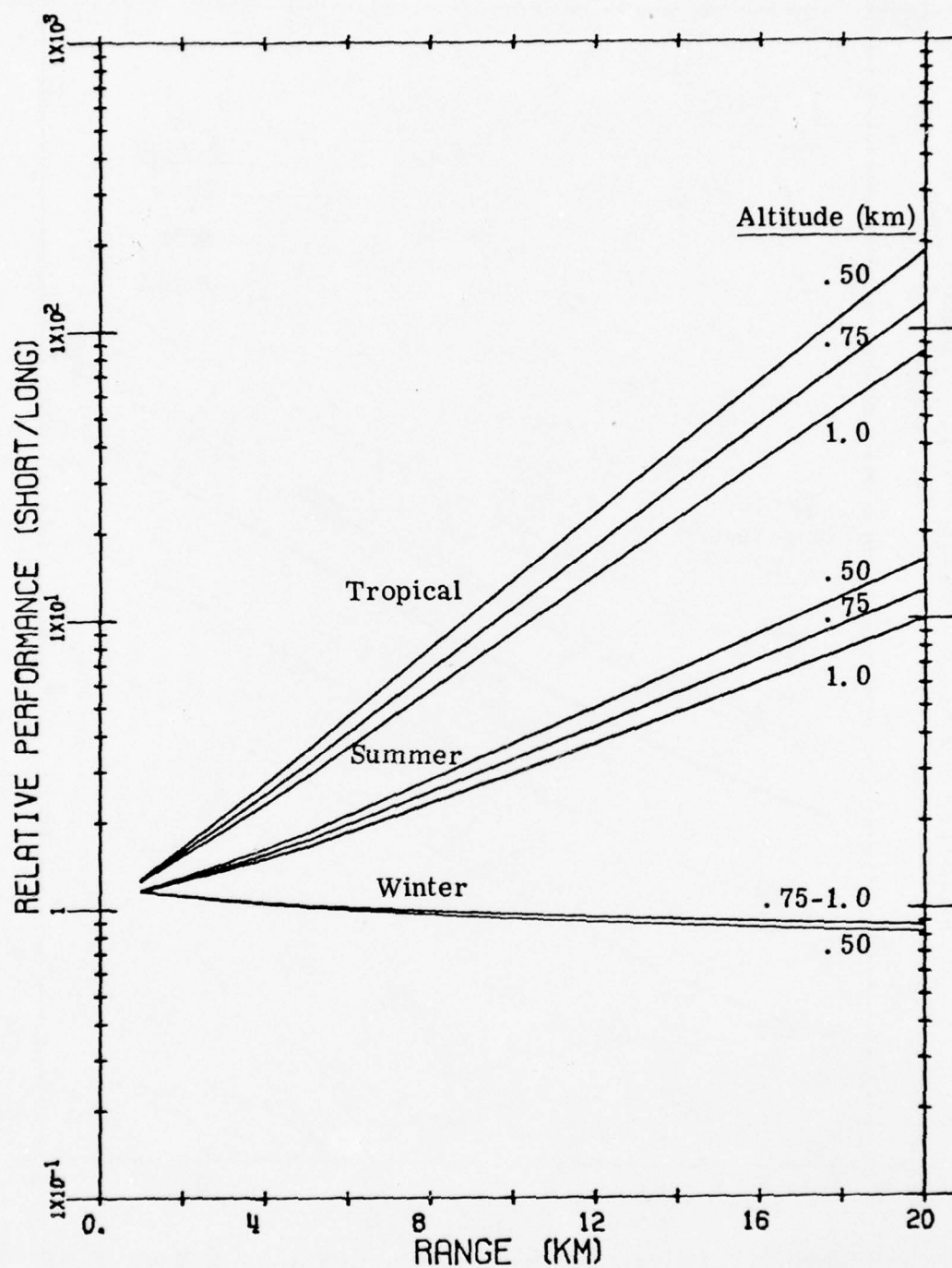


Figure 40. Calculated Performance of a 3.4 - 4.8 μm FLIR Relative to an 8.1 - 12.2 μm FLIR as a Function of Platform Altitude; 8.5 km Visibility, Nominal Target and Terrain

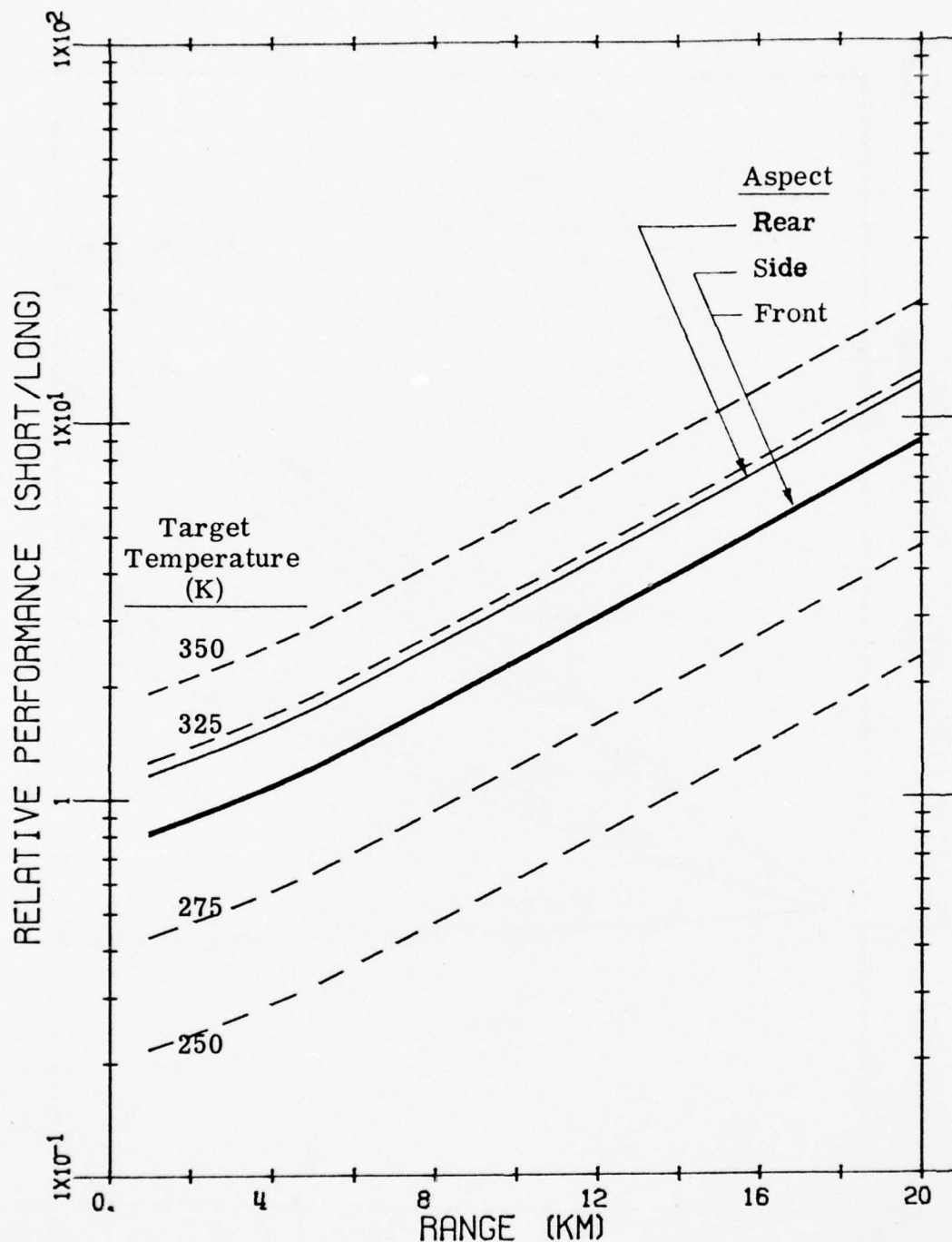


Figure 41. Calculated Performance of a 3.4 - 4.8 μm FLIR Relative to an 8.1 - 12.2 μm FLIR as a Function of the Target Midlatitude Summer, 0.75 km Altitude, 8.5 km Visibility

factor of two), and approximately independent of range out to twenty kilometers. Arbitrarily varying the target temperature over large extremes (see Figure 41, dashed curves), does result in significant performance variations; the short wavelength system favoring high temperature targets and the long favoring low temperatures, as expected. The zero range performance varies with target temperature according to theory (see Appendix C).

The effect of terrain temperature is much smaller than that of target temperature (see Figure 42). This is due to the square root dependence on terrain radiance, and the combination of this term with path radiance (see Eqn. 4-10). Note also the reduction of the influence of the terrain with increasing range. This is because the path radiance term grows with range, and starts to dominate the terrain term. Measured terrain radiances indicate larger effects from day to night than might be expected from their effective temperatures, but are still relatively insignificant.

As mentioned earlier (see Section 4.3), most other analyses approximated the term $\tau_a L_g^* + L_p^*$, by L_g^* alone. This approximation is seen to favor slightly the short wavelength system for humid conditions and the long wavelength systems for dry conditions (see Figure 43). The effect is quite small (i. e. , 10-20%), and appears independent of range. On the other hand, neglecting L_p^* , but including the τ_a factor, results in an approximation which for humid conditions, tends to favor the long wavelength system more and more as range increases. For dry conditions, it favors the short wavelength system slightly, and again apparently independent of range.

A cursory examination was also made of the influence of the limits of the spectral bandpass on the performance of the systems. Four smaller bandpasses from within the nominal short wavelength window were selected for investigation: 3.4 - 4.0 μm , 3.45 - 3.5 μm , 4.5 -

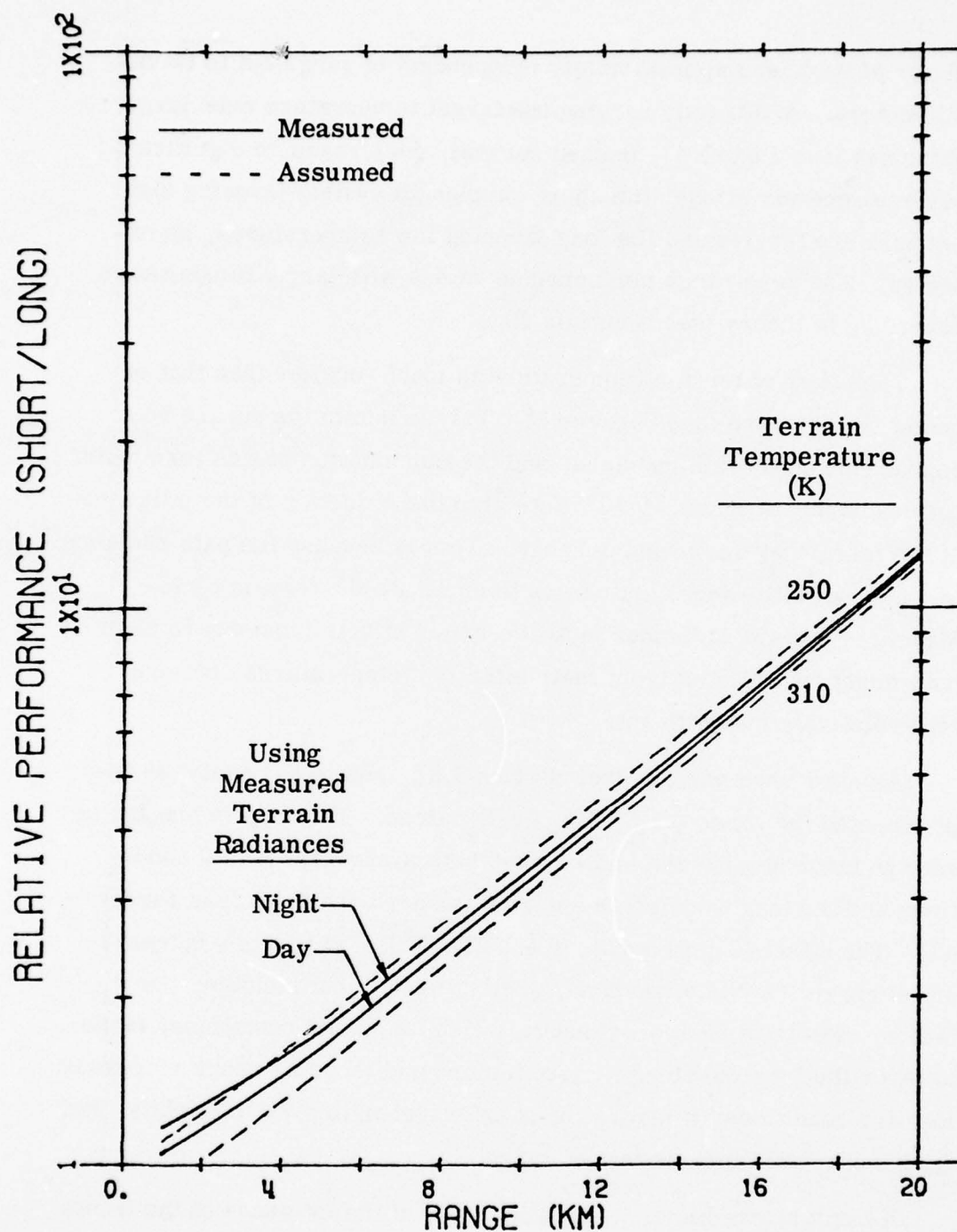


Figure 42. Calculated Performance of a 3.4 - 4.8 μm FLIR Relative to an 8.1 - 12.2 μm FLIR as a Function of the Terrain; Midlatitude Summer, 0.75 km Altitude, 8.5 km Visibility, Nominal Target

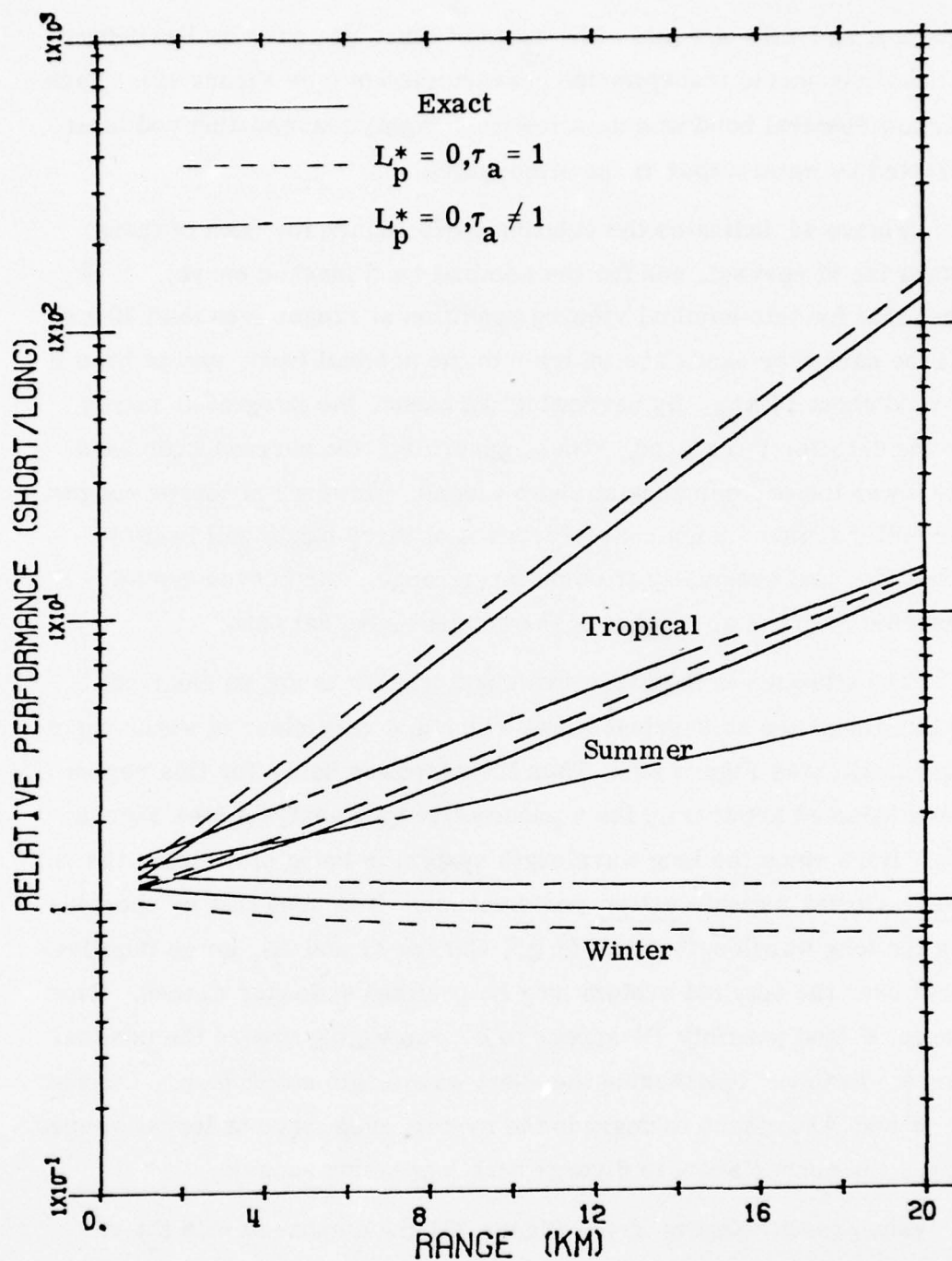


Figure 43. Calculated Performance of a 3.4 - 4.8 μm FLIR Relative to an 8.1 - 12.2 μm FLIR for Various Performance Model Treatments of the Background

4.65 μm and 4.6 - 4.8 μm . The basis of these regions was the calculated atmospheric transmission characteristics (see Figure 19). Each narrow spectral band was selected to be highly transmitting and least affected by water vapor in the atmosphere.

Figure 44 indicates the relative performance for each of these bands (solid curves), and for the nominal band (dashed curve). It is seen that for this nominal viewing condition at ranges less than 20 km, all the narrower bands are inferior to the nominal band, except band A beyond about 14 km. By narrowing the bands, the integrated energy on the detector is reduced. Thus, generally* the narrower the band the lower the performance at short ranges. However at longer ranges, the better transmission characteristics of these bands will begin to dominate, and eventually at some large range their curves are all expected to cross above that of the nominal spectral band.

The situation in the long wavelength window is not so clear-cut, in that there are no spectral bands which are very clear of water vapor attenuation (see Figure 20). Thus the narrower bands for this region were selected arbitrarily for a parametric type analysis (see Figure 45). Here since the long wavelength system is being optimized, the lower curves indicate better performance. It is seen that by shortening the long wavelength cutoff (e. g. , Curves G and H), some improvement over the nominal system may be realized at longer ranges. Even Curve E (and possibly D) appear to be converging toward the nominal curve. However lengthening the short wavelength cutoff (e. g. , Curves F, B and A) appears to degrade the system even more at longer ranges (i. e. , the curves seem to diverge with increasing range).

The present results (from Figure 38) are compared with the results of previous analyses in Figures 46 and 47. It should be remembered that the present results are for slant paths from 0.75 km altitude,

* The exception (i. e. , Curve B crossing Curve A) is due to the shape of the Planckian function.

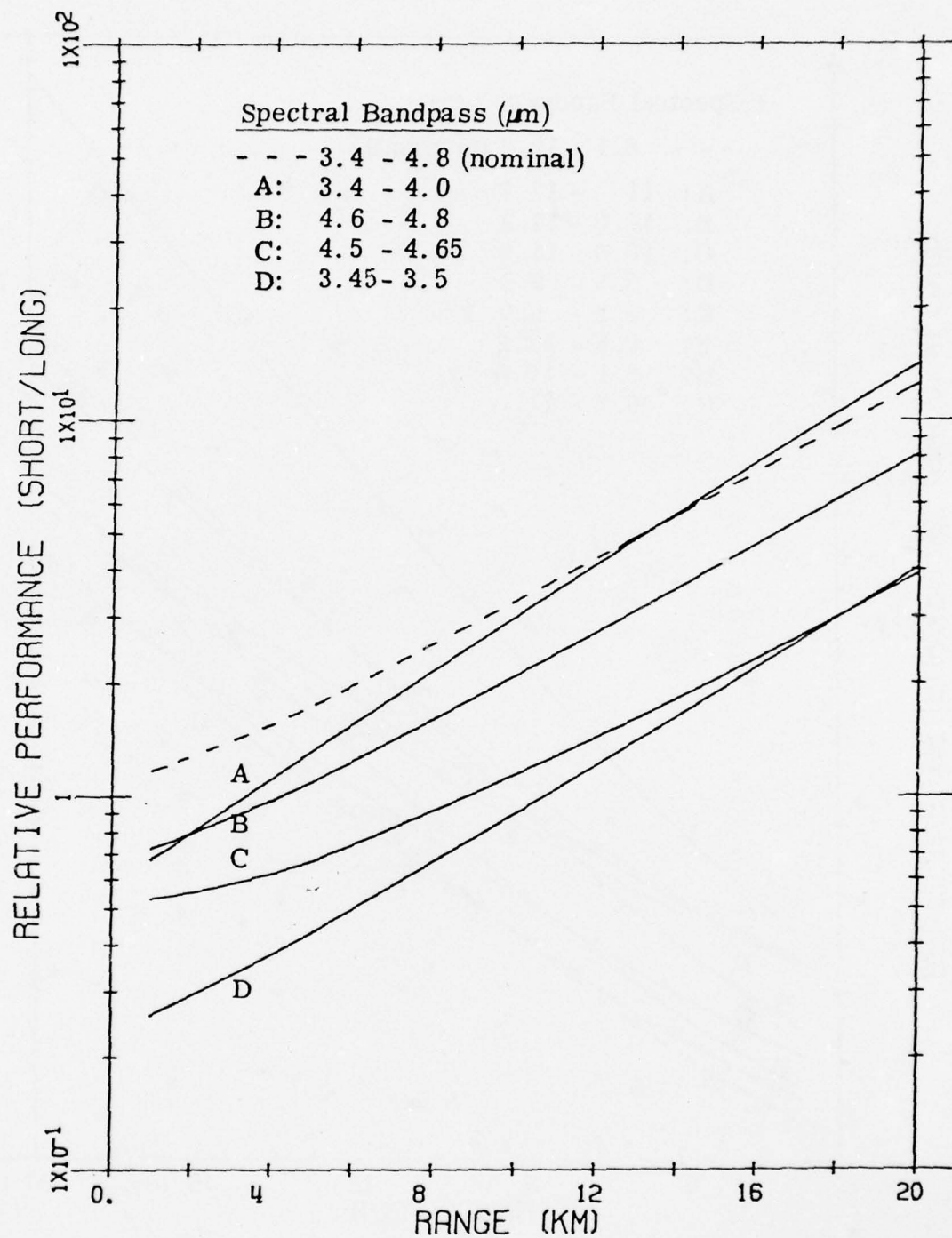


Figure 44. Calculated Performance of a 3.4 - 4.8 μm FLIR
Relative to Several Long Wavelength FLIRs;
Midlatitude Summer Atmosphere, 8.5 km Visibility,
0.75 km Altitude, Nominal Target and Terrain

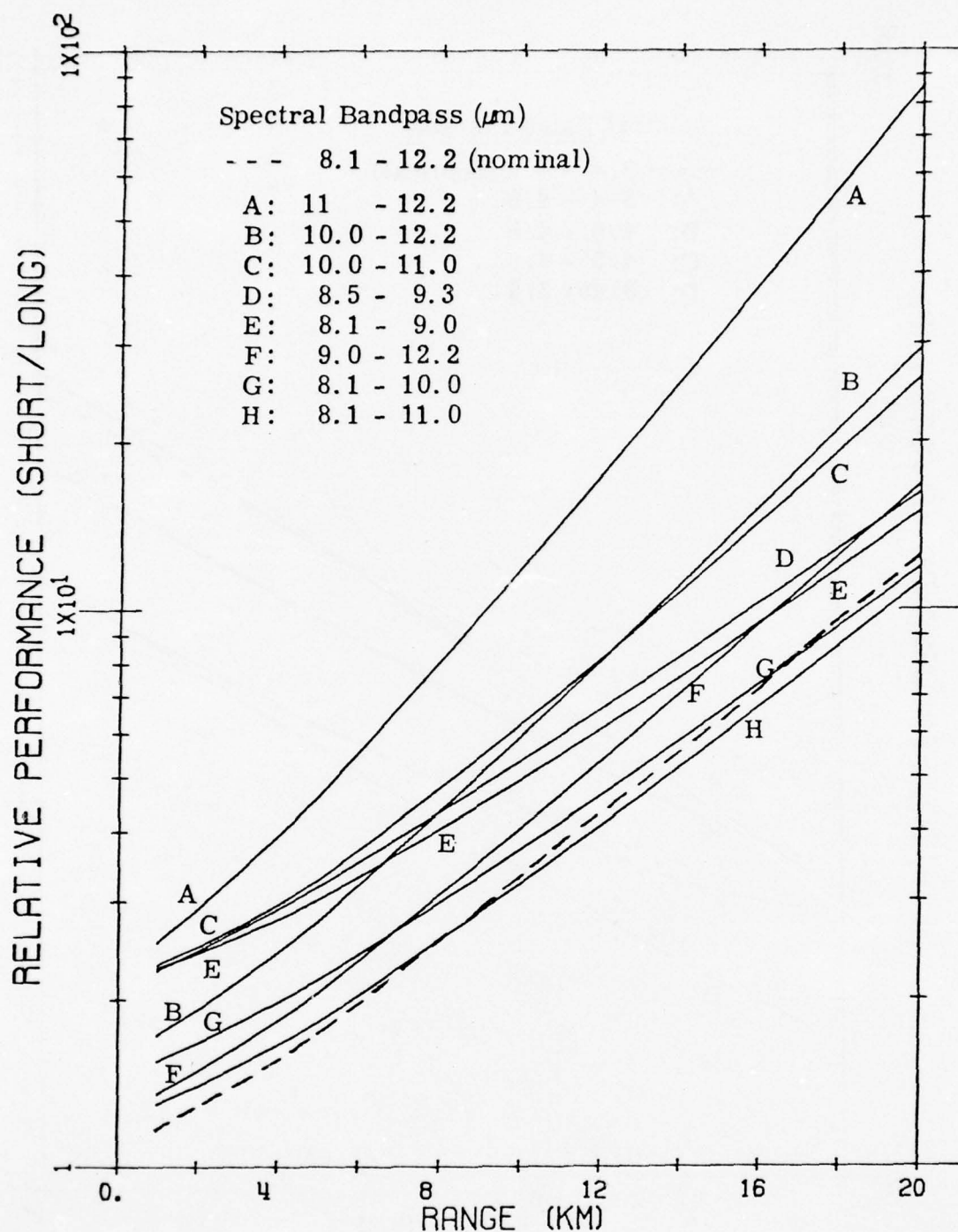


Figure 45. Calculated Performance of Several Short Wavelength FLIRs Relative to an 8.1 - 12.2 μm FLIR; Midlatitude Summer Atmosphere, 8.5 km Visibility, 0.75 km Altitude, Nominal Target and Terrain

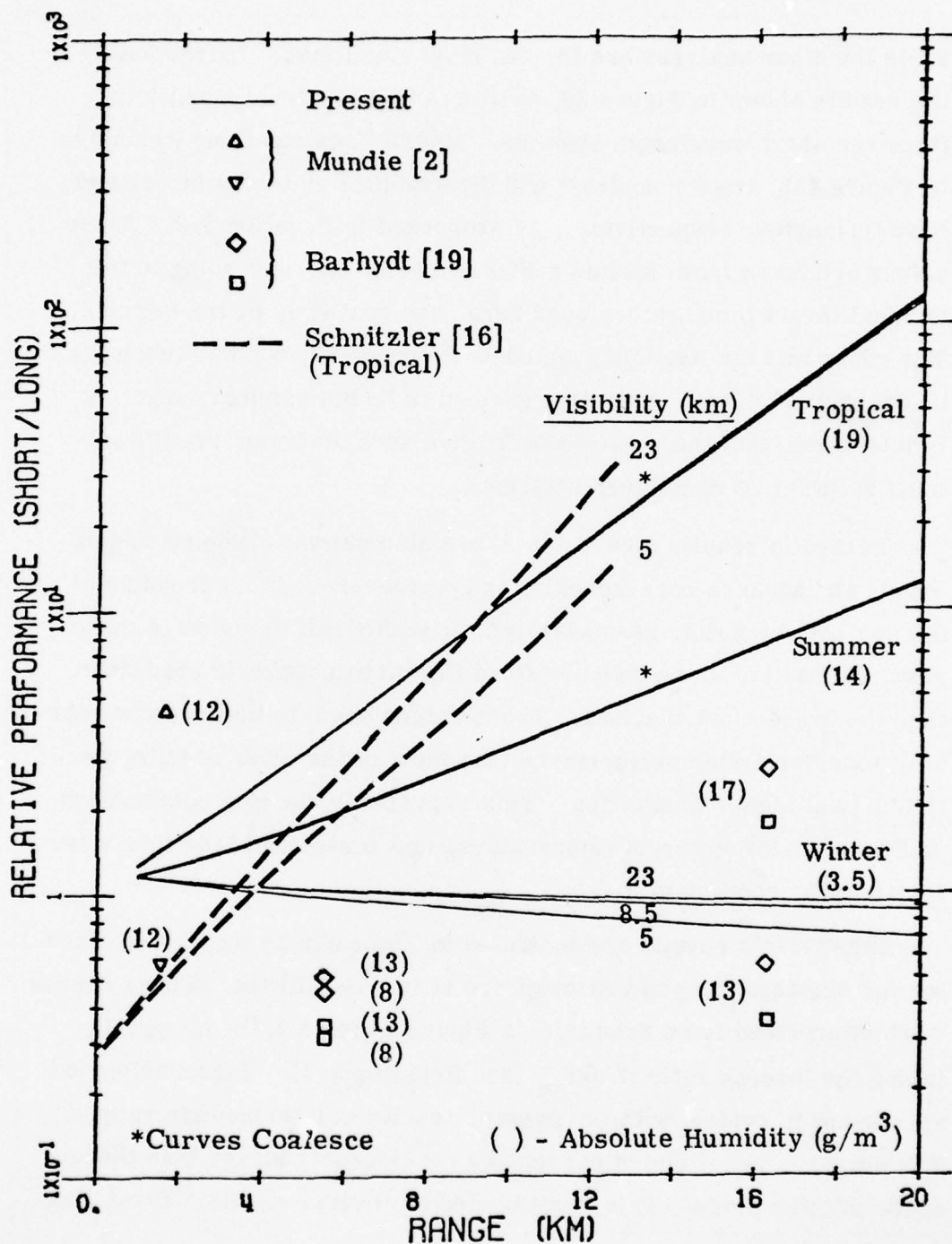


Figure 46. Comparison of Calculated Relative Performance with those of Mundie, Barhydt and Schnitzler

while the other analyses are for sea level conditions. Extrapolating the results shown in Figure 39, indicates that sea level conditions favor the short wavelength systems. Mundie's calculations (triangles in Figure 46), are for contrast and detectability criterion (upper and lower triangles, respectively), as expressed in Equation 3-2. These values are taken from Mundie's Figure 12 [2], corresponding to the nominal target temperature used here, and scaled up by the factor ξ . The range was not explicitly stated in Reference 2, but was taken to be one mile (1.6 km), since that seemed to be his nominal range. It is interesting that these two criteria give such divergent results (almost an order of magnitude different).

Barhydt's results (see Table 2) are also shown in Figure 46 (diamonds and squares corresponding to aperture-resolution products of 0.8 and 1.25 in-mrad, respectively). It is difficult to compare these results directly, since they are for different atmospheric conditions than the present calculations. These values seem to indicate considerably poorer relative performance than most of the other results, particularly at higher humidities. This is probably due to a combination of Barhydt's lower target temperature, and omission of the long wavelength water continuum.*

Schnitzler's results are indicated in Figure 46 by the dashed lines for the standard Tropical Atmosphere at two visibilities. These curves were interpreted from Schnitzler's Figure 10 for a 3.1m target, by taking the inverse ratio of ΔT_{in} (see Equation 3-4). Reasonably good agreement is evident with the present results at intermediate ranges. The slopes of Schnitzler's curves are considerably larger than those of the present study. This is attributed to several effects. First, his

* Yates and Taylor's measurements (employed by Barhydt and Mundie) were reduced in such a way to omit the long wavelength water continuum [17, 27].

calculations are for the higher effective humidity at sea level as compared to the slant path considered in the present study. Second, the Lowtran II model he used neglects the $4\text{ }\mu\text{m}$ water continuum, while the present results include it. Finally, his results are for a slightly different short wavelength bandpass ($3.33 - 4.17\text{ }\mu\text{m}$ instead of $3.4 - 4.8\text{ }\mu\text{m}$), which tends to give a larger slope (see Figure 44). The zero range results are somewhat lower than any of the other results, probably due to different assumed systems parameters, and a lower target temperature.

Milton's results (see Figure 47) also indicate a slightly steeper slope (at the high humidity condition) than the present results, but not as steep as Schnitzler's. The reasons are probably the same as the first two given above for Schnitzler. Otherwise the agreement between Milton's results and the present results is very good at the high humidity conditions. At low humidities Milton's results are somewhat below the present results, but indicate the same general trend. The effect of aerosols (i. e. , visibility) is much stronger in both Schnitzler's and Milton's results, than in the present results. The reason for this is unclear, but may be due to differences in the way atmospheric transmission is applied in the models (see Equations 4-10 and 4-11), or differences between the Lowtran II and III aerosol models.

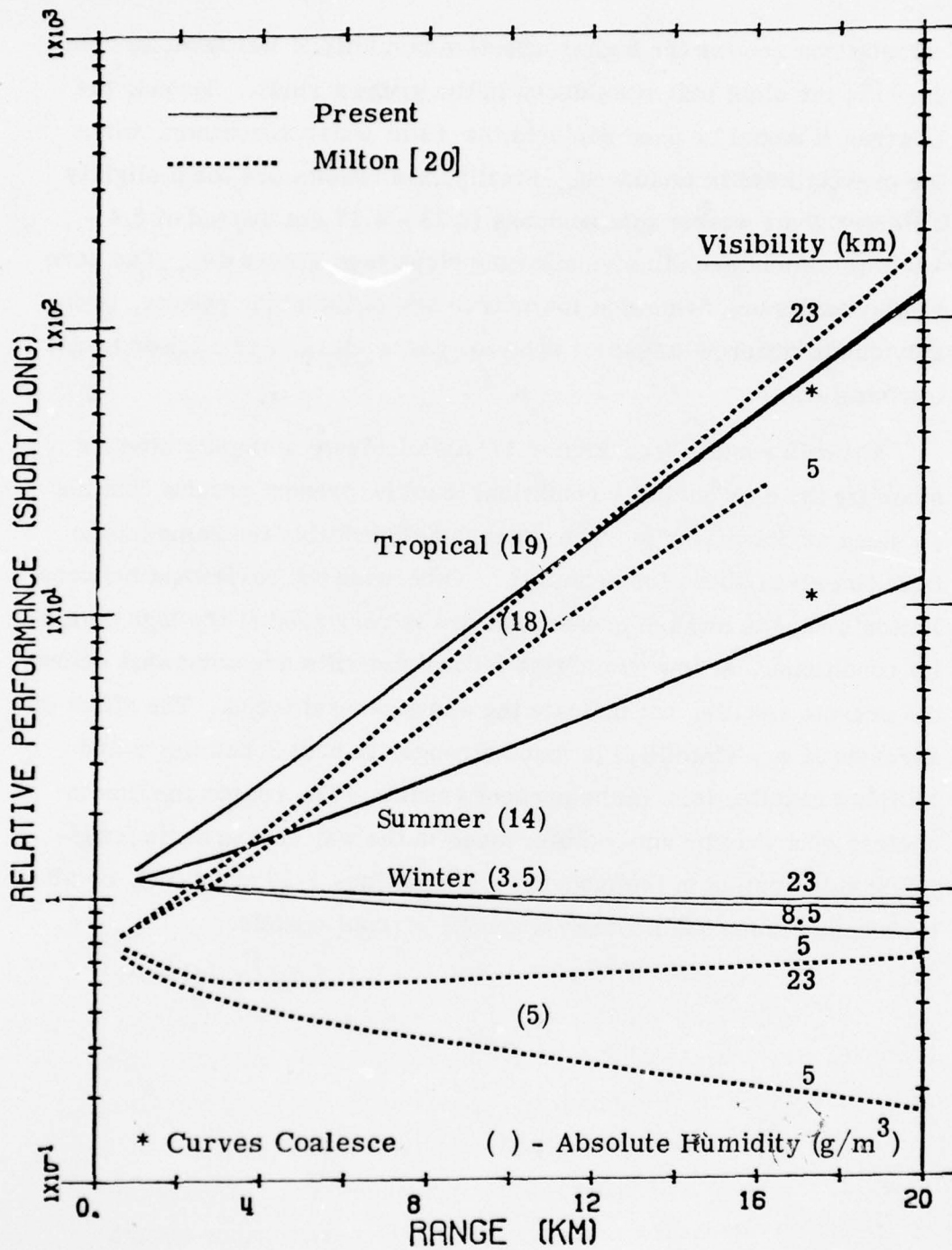


Figure 47. Comparison of Calculated Relative Performance with that of Milton

SECTION VI

CONCLUSIONS AND RECOMMENDATIONS

As shown in the previous section, the short wavelength infrared thermal imaging systems appear to offer some advantages over long wavelength systems for some situations. In particular, high humidity, long path length, low altitude operations favor the short wavelength system for the nominal target considered here (tank, rear aspect). Target temperature can have a significant effect on relative performance, while terrain temperatures are indicated to have minimal effect. Although aerosols are not predicted to have much influence on relative performance, this is thought to be a fictitious result of the simplified aerosol model used in Lowtran. A brief investigation of spectral bandpass optimization showed there could be some improvement in both bands, but nothing very significant for ranges less than twenty kilometers.

Comparisons with previous analyses indicate general agreement, considering the differences in conditions assumed. The main discrepancy, the slightly larger rate of increase in relative performance with range, is attributed to the higher humidity sea level conditions. Once again it should be emphasized that analyses of this type do not address the absolute performance of these systems, only relative performance. Thus, the results presented here should not be taken to indicate that either system would necessarily be capable of operating for all the conditions considered. On the other hand, even though the short wavelength system may be slightly inferior to the long wavelength system at some conditions, it may still have adequate performance there. This is quite likely the case for the Winter condition, since the performance of both systems should be excellent in this low humidity environment.

AD-A037 248

SCIENCE APPLICATIONS INC ANN ARBOR MICH
THERMAL IMAGING SYSTEMS' RELATIVE PERFORMANCE: 3-5 MICROMETERS --ETC(U)
JAN 77 T W TUE

F/G 17/5

DAEA18-73-A-0127

UNCLASSIFIED

SAI-76-005-AA

AFAL-TR-76-217

NL

2 OF 2
AD
A037248



END

DATE
FILMED
4-77

Based on the above conclusions, it is recommended that future studies of this type employ a more sophisticated and better verified atmospheric transmission and path radiance model, especially with regard to aerosol and water continuum modeling. In addition, it may be worthwhile to investigate, in more depth, the selection of optimum spectral operating regions, possibly considering several rather narrow bandpass filters. A statistical analysis of the effects of meteorological conditions for various likely operational theaters would also seem to be of value for the optimum design and implementation of thermal imaging systems.

ACKNOWLEDGEMENTS

The author would like to recognize the helpful and understanding program monitoring by Mr. James Stewart, the cooperative program management by Mr. Donald Fresh and the skillful manuscript preparation by Miss C. Hall. The author also appreciates the helpful discussion with Dr. H. Barhydt regarding some details of his sensor model. In particular, the author would like to acknowledge several valuable discussions of the study with Mr. Frederick G. Smith.

APPENDIX A AVAILABILITY OF INTERMEDIATE RESULTS

The analysis presented in this report can be considered in two parts: 1) the evaluation of the inputs to the performance model: atmospheric transmission and path radiance, and target and terrain radiance; and 2) the evaluation of the performance using the above inputs in Barhydt's model. In the future it may be desirable to utilize a more sophisticated or specific (i. e. , for a particular system) performance model with the results of Part 1, or simply use segments of it for some other purpose. For these reasons the results of Part 1 have been saved on magnetic tape for possible future use.

Atmospheric spectral transmission calculated by Lowtran III has been stored (in the order shown in Table A1) in files TRANS1 and

Table A1.
 Calculated Atmospheric Spectral Transmission
 and Path Radiance Cases

Visibility (km)	Platform Altitude (km)	Slant Range (km)
5.0	0.75	1, 5, 10, 20
8.5	0.75	1, 5, 10, 20
23.0	0.75	1, 5, 10, 20
8.5	0.50	1, 5, 10, 20
8.5	1.00	1, 5, 10, 20

TRANS2 (Transmission) for the Midlatitude Summer model for the short and long wavelength atmospheric windows, respectively. Similarly, files TRANS3 and TRANS4 contain the calculations for the Midlatitude Winter model, and TRANS5 and TRANS6 for Tropical. The short wavelength transmissions are digitized every 0.01 μm from 3.4 to 4.8 μm , while the long wavelength ones are every 0.02 μm from 8.1 to 12.2 μm . In order to adjust the long wavelength continuum, two records are provided for each case in TRANS2, TRANS4 and TRANS6: the first is the total transmission divided by the transmission due to continuum alone, and the second is the total transmission.

Atmospheric spectral path radiance calculated by Radst (and modified by Path) has been stored in the same order in files PRAD1-PRAD6 (Path Radiance). The only difference is that there is only one record for each case for both the short and long wavelength windows. Each record for both transmission and path radiance is preceded by an identification line which completely specifies the case. The number of entries in the record is also indicated on this line.

Terrain spectral radiance calculated by Photon for the cases outlined in Table A2 has been stored in file TRAD (Terrain Radiance).

Table A2.
Calculated Terrain and Target Radiance Cases

<u>Source</u>	<u>Condition</u>	<u>Temperature (K)</u>
Terrain	Night and Day	—
Terrain	Theoretical	250, 270, 290, 310
Target	Side and Front Rear Aspects	—
Target	Theoretical	250, 275, 325, 350

The first record contains the wavelengths (in μm) for which these data (and the other data) have been digitized. The long wavelength region is merged into the end of the short wavelength region in the same record. The second and third records contain the day and night terrain radiances ($\text{phot/sec/sr/m}^2/\mu\text{m}$) as measured by Smith and Blay [59]. The fourth through seventh records have the calculated blackbody radiances for temperatures of 250, 270, 290 and 310K, respectively.

The target spectral radiation function $\left(\frac{\partial^2 J^*}{\partial T \partial \lambda}, \text{phot/sec/sr}/\mu\text{m/K}\right)$ as calculated by Photon for the cases outlined in Table A2 has been digitized in the file TARSIG (Target Signature). The first three records contain the radiation function for the typical tank at front, side and rear aspects, respectively, based on the measurements of Moulton [61]. The last four records have the radiation function for a blackbody of projected area 15.7 m^2 at temperatures of 250, 275, 325 and 350 K, respectively.

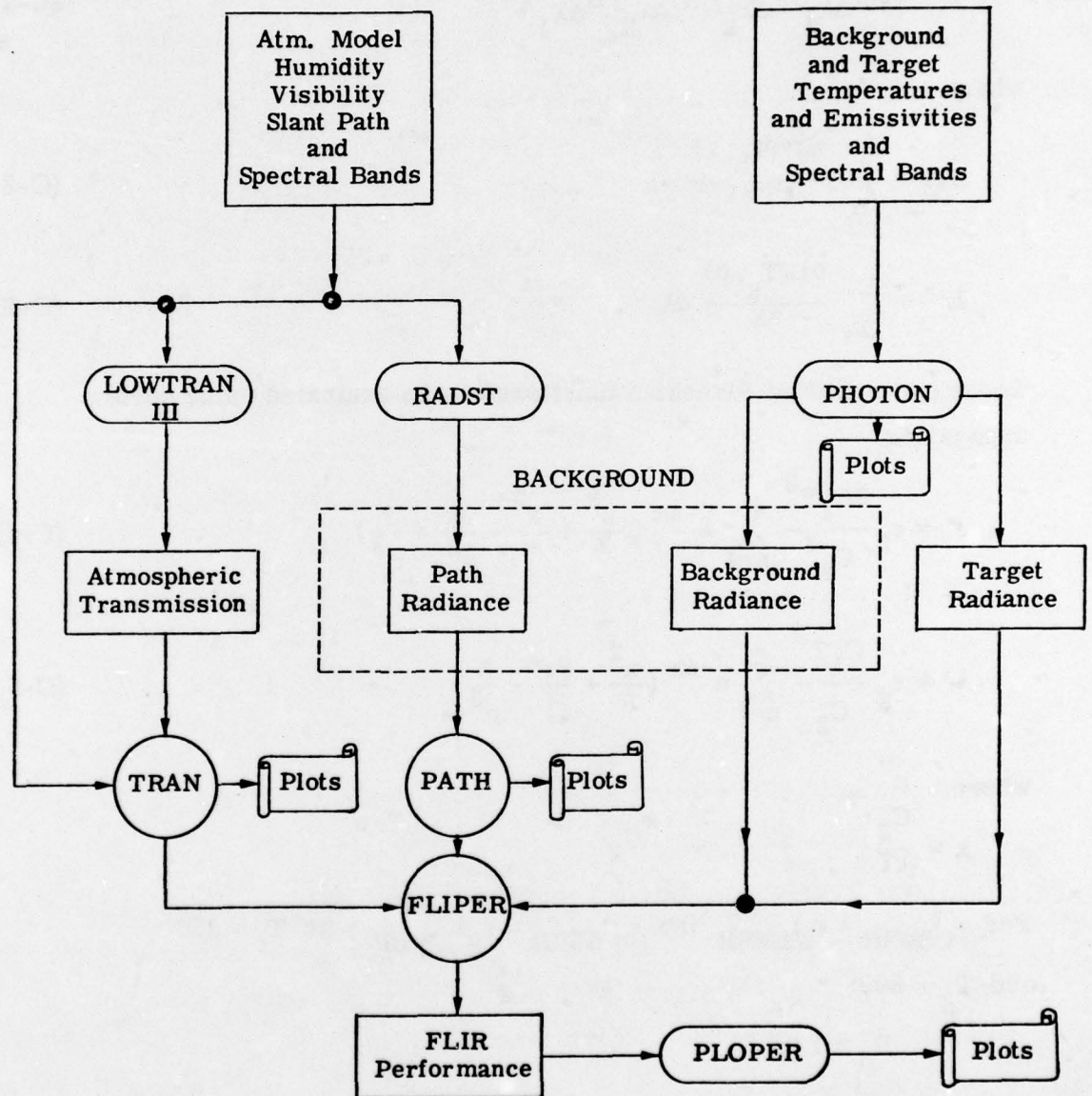
APPENDIX B

CALCULATIONAL PROCEDURE

The general calculational procedure is outlined in the flow diagram shown in Figure B1. A brief description of each of the computer codes (depicted by circles and ovals in Figure B1), is given below:

1. **LOWTRAN III** - The third generation AFCRL code to calculate atmospheric spectral transmission. Inputs are the atmospheric parameters (e. g. , seasonal and latitudinal model, and visibility), viewer slant path (altitude, range), and spectral bands.
2. **RADST** - A code developed by Anding to calculate the atmospheric spectral path radiance. Inputs are the same as those of Lowtran III (see #1, above).
3. **PHOTON** - Calculates the radiant intensity function of general targets, and the radiances of backgrounds from their temperatures and emissivities using the Planck function. Also produces plots as a function of wavelength.
4. **TRAN** - Re-formats the Lowtran output to even wavelength intervals and adds the 3-5 μm water continuum (or alternate 8-12 μm water continua). Also produces plots of atmospheric spectral transmission.
5. **PATH** - Converts RADST output to quantum units, and re-formats it to even wavelength intervals. Also produces plots of atmospheric spectral path radiance.
6. **FLIPER** - Calculates relative FLIR performance for various spectral bands (within limits of bands above). Has the option of suppressing path radiance and/or transmission in the background radiance term, or all atmospheric effects (i. e. , zero range condition).
7. **PLOPER** - Plots performance as a function of range for various conditions.

Figure B1.
Flow Diagram of Calculational Procedure



Ovals and Circles Indicate Computer Codes

APPENDIX C RELATIVE PERFORMANCE AT ZERO RANGE

At zero range, the relative performance of short-to-long wavelength thermal imaging systems is independent of the atmosphere ($\tau_a = 1$ and $L_p^* = 0$), so a closed form expression can be written:

$$P_o = \xi(J'_{\Delta\lambda_1}/J'_{\Delta\lambda_2}) (L_{\Delta\lambda_2}/L_{\Delta\lambda_1})^{1/2} \quad (C-1)$$

where

$$J'_{\Delta\lambda} \equiv \int_{\Delta\lambda} \frac{\partial J^*(T_b, \lambda)}{\partial T \partial \lambda} d\lambda \quad (C-2)$$

$$L' \equiv \int_{\Delta\lambda} \frac{\partial L(T_g, \delta)}{\partial \lambda} d\lambda \quad (C-3)$$

These two modified Planckian functions can be evaluated using series expansions

$$J' \cong \epsilon_t \frac{3C_1' T^2}{C_2^3} \sum_{n=1}^{\infty} e^{-nx} \left(\frac{x^3}{3} + \frac{x^2}{n} + \frac{2x}{n^2} + \frac{2}{n^3} \right) \quad (C-4)$$

$$L' \cong \epsilon_g \frac{C_1' T^3}{C_2^3} \sum_{n=1}^{\infty} e^{-nx} \left(\frac{x^2}{n} + \frac{2x}{n^2} + \frac{2}{n^3} \right) \quad (C-5)$$

where

$$x \equiv \frac{C_2}{\lambda T}$$

For $\epsilon_t^{SWIR} = \epsilon_t^{LWIR}$ and $\epsilon_g^{SWIR} = \epsilon_g^{LWIR}$, with $T_t = 350$ and $T_g = 300$:

$$P_o \cong 1.9.$$

At $T_t = 300$:

$$P_o = 0.79.$$

These are consistent with the curves shown in Figure 41.

REFERENCES

1. L. M. Biberman, "Background Considerations in Infrared System Design", App. Opt., Vol. 4, No. 3, pp. 343-345, Mar. 1965.
2. L. G. Mundie, A Comparison of InSb and Ge: Hg Detectors for Air -to-Ground Reconnaissance, Rand Memorandum RM - 5524-PR, Dec. 1967.
3. H. W. Yates and J. H. Taylor, Infrared Transmission of the Atmosphere, NRL Rept. 5453, June 8, 1960. (AD 240 188)
4. P. J. Wyatt, V. R. Stull and G. N. Plass, "The Infrared Transmittance of Water Vapor", Appl. Opt., Vol. 3, No. 2, pp. 229-241, Feb. 1964.
5. V. R. Stull, P. J. Wyatt and G. N. Plass, "The Infrared Transmittance of Carbon Dioxide", Appl. Opt., Vol. 3, No. 2, pp. 243-254, Feb. 1964.
6. F. A. Rosell, "Limiting Resolution of Low-Light-Level Imaging Sensors," JOSA, Vol. 59, p. 539, May 1969.
7. F. A. Rosell and R. H. Willson, Performance Synthesis (Electro-Optical Sensors), AFAL-TR-71-137, May 1971.
8. F. A. Rosell and R. H. Willson, Performance Synthesis (Electro-Optical Sensors), AFAL Tech. Rept. No. AFAL-TR-72-279, Aug. 1972.
9. F. A. Rosell and R. H. Willson, Performance Synthesis of Electro-Optical Sensors, AFAL-TR-73-260, Aug. 1973.
10. F. A. Rosell and R. H. Willson, Performance Synthesis of Electro-Optical Sensors, AFAL-TR-74-104, Apr. 1974.
11. R. L. Sendall and L. R. Skube, "An Advanced Foreward-Looking Infrared System," Proc. IRIS, Vol. 13, No. 1, p. 215, Apr. 1969.
12. R. L. Sendall and J. M. Lloyd, "Improved Specifications for Infrared Imaging Systems," Proc. IRIS, May 20-22, 1969.

13. R. L. Sendall and F. A. Rosell, E/O Sensor Performance Analysis and Synthesis (TV/IR Comparison Study), AFAL-TR-72-374, Apr. 1973.
14. N. Worthy, R. Sendall, et. al., High Performance IR Systems Study, AFAL-TR-71-286, Jan. 1972.
15. A. D. Schnitzler, "Image Detector Model and Parameters of the Human Visual System," JOSA, Vol. 63, pp. 1357-1368, 1973.
16. A. D. Schnitzler, "The Composite Flir - Visual System I: Quantitative Relationships between Performance and Design Parameters," IRIS Specialty Group on Infrared Imagery, p. 85, Aug. 1974
17. J.E.A. Selby and R. M. McClatchey, Atmospheric Transmittance from 0.25 to 28.5 μ m: Computer Code Lowtran 2, AFCRL-72-0745, 29 Dec. 1972, (AD-763-721).
18. H. Barhydt, D. P. Brown and W. B. Dorr, "Comparison of Spectral Regions for Thermal Imaging Sensors," Proc. IRIS, Vol. 14, No. 2, Aug. 1970.
19. H. Barhydt, "Review of Spectral Region Choice", Proc. IRIS, Vol. 18, No. 1, pp. 313-314, June 1973.
20. A. F. Milton, G. L. Harvey, J. C. Kershenstein and M. D. Mikolosko, A Comparison of the 3-5 Micrometer and 8-2 Micrometer Regions for Advanced Thermal Imaging Systems Using the Lowtran II Atmospheric Transmission Model, NRL Memo Rept. 3098, EOTPO Rept. #22, Aug. 1975.
21. P. M. Moser, "FLIR Operational Performance Model", IRIS Spec. Group on IR Imaging, ERIM Rept. 107600-5-X, p. 125, Aug. 1974.
22. Signal-to-Noise Ratio, Noise Equivalent Temperature Difference, Index of Performance and Design-Performance Tradeoffs for FLIR Imaging Devices, NAVAIRDEVCECN Tech Memo NADC-AEY-3: PMM/NEM, 16 June 1972.
23. Mathematical Model of FLIR Performance, NAVAIRDEVCECN Tech Memo NADC-20203: PMM, 19 Oct. 1972.

24. Predictions of FLIR Performance Against Ships, NAVAIRDEVCE
Tech Memo NADC-20203: PMM, 12 Dec. 1972.
25. D. L. Shumaker and R. B. Keller, A Mathematical Model of FLIR
System Performance in Target Detection and Identification, NRL
Memo Rept. 3098, EOTPO Rept. #22, pp. 127-161, Aug. 1975.
26. T. L. Altshuler, Infrared Transmission and Background Radiation
by Clear Atmospheres, GE Rept. 615D199, 1961 (AD-401923)
27. J.E. A. Selby and R.M. McClatchey, Atmospheric Transmittance from
0.25 to 28.5 μ m: Computer Code Lowtran 3, AFCRL-TR-75-0255,
7 May 1975.
28. R.A. McClatchey, et.al., AFCRL Atmospheric Absorption Line
Parameters Compilation, AFCRL-TR-73-0096, 26 Jan. 1973 and
later updates.
29. D.E. Burch, D. A. Gryvnak and J.D. Pembroke, Investigation of
the Absorption of Infrared Radiation by Atmospheric Gases: Water,
Nitrogen, Nitrous Oxide, AFCRL-71-0124, Jan. 1971, (AD 882876)
30. S.R. Reddy and C.W. Cho, Canadian J. Phys. Vol. 43, p. 2331,
1965.
31. M. M. Shapiro and H. P. Gush, Canadian J. Phys. Vol. 44, p. 949,
1966.
32. D. J. Spencer, G. C. Denault and H. H. Takimoto, "Atmospheric
Gas Absorption at DF Laser Wavelengths", Appl. Opt., Vol. 13,
No. 12, pp. 2855-2868, Dec. 1974.
33. R.K. Long, F.S. Mills and G.L. Trusty, Calculated Absorption
Coefficients for DF Laser Frequencies, RADC-TR-73-389, Nov. 1973.
34. R. E. Meredith, T.W. Tuer and D.R. Woods, Investigation of DF
Laser Propagation, ECOM - 74-4, July 1974. (AD005631)
35. K.O. White, W.R. Watkins and C.W. Bruce, Water Vapor Absorption
Measurements Using a Line Tuneable Deuterium Fluoride Laser, to be
presented at the Army Science Conf., June 1976.

36. F.S. Mills, Absorption of Deuterium Fluoride Laser Radiation, Ohio State U., Rept. ESL-4054-3, Sept. 1975.
37. F.G. Smith and T.W. Tuer, Propagation Characteristics of Potential Army High Energy Laser Systems, SAI Report in preparation, July 1976.
38. D.E. Burch, Investigation of the Absorption of Infrared Radiation by Atmospheric Gases, Aeronutronic U-4784, 31 Jan. 1971.
39. D.E. Burch, D.A. Gryvnak and F.J. Gates, Continuum Absorption by H₂O between 330 and 825 cm⁻¹, AFCRL-TR-74, 1974.
40. J.H. McCoy, D.B. Rensch and R.K. Long, "Water Vapor Continuum Absorption of Carbon Dioxide Laser Radiation near 10 μ ", Appl. Opt., Vol. 8, No. 7, pp. 1471-1478, 1969.
41. K.J. Bignell, Quart. J. Roy. Met. Soc., Vol. 96, p. 409, 1970.
42. R.E. Roberts, J.E.A. Selby and L.M. Biberman, "Infrared Continuum Absorption by Atmospheric Water Vapor in the 8-12 μ m Window," Appl. Opt., Vol. 15, No. 9, pp. 2085-2090, Sept. 1976.
43. V.G. Kunde and W.G. Maguire, Direct Integration Atmospheric Slant Path Transmittance Model for Interpretation of High Spectral Resolution Planetary Thermal Emission Spectra, NASA Goddard Report, Jan. 1973.
44. F.E. Volz, "Infrared Refractive Index of Atmospheric Aerosol Substances", Appl. Opt., Vol. 11, No. 4, pp. 755-759, Apr. 1972.
45. G.L. Trusty, Private Communication to SAI, 10 Mar. 1975.
46. D.J. Gambling, An Aerosol Attenuation Model for the Visible and Infrared Spectral Regions, Weapons Research Est., Australia WRE-TN-593 (AP), Mar. 1972.
47. J.A. Hodges, "Aerosol Extinction Contribution to Atmospheric Attenuation in Infrared Wavelengths:", Appl. Opt., Vol. 11, No. 10, pp. 2304-2310, Oct. 1972.
48. E.A. Barnhardt and J.L. Streete, "A Method for Predicting Atmospheric Aerosol Scattering Coefficients in the Infrared", Appl. Opt., Vol. 9, No. 6, pp. 1337-1344, June 1970.

49. B. S. Katz, E/O Met Analysis Using North Atlantic Ship Reports and HEL Generated Optics Codes, NSWC Memorandum WR-42: BSK:cbb, Jan. 1976.
50. E. P. Shettle and R. W. Fenn, Models of Atmospheric Aerosols and Their Optical Properties, Presented at AGARD EM Wave Propag. Panel - Optical Propag. in the Atm., Oct. 1975.
51. E. P. Shettle, Maritime Aerosol Models, AFCRL-OPA/E/E. Shettle/861-4344, 10 Feb. 1975.
52. R. A. McClatchey and J. E. A. Selby, Atmospheric Attenuation of Laser Radiation from 0.76 to 31.25 μm , AFCRL-TR-74-0003, 3 Jan. 1974.
53. R. A. McClatchey and J. E. A. Selby, Atmospheric Attenuation of HF and DF Laser Radiation, AFCRL-TR-72-0132, 23 May 1972.
54. R. A. McClatchey and J. E. A. Selby, Atmospheric Transmission 7-30 μm : Attenuation of CO₂ Laser Radiation, AFCRL-72-0611, 12 Oct. 1972.
55. G. J. St. Cyr, Extinction Coefficients and Energy Scattered by Clouds, Fog, Maritime Haze and Continental Haze, Hughes Aircraft Co. 2771.1/48, July 1968.
56. J. A. Dowling, Preliminary Aerosol Measurements (unpublished data), private communication to SAI, Jan. 1976.
57. D. H. Arnold, D. B. Lake and R. Sanders, Comparative Measurements of Infra-Red Transmission Over a Long Oversea Path, EMI Electronics, Ltd., Rept. No. DMP 3736, Contract No. KJ/D/4404/CB19A, Oct. 1970.
58. D. H. Arnold and R. Sanders, Comparative Measurements of Infra-Red Transmission Over a Long Path, August/September 1970, EMI Electronics, Ltd., Rept. No. DMP 3858, Contract No. KJ/D/4404/CB19A, May 1971.
59. C. D. Smith and D. W. Blay, "Infrared Signatures of Ground Vehicular Targets," Proc. IRIS, Vol. 19, pp. 35-64, Sept. 1974.

60. J. N. Hamilton, J. A. Rowe and D. Anding, Atmospheric Transmission and Emission Program, Aerospace Report TOR-0073 (3050-02)-3, June 15, 1973.
61. J. R. Moulton, S. P. Rodak and F. H. Zegal, "Target Signatures for Thermal Imager Performance Models," IRIS Specialty Group on Infrared Imaging, pp. 27-65, Aug. 1974.